Lateral Programmable Metallization Cell

Devices And Applications

by

Minghan Ren

A Dissertation Presented in Partial Fulfillment
of the Requirements for the Degree
Doctor of Philosophy

Approved January 2011 by the
Graduate Supervisory Committee:

Michael Kozicki, Chair
Dieter Schroder
Ronald Roedel
Hugh Barnaby

ARIZONA STATE UNIVERSITY

May 2011

ABSTRACT

Programmable Metallization Cell (PMC) is a technology platform which utilizes mass transport in solid or liquid electrolyte coupled with electrochemical (redox) reactions to form or remove nanoscale metallic electrodeposits on or in the electrolyte. The ability to redistribute metal mass and form metallic nanostructure in or on a structure in situ, via the application of a bias on laterally placed electrodes, creates a large number of promising applications.

A novel PMC-based lateral microwave switch was fabricated and characterized for use in microwave systems. It has demonstrated low insertion loss, high isolation, low voltage operation, low power and low energy consumption, and excellent linearity. Due to its non-volatile nature the switch operates with fewer biases and its simple planar geometry makes possible innovative device structures which can be potentially integrated into microwave power distribution circuits.

PMC technology is also used to develop lateral dendritic metal electrodes. A lateral metallic dendritic network can be grown in a solid electrolyte (GeSe) or electrodeposited on SiO_2 or Si using a water-mediated method. These dendritic electrodes grown in a solid electrolyte (GeSe) can be used to lower resistances for applications like self-healing interconnects despite its relatively low light transparency; while the dendritic electrodes grown using water-mediated method can be potentially integrated into solar cell applications, like replacing conventional Ag screen-printed top electrodes as they not only reduce resistances

but also are highly transparent. This research effort also laid a solid foundation for developing dendritic plasmonic structures.

A PMC-based lateral dendritic plasmonic structure is a device that has metallic dendritic networks grown electrochemically on SiO_2 with a thin layer of surface metal nanoparticles in liquid electrolyte. These structures increase the distribution of particle sizes by connecting pre-deposited Ag nanoparticles into fractal structures and result in three significant effects, resonance red-shift, resonance broadening and resonance enhancement, on surface plasmon resonance for light trapping simultaneously, which can potentially enhance thin film solar cells' performance at longer wavelengths.

This dissertation is dedicated to my wife,

son and parents

ACKNOWLEDGMENTS

I am deeply obliged to my advisor Prof. Michael Kozicki for offering me this terrific research opportunity and being supportive throughout good times and bad times. Without his mentorship and tremendous motivation, I would not be here. I also would like to thank my committee members, Dr. Dieter Schroder, Dr. Ronald Roedel and Dr. Hugh Barnaby for their suggestions and support. I am also thankful to Professor Nathan Newman for providing me the important equipment for spectroscopy measurement.

I wish to express my forever thanks to my parents, Bowen Ren and Lianfang Xin, who have dedicated their whole life for my better future. Without their support, love and sacrifice. I would not be myself. I would like to especially thank my father for inspiring my dreams and ambition. I am also indebted to my grandparents, Deyou Ren, Jinmei Liu, Afeng Xu and Suzhen Li for selflessly taking great care of me, which I cannot repay. I pray for them and may they rest in peace. I am also grateful to my aunt Jianqiu Ren for giving me the support and encouragement when I most needed and may she rest in peace.

My special thanks go to my beautiful wife Yun Xia who delivered me the most wonderful gift in the world, our son Daoye Ren. She has always been patient, considerate and supportive even when I had to work away from home for such a long time and gave me the faith, strength and encouragement to achieve my dreams and goals.

I would also like to thank all the staff in the Center for Solid State Electronics Research and my research colleagues, Sarath Chandran, Sunil Baliga

and Deepak Kamalanathan for always helping me with my experiments and research.

TABLE OF CONTENTS

CHAPTER Page

LIST OF TABLES

Table Page

LIST OF FIGURES

Figure Page

Figure Page

Figure Page

Figure Page

Figure Page

Figure Page

1. INTRODUCTION

Electrochemical deposition has advanced from an art to a science over the past few decades and been developed into one of the important processes in electronic industries. The original purpose of using electrochemical deposition is to increase the value of metal articles by coating the articles and enhancing their appearance (Siah). These days, the trend has turned toward surface treatments that allow the use of cheaper substrate metals or plastics, which will deliver corrosion resistance or other special physical or mechanical properties to the surface (e.g. conductivity, heat or wear resistance, lubrication or solderability) (Siah).

Electrochemical technology entered the electronics industry about 50 years ago as a manufacturing process for printed circuit boards (PCB). In 1998 the major integrated circuits (ICs) manufacturers started a huge revolution of switching aluminum conductors fabricated by physical methods (e.g. evaporation or sputtering), to copper (Cu) conductors produced by electrochemical methods (electrodeposition) (Paunovic). This change from physical to electrochemical techniques in the microelectronics industry has spurred an enormous amount of interest in electrochemical deposition. Today, this technology is extensively in use for processing advanced microelectronic components, including Cu chip, high end packages and interconnects, thin film magnetic heads, microelectromechanical systems (MEMS), etc (Siah).

The fundamentals of electrochemical deposition lie in Electrochemistry which deals with the relationship between electricity and chemical change, as its name suggests. Metal atoms which are deprived of electrons in the process of

oxidation become ion at one location and they are able to move under the direction of an electric field in liquid or solid electrolytes. By the time when they receive electrons at another location, these displaced ions are reduced back to atoms (Mitkova and Kozicki). Note that ions not only carry charge but also have substantial mass. In this situation, it is only the mass that is redistributed in the process – the atoms are detached from one location and deposited at another location under the influence of an external energy source (Mitkova and Kozicki). Two conditions have to be satisfied before the mass transport can occur: 1. the oxidizable electrode (the anode) in an electrolyte must be made positive against the other electrode (the cathode); 2. a sufficient bias is applied, typically greater than a few hundred millivolts, to overcome the chemical potential barrier at the electrode (Mitkova and Kozicki). The number of atoms removed and deposited will be equal to the number of electrons that come from the external source and participate in the process. The electrodeposited mass is therefore controlled by the total Faradaic charge (which takes part in the electrochemical reaction) from the power supply (Mitkova and Kozicki). Each reduced metal ion is offset by an oxidized metal atom and therefore the whole electrodeposition process is self-balanced to prevent from forming the internal build-up electric field which would eventually annul the applied field and terminate the process (Mitkova and Kozicki). To make the electrodeposition process reversible, the opposite electrode must be electrochemically inert (not oxidizable) and the polarity of the applied bias must be reversed and the rest rules in respect to deposition remain the same for dissolution (Mitkova and Kozicki). This dissimilar electrode structure makes

possible the cycling of deposition/dissolution process (Mitkova and Kozicki). Note that during the dissolution process, once the excess metal which came from the previous electrodeposition is completely exhausted, the dissolution process self-terminates (Mitkova and Kozicki).

Programmable Metallization Cell (PMC) is a technology platform which utilizes mass transport in solid or liquid electrolyte films coupled with electrochemical reactions to form nanoscale metallic electrodeposits on or in the electrolyte. The potential to utilize PMC technology to redistribute metal mass attracts lots of interest and leads to numerous applications. For example, deposition and dissolution of metal mass, like Ag or Cu, in a solid electrolyte can dramatically change electrical resistance up to some eight orders of magnitude and this effect is used in solid state memory to store information (Kozicki, Park and Mitkova); deposition of mass can be used to adjust the resonant frequency of a MEMS resonator (S. Enderling et al.) or a MEMS microphone (Sang-Soo et al.); it can also be used to block or reflect light and makes possible optical switches (Mitkova, Kozicki and Aberouette); it can be used to alter surface property, making surface more hydrophobic, and leads to applications in microvalves and other fluid/droplet control devices (Kozicki, Maroufkhani and Mitkova).

PMC devices can be categorized into vertical and lateral devices based on how electrodes are positioned. For the vertical devices, the thin film of electrolyte is sandwiched between the electrodes so that the electrodeposition occurs within the glass. In this structure, fast electrical switching can be realized as the distance between the electrodes which is determined by the electrolyte film thickness can

easily reach the order of tens of nanometer or less. For example, PMC memories which are in need of speedy switching adopt this design, shown in Fig. 1. In the lateral devices, the electrodes are coplanar and the electrodeposit forms between them either on the surface of a thin film of solid electrolyte or in a layer of liquid electrolyte which covers the coplanar electrodes. The lateral arrangement can be perfectly fit for applications that require large electrodeposits to change the physical properties of a surface or applications that need minimum capacitive coupling. Note that the capacitance in the lateral device is directly proportional to area that in this case is the cross-section of the electrode which is typically much smaller than the area of the electrode. Fig. 2 shows an example of a lateral PMC device, a MEMS resonator with PMC tuning scheme.

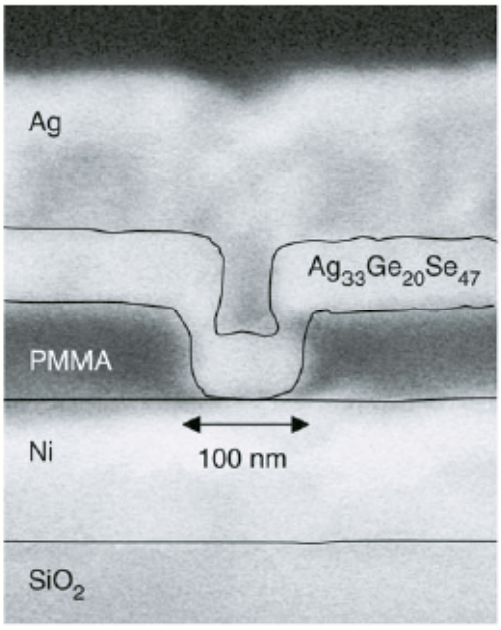

Fig. 1 Scanning electron microscope image of a PMC memory cell cross section fabricated using PMMA as the dielectric. The Ag–Ge–Se electrolyte and silver anode are formed in a 100 nm via in the dielectric (M. N. Kozicki et al.)

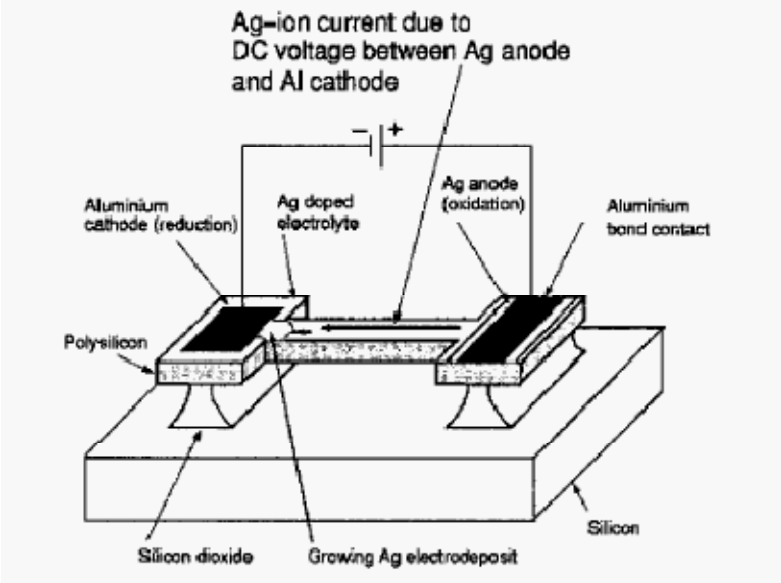

Fig. 2 Schematic of a polysilicon microbeam with integrated electrolyte, Ag anode and aluminium contacts (S. Enderling et al.)

1.1 Goals and outline of dissertation

This work is directed towards developing innovative PMC-based lateral devices, including PMC-based microwave switch, dendritic electrode and dendritic plasmonic structures, using mass transport in either solid electrolytes or liquid electrolytes for novel applications for microwave or photovoltaics. Designs, fabrications, experimentals and results of PMC-based lateral devices are discussed in this dissertation. The rest of the first chapter is intended to provide fundamentals and background about electrochemical deposition and PMC technology. Chapter 2 discusses the design, fabrication, characterization and results of PMC-based microwave switch. Chapter 3 presents the design, fabrication, tests and results of PMC-based dendritic electrode. Chapter 4 covers the design, fabrication, tests and results of PMC-based dendritic plasmonic structures. Conclusions are given in Chapter 5.

1.2 PMC technology

PMC technology is based on an electrochemical mass redistribution effect, in which mobile ions within a liquid or solid electrolyte undergo an electrochemical process to form and erase conductive metallic filaments with a small bias applied between two unlike electrodes. The ability to redistribute metal masses in devices or structures in situ makes the PMC technology available for a wide range of potential applications, including solid state electronics, MEMS, microfluidics, microwave electronics, optics, etc. The science behind the PMC technology will be briefly reviewed in this section.

Electrochemistry is a science concerned with the interrelation of electrical and chemical effects. All electrochemical reactions can be classified as redox reactions which can be deemed as two independent half reactions, oxidation and reduction. In the oxidation process, an atom, which loses electrons at the anode where the oxidation occurs, is transformed into an ion. Under the guidance of an electrical field, the ion can flow in an ion conductor, which is also called electrolyte and can be either liquid or solid form. The displaced ion finally reaches the cathode in which the reduction occurs, regains those lost electrons and is turned back to an atom again. An electrochemical cell is thus designed to combine the two half reactions in one place. A simple liquid-state electrochemical cell (LSE) with a battery power source is illustrated in Fig. 3. It contains an Ag anode denoted by M, a W cathode and a water electrolyte. Ag is an easily oxidizable metal while W is considered as an inert electrode material. When a positive voltage is applied to the anode, Ag is oxidized and become ions. These

ions are drawn across the electrolyte under the influence of the electrical field and deposited at the cathode resulting from the reduction (Balakrishnan):

$M \rightarrow M^+ + e^-$ ---------- Oxidation

$M^+ + e^- \rightarrow M$ ---------- Reduction

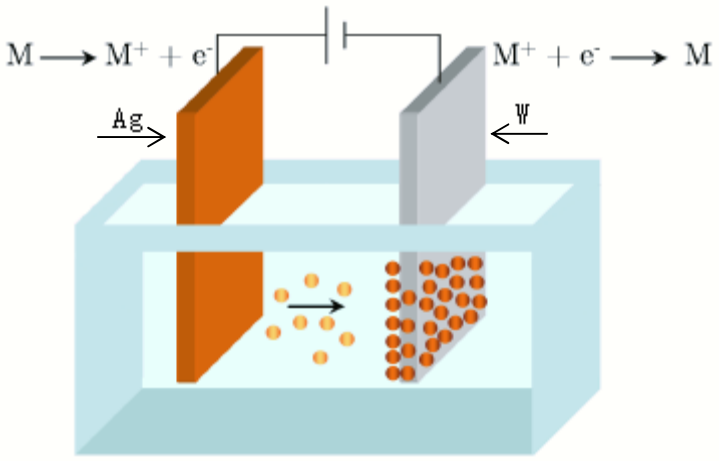

Fig. 3 Schematic illustrating a simple electrochemical cell set up with aquaous electrolyte (Schindler)

In a solid-state electrochemical cell (SSE), the liquid electrolyte is replaced with the solid electrolyte and solid electrolytes behave very similarly to liquid electrolytes based on the same thermodynamic principles (Riess). Yet, there are some differences between them. Firstly, there is no (electron/hole) conduction in most liquid electrolytes, while electronic conduction exists to some extent in all solid electrolytes (Riess). Secondly, in LSEs, it is possible to stir and replenish the liquid electrolyte but apparently this is not feasible in SSEs (Riess). Finally, in liquid electrolytes both cations and anions are mobile, while in solid electrolytes only one kind of ions is usually free to move while the other immobile ions form a

solid matrix providing a frame for the motion of the mobile ion which can “hop” into neighboring potential wells (Nessel et al.). According to the short-range hopping mechanism for conduction, the ionic conductivity of solid electrolytes can locally reach electronic conductivity levels which are accomplished in current semiconductors (Nessel et al.).

There are many inorganic and organic ion-conductive materials but it is the so-called chalcogens that draw a great amount of interest in the context of PMC devices, mainly due to their high ion availability and mobility at normal device operating temperatures (Michael N. Kozicki et al.). When the chalcogenide is doped with metal ions by either thermal annealing or photodissolution, a ternary can be created in the form of a discrete nanoscale metal ion-rich phase in a continuous glassy matrix due to the nucleation of metal ions on the chalcogen-rich regions (Nessel et al.). In such a situation, the electrolyte with large quantities of highly mobile metal ions yet has a fairly high resistivity (necessary for a high off resistance state) (see Fig. 4(a)) (Nessel et al.).

For example, in PMC non-volatile memory application, a base glass of Ge_3Se_7 is utilized and saturated with Ag+ ions. To enable an ion current to flow in an electrolyte, a sufficient positive bias, typically on the order of a few tenths of a volt or more to overcome the potential barrier (chemical in nature) at the cathode, is applied across an anode which is composed of an oxidizable electrode and a cathode. The magnitude and duration of the ion current, i.e., the total faradaic charge will determine the amount of metal deposited. In Ag+ saturated Ge_3Se_7, excessive Ag+ ions are formed by oxidizing Ag at the anode and these ions are

drawn toward the cathode, under the direction of the applied electrical field, via the coordinated hopping mechanism described above (Nessel et al.). At the cathode, Ag metal is re-formed by a reduction reaction with injected electrons, as shown in Fig. 4(b). The number of atoms electrodeposited by the reduction of ions will be equal to the number of electrons that participate in the process (supplied by the external circuit). Each reduced metal ion will be replenished by an oxidized metal atom to prevent from forming an internal electric field due to the buildup of charge. The process will last as long as the programmed voltage/current limits enforced by the external power source is not reached or the oxidizable metal supply is not totally consumed (Nessel et al.). If the current limit is made sufficiently high (~μA), an Ag conductive path is formed to connect the two electrodes (Fig. 4(c)) with no power required to sustain it (Nessel et al.). To be able to reverse this process, the original cathode must be made electrochemically inert (not oxidizable) and the polarity of the bias must be reversed (Nessel et al.). The Ag metal bridge is dissolved and deposited back onto the original anode in order to maintain the balance (Fig. 4(d)) (Nessel et al.). Once the electrodeposit is completely dissolved, the process terminates itself (Nessel et al.).

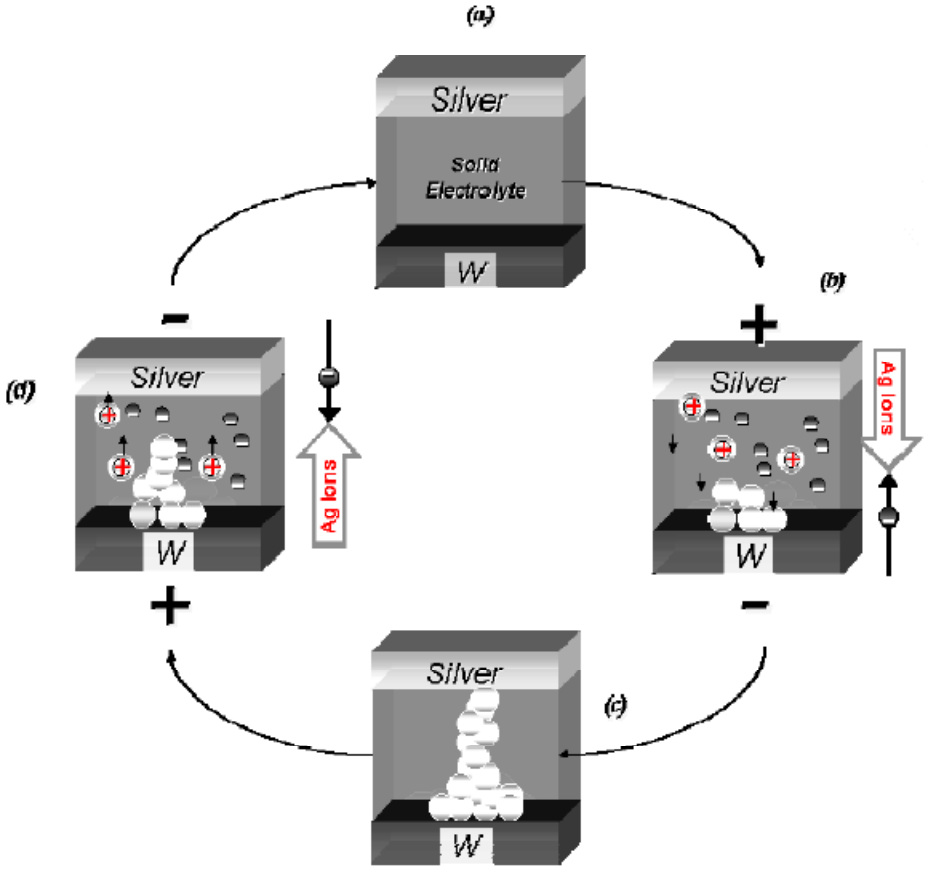

Fig. 4 Device operation. (a) switch is off, (b) small bias forces electrons in cathode to reduce silver ions in substrate, (c) process halts when path is formed, and (d) process is reversed with application of reverse bias (Nessel et al.), (Ratnakumar).

The electrodeposition is a Faradaic process; however, there is also a non-Faradaic process that occurs in the SSE, which somehow affects the ion velocity. In case of non-Faradaic processes, the behavior of the electrode/electrolyte interface is similar to that of a capacitor with a capacitance in the order of 10^{-14} F/μm2 and resistance around 10^{10} Ω.μm2 for a typical solid electrolyte under small applied bias (Waser). This is called the electrochemical double layer and the

capacitance associated with it is called the double layer capacitance. Most of the applied voltage will be dropped across the double layer, which is typically a few tens of nanometers thick and the field will therefore be in the order of 10^5 V/cm. For best solid electrolytes with a typical mobility in the order of 10^{-3} cm^2/V s, the effective ion velocity can be as high as 1 m/s (Mitkova and Kozicki). Such high ion velocity makes PMC technology a good candidate for fast switching applications like microwave switches or memories.

2. PMC-BASED MICROWAVE SWITCH

2.1 Introduction

The market volume of portable electronic devices equipping wireless interfaces has been increasing recently. Mobile phone production volume grew from 680 million units to 1,400 million units in the past five years (Andoh). The demand for multiband, multimode band switching at low insertion loss while maintaining excellent linearity in mobile phones is driving the need for RF switches. A novel PMC-based microwave switch was developed that shows a low insertion loss of ~0.5dB, excellent linearity up to 6 GHz, isolation of >30dB, low voltage operation (1V), low power (~μW) and low energy (~μJ) consumption. This research project was cooperated with NASA Glenn Research Center (GRC). I was involved in device fabricating and processing improvement. The simulations and measurements were performed at GRC.

In this chapter, the basics and key parameters of microwave switches are explained first, followed by the introduction and discussion of the novel PMC-based microwave switch.

2.2 The basics of microwave switch

Switches are a simple but vital component of all microwave circuit systems and a very basic definition for such a component is: a switch is a device for making or breaking an electric circuit and is capable of routing signals between a system and devices for enhancing their flexibility and expandability (Varadan et al.). Fig. 5 presents two simple switch configurations in an electric circuit.

At high frequencies, many issues relating to performance of any circuit also apply to switches. The most important are:

· Insertion Loss versus frequency (bandwidth)

· VSWR versus frequency (mismatch)

· On-off isolation (feed-through) and isolation to other circuitry (crosstalk)

· Power handling

· Switching speed

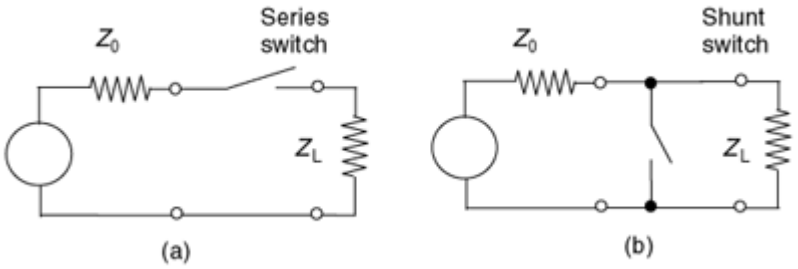

Fig. 5 Typical switch configurations: (a) series switch, (b) shunt switch. Note: Z, impedance (Varadan et al.)

2.2.1 Insertion loss

The insertion loss is the attenuation between input and output ports of the switch, when the switch is in the "ON" state. It is a measure of a microwave switch's efficiency for signal transmission. Insertion loss can be defined by the power drop or voltage attenuation caused by the switch on a signal:

$$\text{Insertion loss (dB)} = 10\log_{10}\left(\frac{\text{Pout}}{\text{Pin}}\right) = 20\log_{10}\left(\frac{\text{Vout}}{\text{Vin}}\right) \text{ (Jhangiani)}$$

or specified in terms of the transmission coefficient, S_{21}, in dBs, between the input and output ports of the switch circuit.

$$IL = -20\log_{10}|s_{21}| \text{ dB (Wikipedia "Insertion Loss")}$$

Insertion loss occurs due to parasitic capacitance, inductance, resistance, and conductance that reside in the circuitry of the switch. All these parasitic components contribute to weaken and degrade the signal that the switch routes (Jhangiani). Resistive losses at lower frequencies and skin-depth effects at higher frequencies are the dominant causes for losses.

2.2.2 Voltage standing-wave ratio (VSWR)

VSWR is the ratio of reflected-to-transmitted waves. At higher frequencies, signals are transmitted in the form of waves when passing through a transmission line or cable. Reflections occur when such signals pass through different media (such as components with unmatched impedances) (Jhangiani). In a switch module, this mismatch occurs due to slight variances in characteristic impedances of the connector, the PCB traces, and the actual relay itself (Jhangiani). The reflected wave combined with the input signal either increases or decreases its net amplitude, depending on the phase of the reflection with respect to the input signal (Jhangiani).

2.2.3 Isolation and crosstalk

Isolation is defined as the magnitude of coupling of a signal in the off state, which can be measured as S21 between the input and output of a switch in the off state. A large value of S21 (in decibels) indicates good isolation (Jhangiani). Crosstalk is defined as the magnitude of undesired coupling of a signal between circuits (such as separate multiplexer banks on an RF module) (Jhangiani).

2.2.4 Power handling

Microwave power handling assesses the efficiency of carrying the RF signal in a switch. One commonly assumes that the output power level follows the input power linearly before it hits a certain point and starts to lose its linearity. This point is generally defined in terms of a 1 dB compression point, which is borrowed from the amplifier industry (Varadan et al.). The 1 dB compression point is defined as the input power level at which the switch insertion loss increases by 1 dB over its low-level with respect to linearity (Varadan et al.).

2.2.5 Figure of merit

The switch's on-state impedance is determined by resistance and the off-state is determined by capacitance at microwave frequencies. With direct current the off-on impedance ratio can be used to characterize a switch. The impedance ratio for a simple microwave switch is

$$Zratio = Zon/Zoff = jwCR.$$

The ratio is frequency-dependent since the off state is determined by a capacitance. The product of CR is a characteristic number called the figure of merit (FOM) of a switch (Grant, Denhoff and Mansour).

$$FOM=CR$$

A smaller FOM means the on impedance is small with respect to the off impedance, which also means better performance typically (Grant, Denhoff and Mansour). The reciprocal of the FOM is called the cut-off frequency. A better switch element can be made by reducing R while C is held constant or by

reducing C while holding R constant. In an ideal situation both R and C can reduced (Grant, Denhoff and Mansour).

2.3 PMC-based microwave switch design

2.3.1 Introduction

Four existing main switch technologies have been reviewed and their own advantages and disadvantages are summarized as follows. The commonly used microwave switches are mechanical switches (coaxial and waveguide) and semiconductor switches (p-i-n diode and FET). Mechanical coaxial and waveguide switches have the advantage of low insertion loss, large off-state isolation, high power handling capabilities, and are highly linear. However, they are bulky, heavy and slow. Oppositely, semiconductor switches such as p-i-n diodes and FET offer much faster switching speed and are smaller in size and weight, but are substandard in insertion loss, DC power consumption, isolation and power handling than their mechanical counterparts (Grant, Denhoff and Mansour). MEMS switches are one of the potential candidates to replace conventional switches. They promise to offer the high RF performance and low DC power consumption of mechanical switches, and the small size, weight and low cost features of semiconductor switches, but are at the cost of reliability and speed due to their moving parts.

Compared to aforementioned microwave switches, the PMC-based lateral switch offers several unique features due to its electrochemical nature. Firstly, the process is non-volatile. Power is only required to change states but not to maintain a particular state (ON or OFF). Consequently, fewer bias operations are involved.

The process is also low energy, requiring on the order of μJ to operate. Power consumption is thus comparable to MEMS devices. There are no moving parts (as in MEMS devices), eliminating this point of failure and enhancing speed. Merely on the order of tenths of a volt is needed to activate a PMC device, superior to solid state and MEMS-based switches. The switching speed is potentially competitive with solid state switches because metal ion conductivity in these base solid electrolytes is comparable to electron conductivity in semiconductors. Finally, fabricating PMC-based switches requires only as little as five processing steps, using conventional semiconductor fabrication tools. This leads to an unmatched ease of integration and reduction in cost, compared to solid state and MEMS devices, which may need several sacrificial layers and masks for fabrication (Nessel et al.).

2.3.2 Reference design

The preliminary design of a microwave series switch is based on a simple two electrode coplanar geometry. A reference design layout can be seen in the microphotograph of Fig. 6. Two electrodes (~50 nm) of dissimilar metals (Ag anode, Ni cathode) are deposited onto a thin film (~60 nm) of silver-saturated $GeSe_2$ glass on a 500 μm thick quartz substrate (ε_r = 3.9). A gap of 2-100 μm separates the two electrodes. Several iterations provided the framework for an optimal geometry based on the nanoionic material characteristics and coplanar layout.

2.3.2.1 Device fabrication

The reference design of a microwave series switch is based on a simple two electrode coplanar geometry comprising an Au bottom ground electrode, a quartz substrate, the solid electrolyte, an inert electrode (Ni) and an oxidizable electrode (Ag). Fig. 7 shows a schematic drawing of the device. To fabricate the test structures, a 60 nm thick Ge_3Se_7 layer was deposited by thermal evaporation (Edwards 1) onto a 500 µm thick quartz substrate with a pre-deposited Au ground plate. A 20 nm thickness Ag layer was deposited in the same equipment and was dissolved into the base glass by photodissolution at room temperature using exposure to ultraviolet light from a 405 nm broadband source with an energy density at the wafer surface of 1 J/cm2. Following photodissolution, a 50 nm thick Ni cathode was deposited by electron beam evaporation (CHA1) and an additional 50 nm thick Ag anode was added by thermal evaporation (Edwards 1) to ensure a continuous oxidizable source for electrodeposition. The process flow for the fabrication is illustrated in Fig. 8.

2.3.2.2 Device measurements

To measure the RF performance of the devices, the test samples were individually diced and mounted onto a structure as shown in Fig. 9. The circuit was connected to an Agilent E8361A Vector Network Analyzer (VNA) to determine the isolation (S_{21} in the OFF state) and insertion loss (~S_{21} in the ON state). VNA calibrations were performed in two stages: one measurement was taken from 400 MHz to 4 GHz and another from 4 GHz to 22 GHz. An Agilent E3646A DC Power Supply was utilized to turn the device ON and OFF. Initial

measurements were performed using current limits of 100 mA and (typical) voltages of 1-3 V. Fig. 10 and Fig. 12 provide representative plots of device performance as they were cycled repeatedly between ON/OFF states for the lower and higher frequency ranges, respectively.

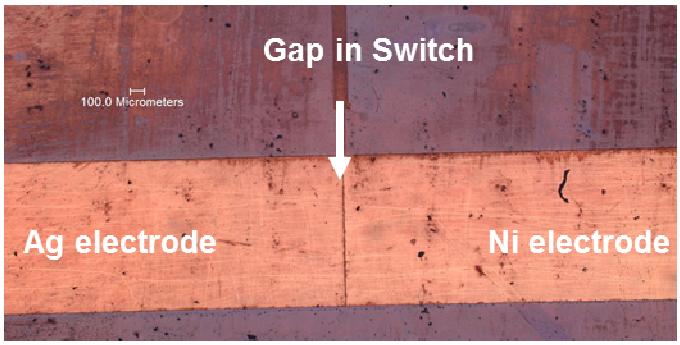

Fig. 6 Microphotograph of coplanar PMC-based switch reference design

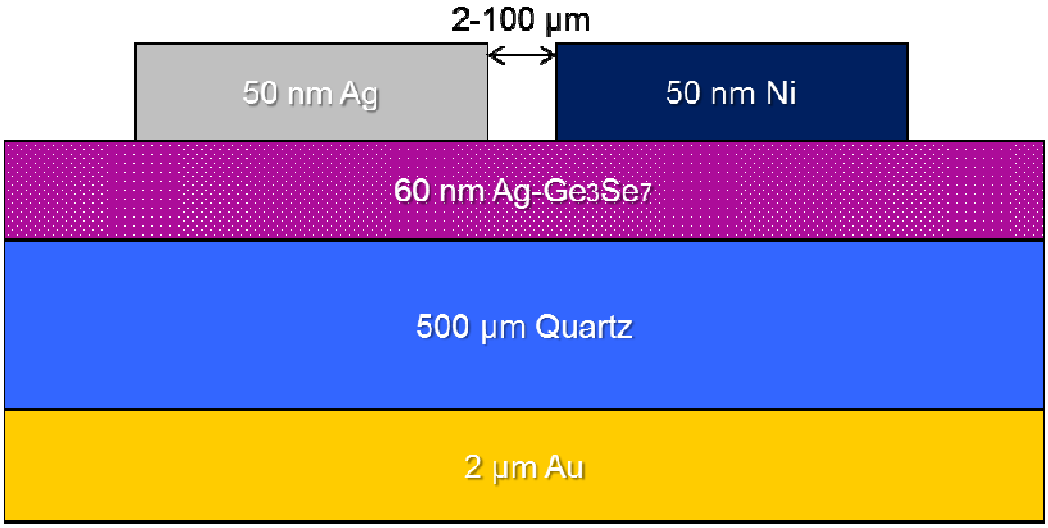

Fig. 7 Schematic of a PMC-based microwave switch with reference design

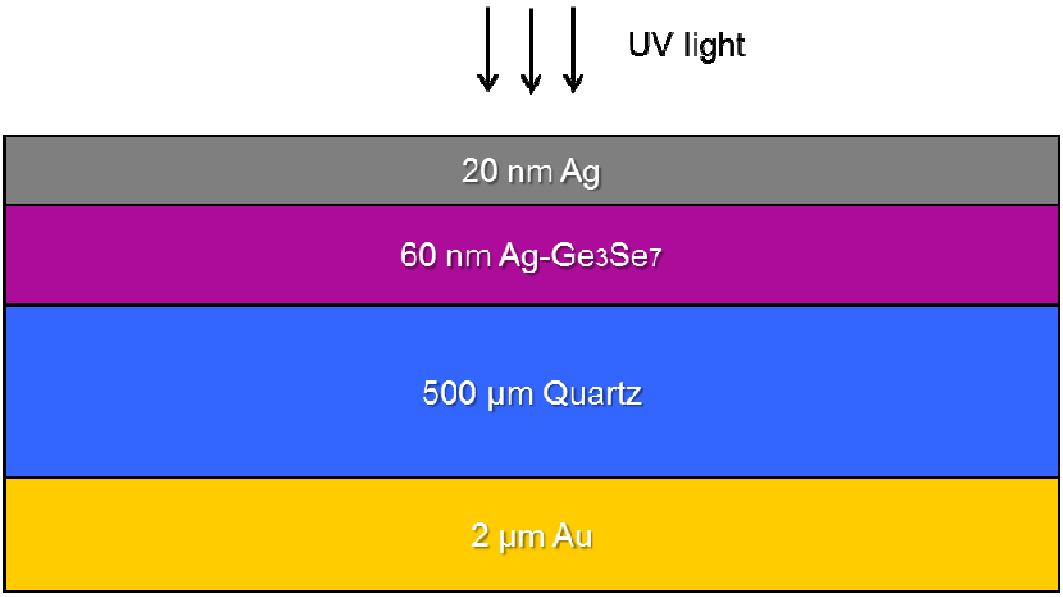

(a) GeSe glass deposition, thin Ag deposition followed by UV sample flood exposure for Ag diffusion and solid electrolyte formation

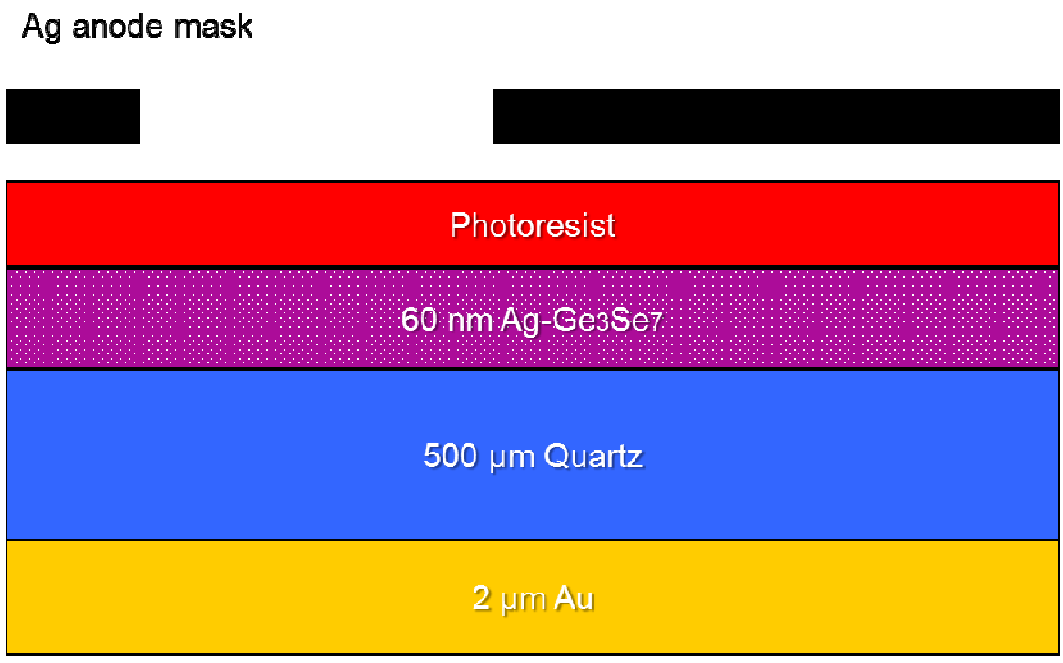

(b) AZ 4330 Photoresist spin for Ag anode lithography

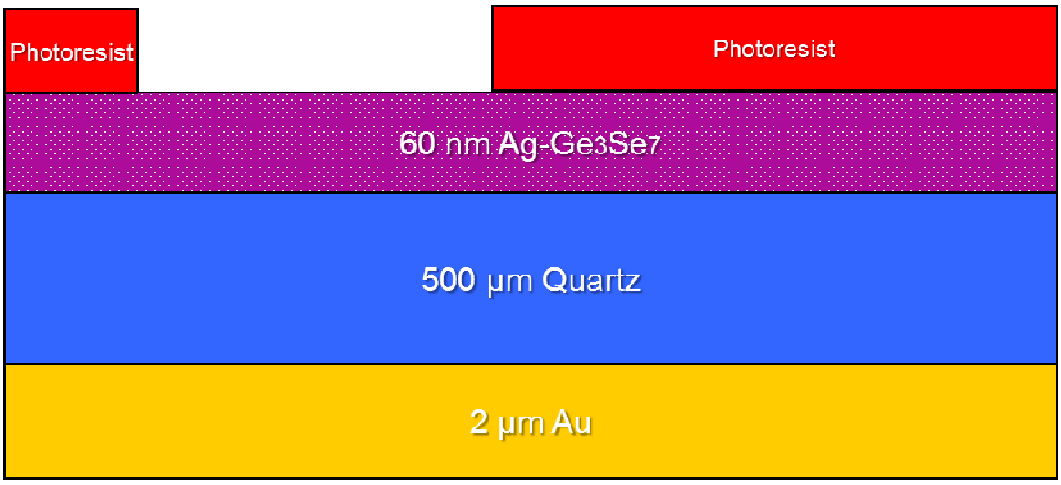

(c) Ag anode patterning and developing

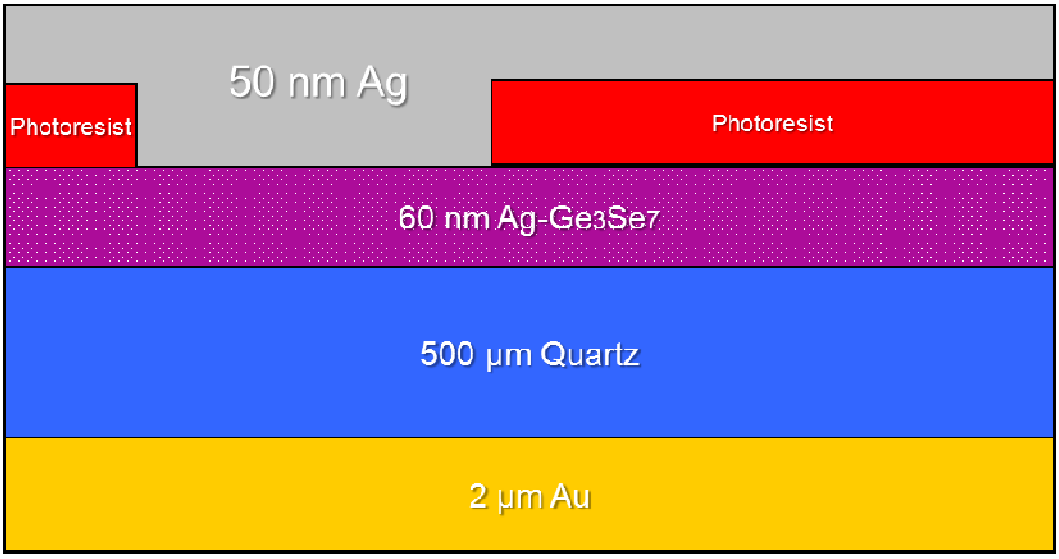

(d) Ag anode electrode metallization

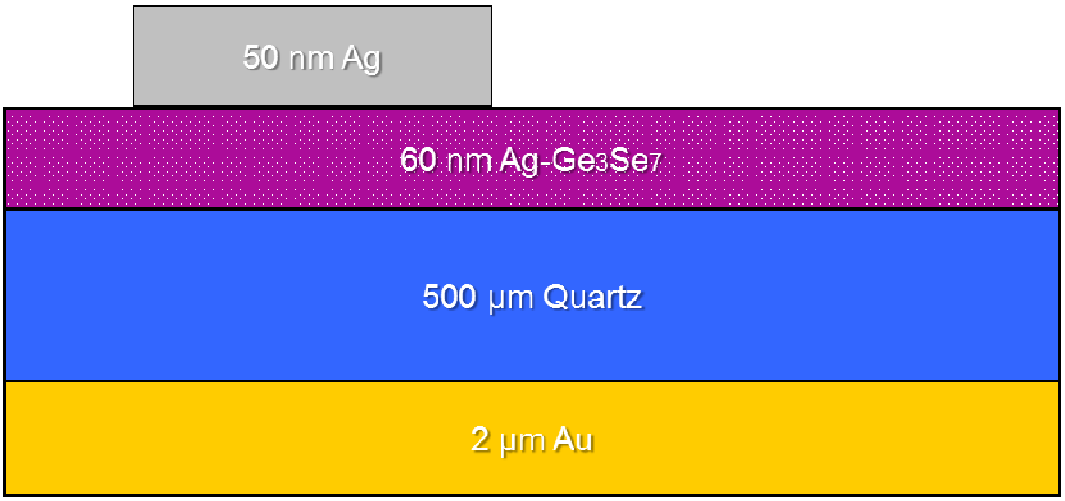

(e) Photoresist lift-off

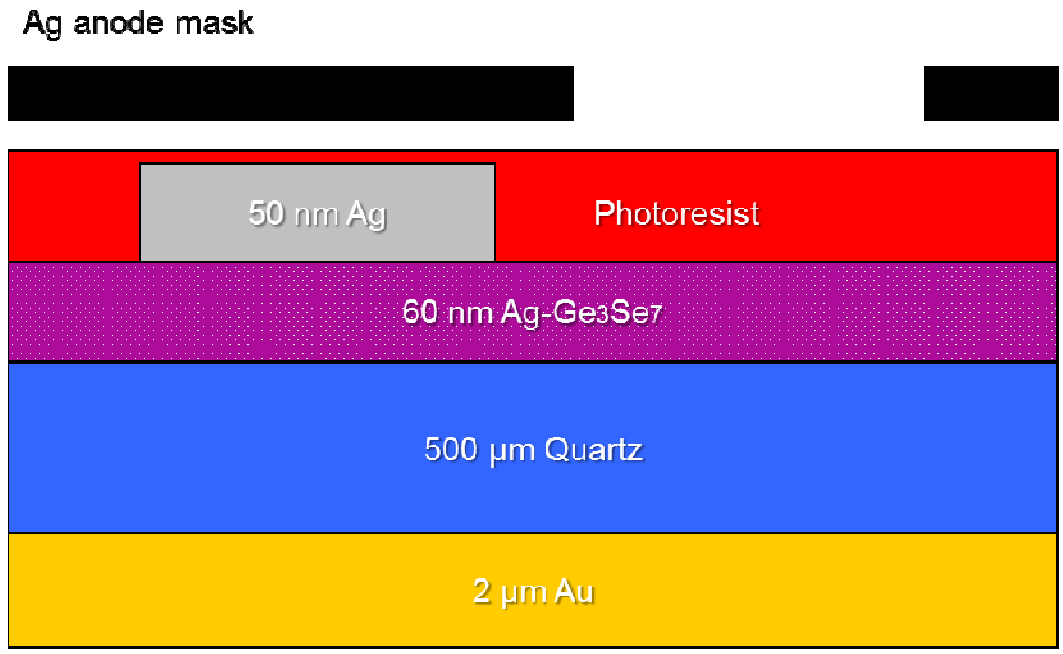

(f) AZ 4330 Photoresist spin for Ni cathode lithography

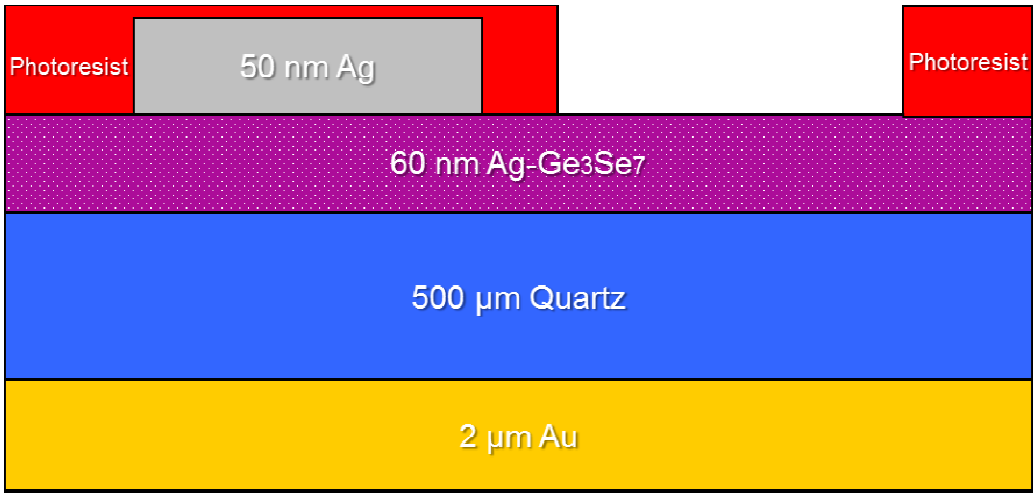

(g) Ni cathode patterning and developing

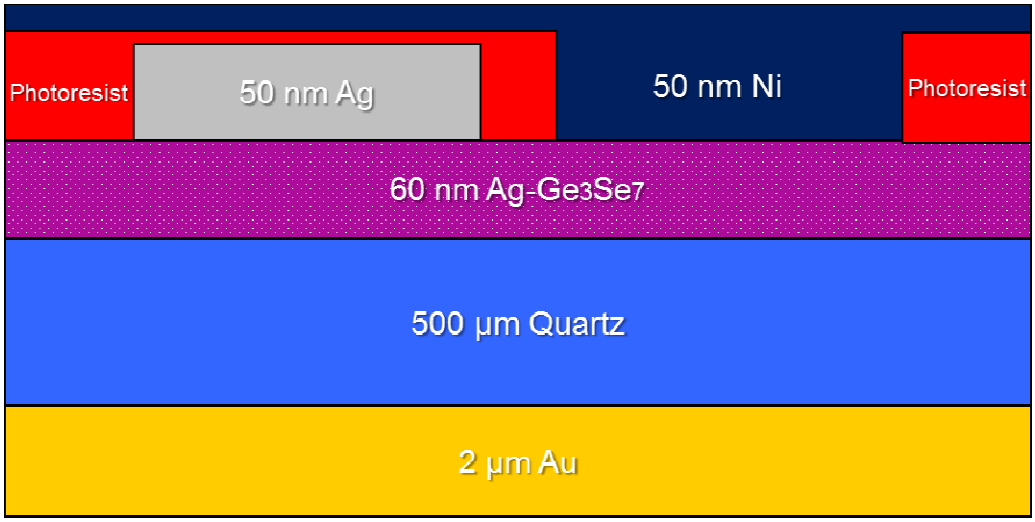

(h) Ni cathode electrode metallization

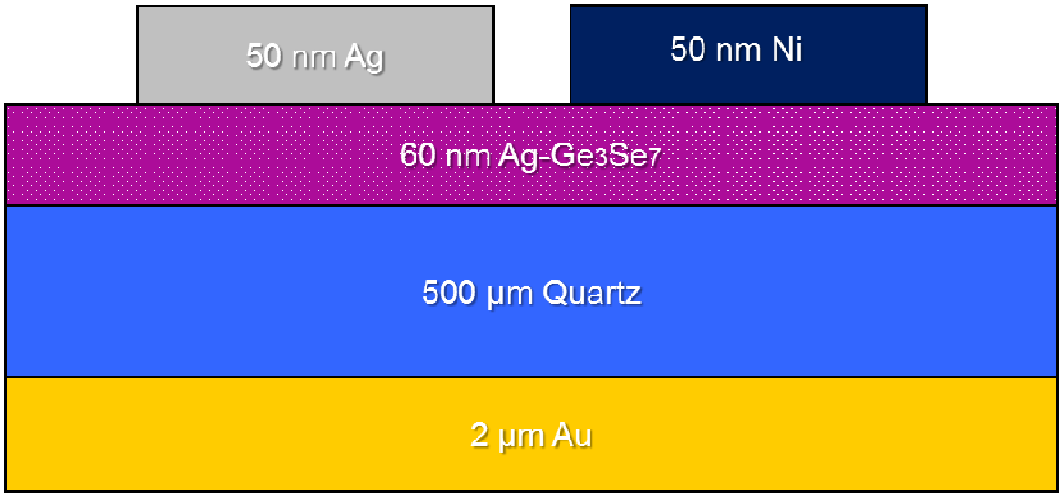

(i) Photoresist lift-off

Fig. 8 Process flow for the fabrication of PMC-based microwave switches with reference design

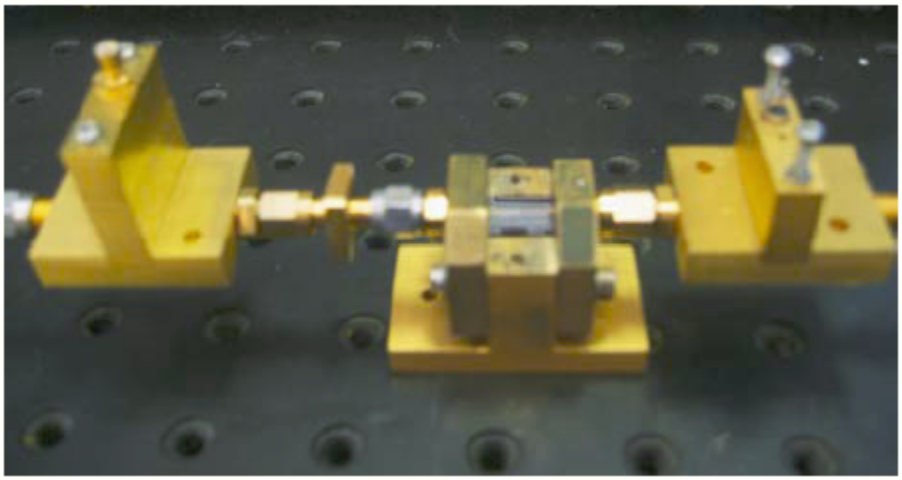

Fig. 9 Chalcogenide-based switch mounted to test structure

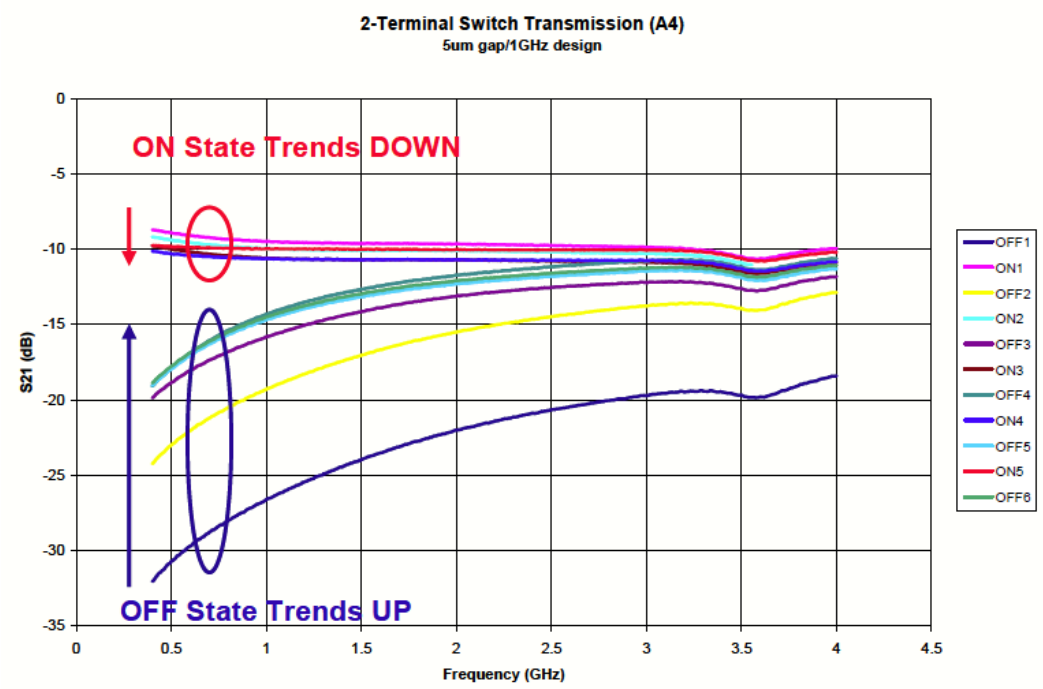

Fig. 10 Representative plot of device performance when cycled between ON/OFF states from400 MHZ to 4 GHz. This particular device contained a 5 μm gap and was designed for 1 GHz operation. Switching was performed utilizing 3V/100mA current limit (tested at GRC)

Initially, the switches tend to show good OFF state isolation at the lower frequency range. For example, at 1 GHz, isolation of better than 25 dB for nearly all devices was observed, with poorer performance as the frequency was increased (regardless of design frequency). A figure of merit for a switch's OFF state isolation is to achieve better than 20 dB isolation, with an optimally configured switch operating at better than 40 dB. The poorer performance of these devices is likely attributable to the coupling through the substrate and the electrode edge. The isolation is determined by the off state capacitance which can be approximated by mainly a series capacitor C_{gap} (see Fig. 11). C_{gap} that is the

coupling between the electrodes including the substrate effect can be estimated by (Ishii)

$$C_{gap} = 0.5[C_0(\varepsilon_{eff}) - 0.5C_e(\varepsilon_{eff})]$$

$$C_0(\varepsilon_{eff}) = 9.6(\varepsilon_{eff}/9.6)^{0.8}(g/w)^{m0}\exp(K_0)w \quad (pF)$$

$$C_e(\varepsilon_{eff}) = 9.6(\varepsilon_{eff}/9.6)^{0.9}(g/w)^{me}\exp(K_e)w \quad (pF)$$

$$m0 = w/h[0.627\cdot\ln(w/h) - 0.3853]$$

$$K_0 = 4.26 - 0.631\cdot\ln(w/h)$$

$$me = 0.8675$$

$$K_e = 2.043(w/h)^{0.12}$$

where the typical width of these electrodes w = 1 mm, the thickness h = 500 μm and the gap between two electrodes g = 2 μm. ε_{eff} is the effective relative permittivity of the substrate and can be calculate by using

$$1/C_{sub} = 1/C_1 + 1/C_2 \rightarrow$$

$$1/(\varepsilon_{eff}\cdot\varepsilon_0\cdot l\cdot w)/h = 1/(\varepsilon_1\cdot\varepsilon_0\cdot l\cdot w)/h_1 + 1/(\varepsilon_2\cdot\varepsilon_0\cdot l\cdot w)/h_2 \rightarrow$$

$$\varepsilon_{eff} = h/(h_1/\varepsilon_1 + h_2/\varepsilon_2)$$

where the typical length of these electrodes l = 5 mm, the thickness of Ge_3Se_7 h_1 = 60 nm, Ge_3Se_7 ε_1 = 60, the thickness of Quartz h_2 = 500 μm and Quartz ε_2 = 3.9. Substituting all the numbers, ε_{eff} is 3.9 and the estimated $C_{gap} \approx 6\times10^{-14}$ F. This value is very close to the OFF state capacitance calculated from the isolation measurement results shown in Fig. 10. The isolation is expressed by

$$Iso = 10\log_{10}\left[1 + \frac{1}{\left(4\pi f c_{off} z_0\right)^2}\right]$$

where f is the frequency, C_{off} is the OFF state capacitance and Z_0 is the characteristic impedance and typically 50 Ω. Using the isolation measurement results (27 dB) in Fig. 10 at 1 GHz, C_{off} is estimated about 7×10^{-14} F. The gap series capacitance, C_{gap}, is the dominant component in the OFF state capacitance and is related to the widths of the electrodes. Thus, by reducing the width of the electrodes, the OFF state capacitance can be lowered and so the OFF state performance can be further improved. Additionally, the OFF state performance worsened as the switch was repeatedly cycled. This is likely a result of the persistence of silver nanowires present within the gap even in OFF state (see Fig. 13 and Fig. 14 discussed later in this section).

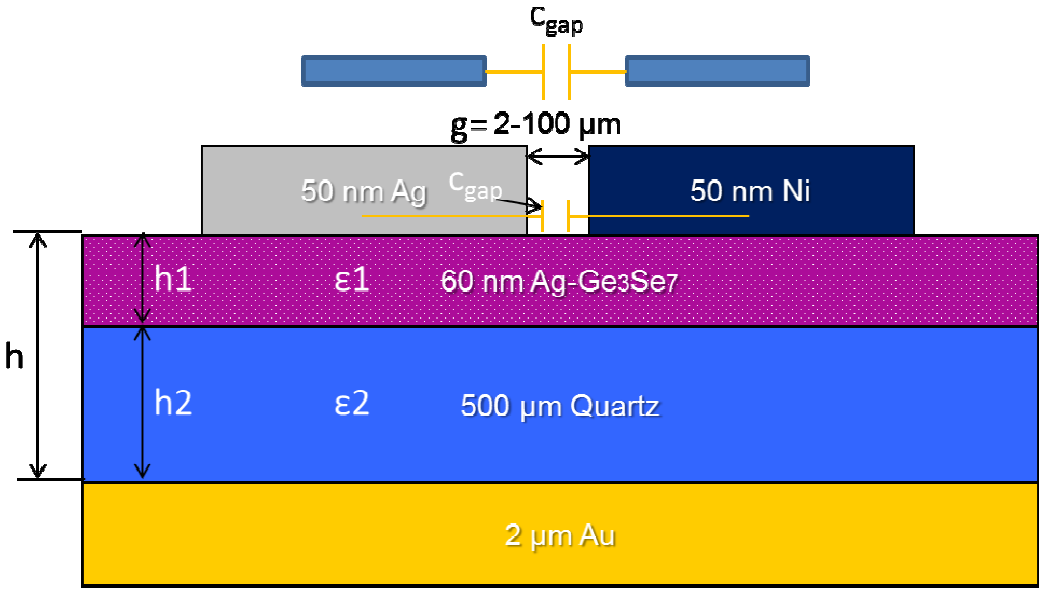

Fig. 11 Schematic drawing of off state capacitance in a PMC-based microwave switch with reference design

In the ON state, insertion losses of approximately 7 to 10 dB were normal and good repeatability over several cycles were maintained at the lower

frequencies. However, a good RF switch should be capable of obtaining better than 1 dB of insertion loss, especially at low frequencies. From the insertion loss measurement results, the ON state resistances can be estimated by using the equation

$$IL = 20\log[1+Rs/(2Z_0)]$$

where Rs is the ON state resistance and Z_0 is the characteristic impedance and typically 50 Ω. At 1 GHz, the insertion loss is about 10 dB and the ON state resistance, including the electrode resistances, metal nanowire (dendrite) resistances and contact resistances, is calculated around 220 Ω. The measured average resistances of these electrodes are about 30 Ω (typically 15 Ω the Ag electrode and 50 Ω for the Ni electrode). The resistance of metal nanowires can be estimated around 0.1 Ω for 10 mA current compliance as the resistance of metal nanowires is proportional to the reciprocal of the compliance current limit (Baliga, Ren and Kozicki). Thus, contact resistances are responsible for the rest of the total ON state resistance.

The high electrode resistance and contact resistances of Ag and Ni electrodes accounts for the increased insertion loss. It will be critical to reduce the resistive loss as much as possible.

Images were taken of several devices when cycled between ON/OFF states. It was identified that at high current limits and/or many cycles, severe degradation of the silver electrode occurred, which can be seen in Fig. 13. It was later determined that this degradation could be delayed by ensuring lower applied current levels as indicated in Fig. 14, where a current limit of 5 mA was utilized.

However, silver electrode degradation still occurred if the device was allowed to repeatedly cycle. Further, lower current limits implies higher resistance nanowires, which impact the insertion loss of the switch when ON, as shown in the S_{21} ON-state plot in Fig. 15. In this example, insertion losses were observed on the order of approximately 12 dB.

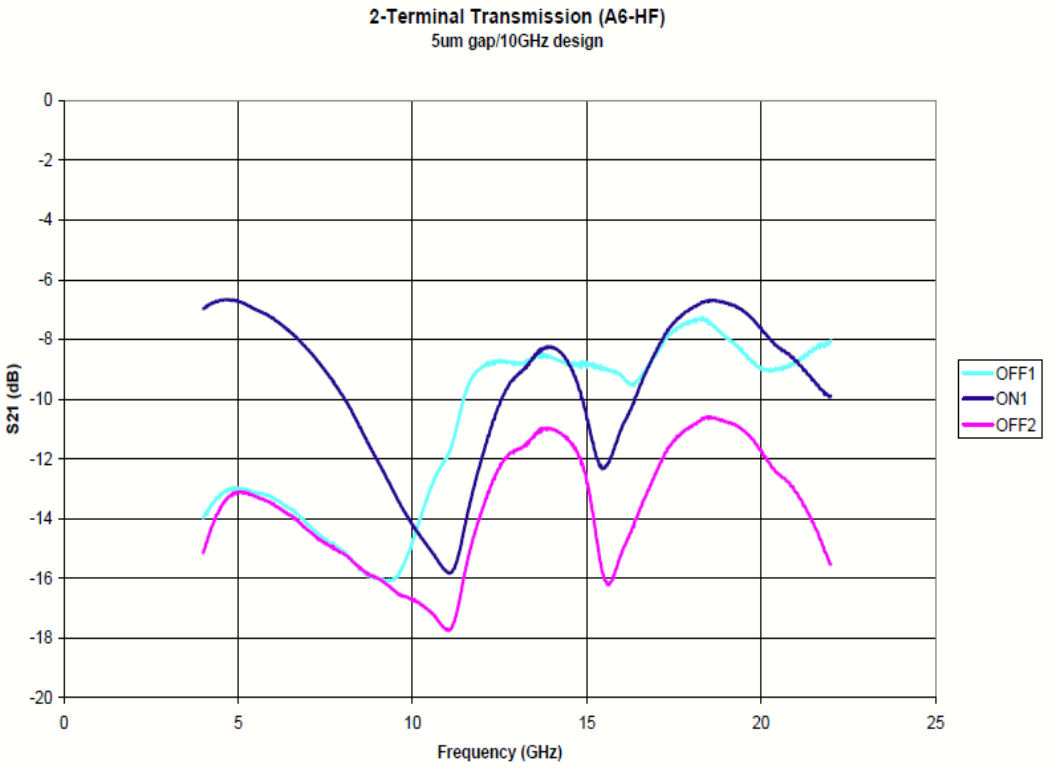

Fig. 12 Representative plot of device performance when cycled between ON/OFF states from 4 GHz to 22 GHz. This particular device contained a 5 μm gap and was designed for 10 GHz operation. Switching was performed utilizing 2V/100mA current limit (tested at GRC)

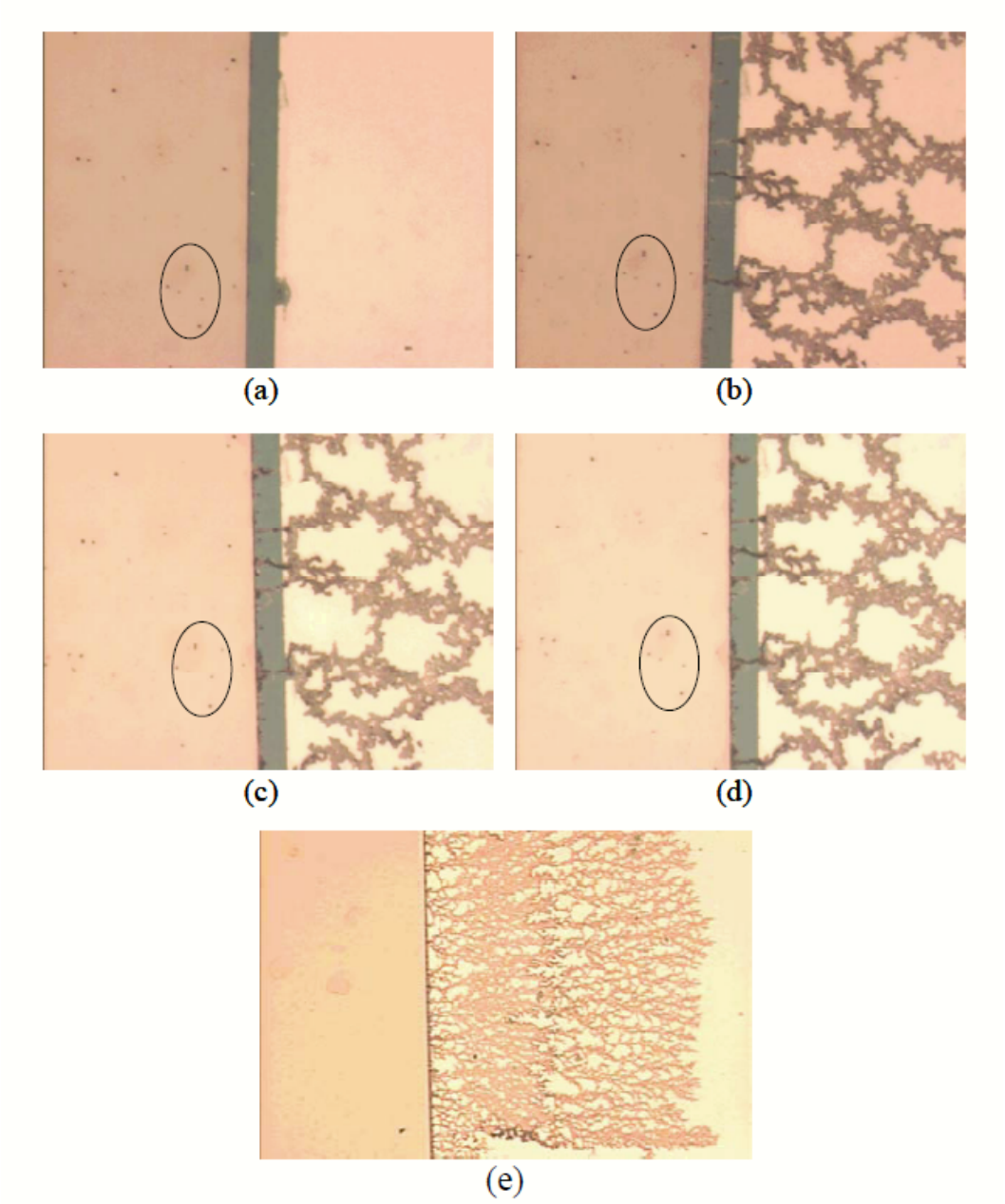

Fig. 13 Photographs of electrodes in (a) initial state, (b) ON1 state, (c) OFF2 state, (d) ON2 state, and (e) FAIL state (zoomed out). Circles provide a reference from photograph to photograph. Device: 10um gap using a 2V/20mA current limit (tested at GRC)

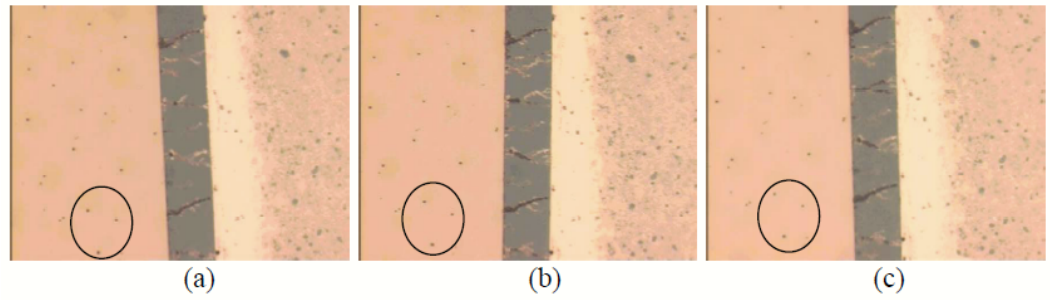

Fig. 14 Photographs of electrodes in (a) initial state, (b) ON1 state, and (c) OFF2 state. Circles provide a reference from photograph to photograph. Notice no significant degradation in silver electrode. Device: 20um gap using a 1V/5mA current limit (tested at GRC)

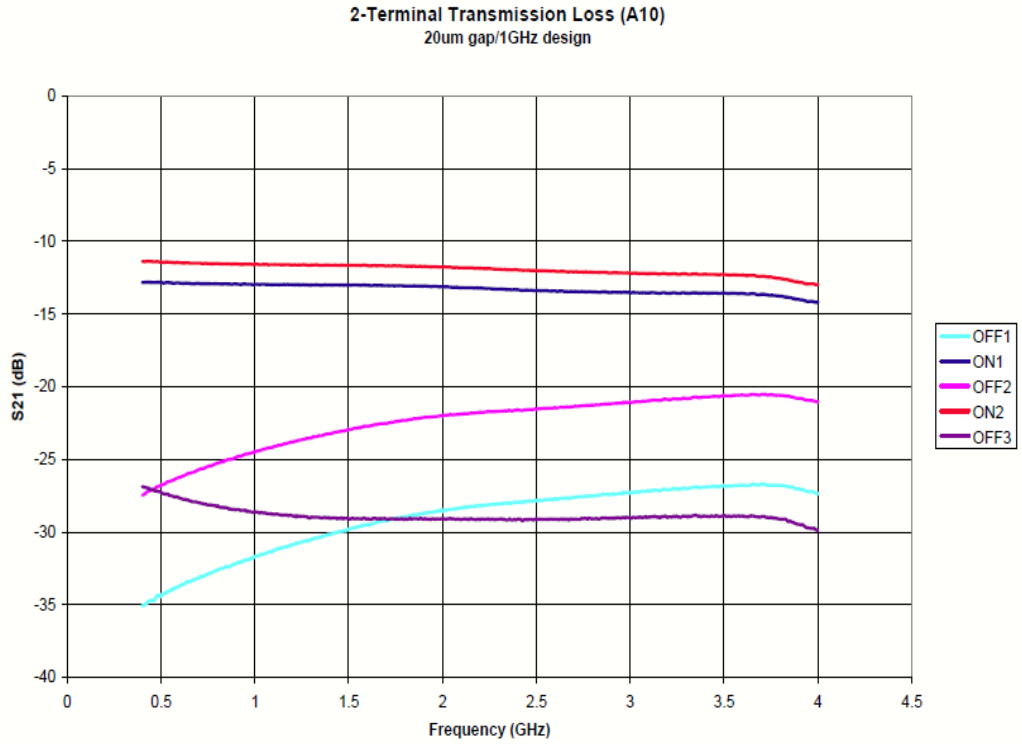

Fig. 15 Plot of device performance when cycled between ON/OFF states from 400 MHz to 4 GHz. The lower current limit results in higher ON state insertion loss (12 dB). This particular device contained a 20 μm gap and was designed for 1 GHz operation (tested at GRC)

2.3.3 Reference design with Au-plated electrodes

The switches with the reference design were coated with ~2 μm thick Au to improve the resistive loss (see Fig. 16). The process flow for the fabrication is almost the same as the previous reference design except Au plating for the top electrodes. Au plating was performed at GRC. The insertion loss results are shown in Fig. 17. From the insertion loss measurement results, the ON state resistances can be estimated around 5.9 Ω by using the equation

$$IL = 20\log[1+Rs/(2Z_0)]$$

where Rs is the ON state resistance and Z_0 is the characteristic impedance and typically 50 Ω. Thicker electrodes significantly improve the ON state performance by reducing the electrode resistances and contact resistances compared to the reference design's 220 Ω ON state resistance, but unfortunately also worsen the OFF state performance due to higher capacitive edge coupling. In this design, the capacitive coupling was increased owing to that the thicknesses of the electrodes were increased by 40 times (the added Au layers are 2 μm thick and are 40 times the original Ag and Ni layers which are only 50 nm thick) as the capacitance is strongly related to the thickness of the electrodes. A taper width of transmission line can be designed to decrease the edge coupling capacitance by reducing the area.

2.3.4 Serrated tapered design

To improve the OFF state performance, the anode and cathode electrodes both were redesigned to have multiple tapered edges towards the gap (Fig. 18). The process flow for the fabrication is the same as the previous reference design

with Au plating for the top electrodes. The typical switch characteristics are shown in Fig. 19. The OFF state performance showed a slight improvement over the previous iteration due to the reduced edge coupling capacitance which results from a small decrease of the widths of the electrodes and a little increase of the average distance between the electrodes, while still possessed good ON state performance. However, large silver electrodeposits (Fig. 20) which were created during switching process were observed due to serration and become difficult to remove. After a few cycles, these large residual silver electrodeposits seriously worsened the OFF state performance.

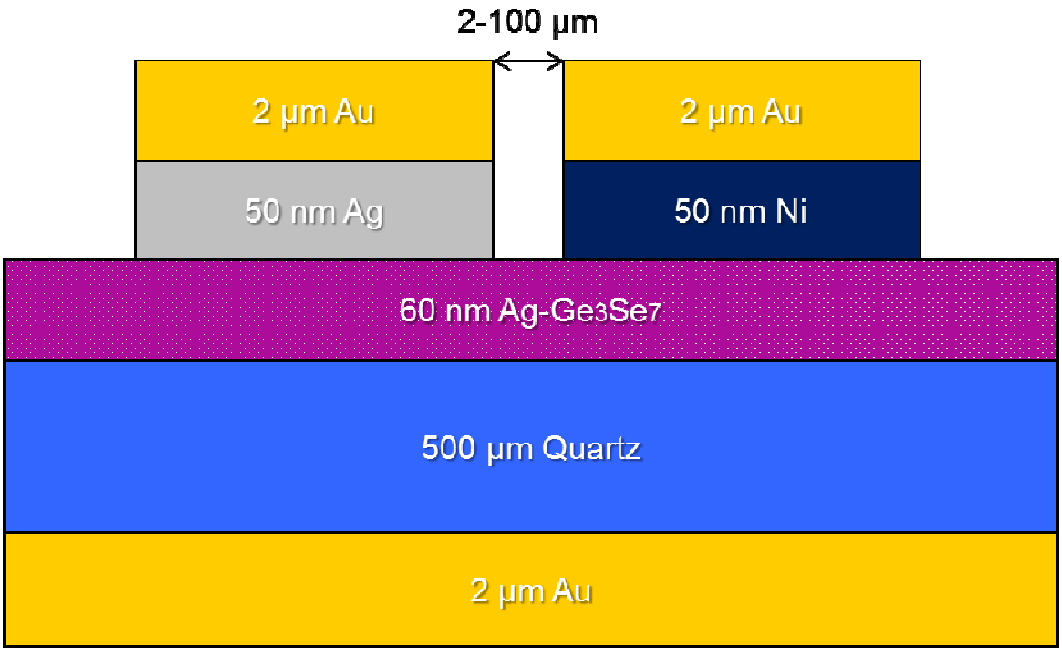

Fig. 16 Schematic of a PMC-based microwave switch with reference design and Au-plated electrodes

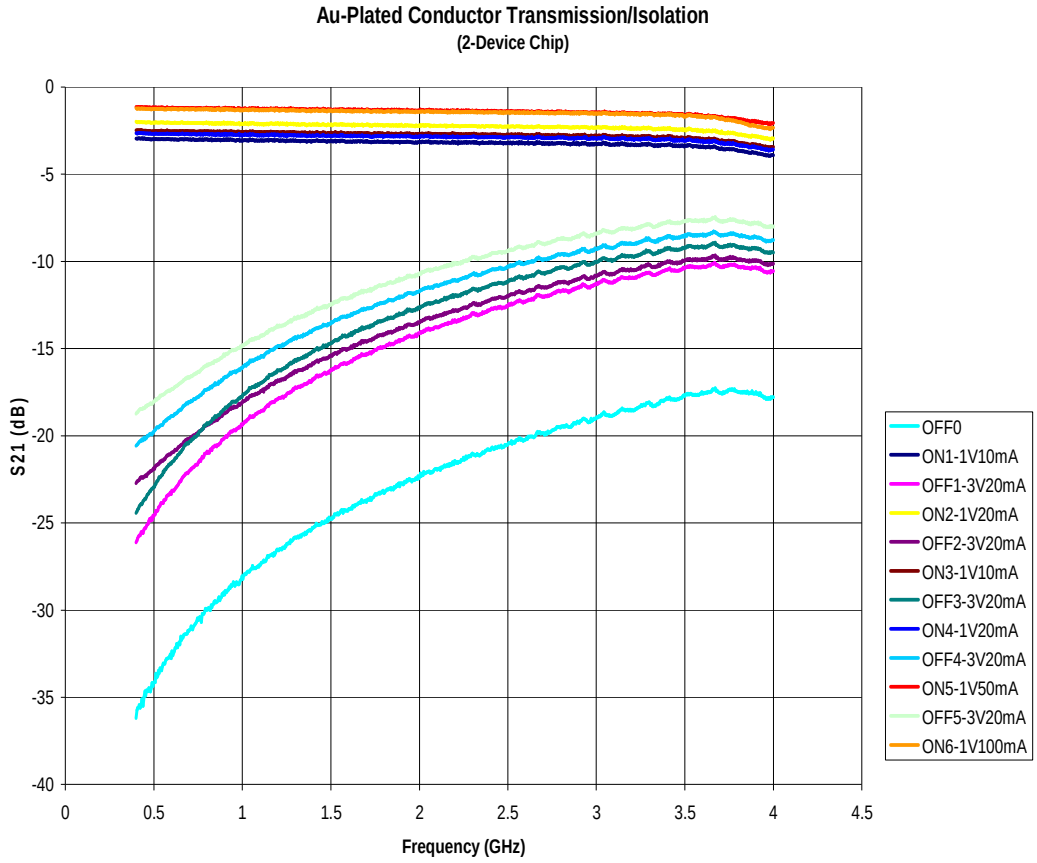

Fig. 17 Initial insertion loss (S21) of the reference switch in the ON state has improved to better than -5 dB over the 1 to 4 GHz range, while the isolation (S21) in the OFF state is better than -15 dB (initially), but continues to worsen over several cycles. After 6 cycles, the distinction between ON and OFF is still evident, but not good enough (tested at GRC)

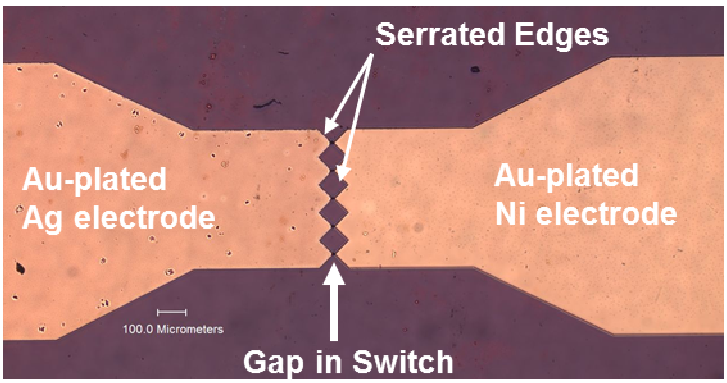

Fig. 18 Microphotograph of coplanar nanoionic switch serrated tapered design (tested at GRC)

2.3.5 Tapered design

To reduce the serration effect while preserve the taper electrode design, the serrated anode and cathode electrodes were modified to a single-tapered-tip transmission line which tapers to a higher impedance thin extension (narrowed width) towards the gap. This design proves to be the best out of four iterations and shows an insertion loss of ~0. 5 dB, isolation of >30 dB, low voltage operation (1V), low power (~μW) switching, and excellent linearity up to 6 GHz (Nessel et al.). The fabrication and characterization will be presented in detail in the following section.

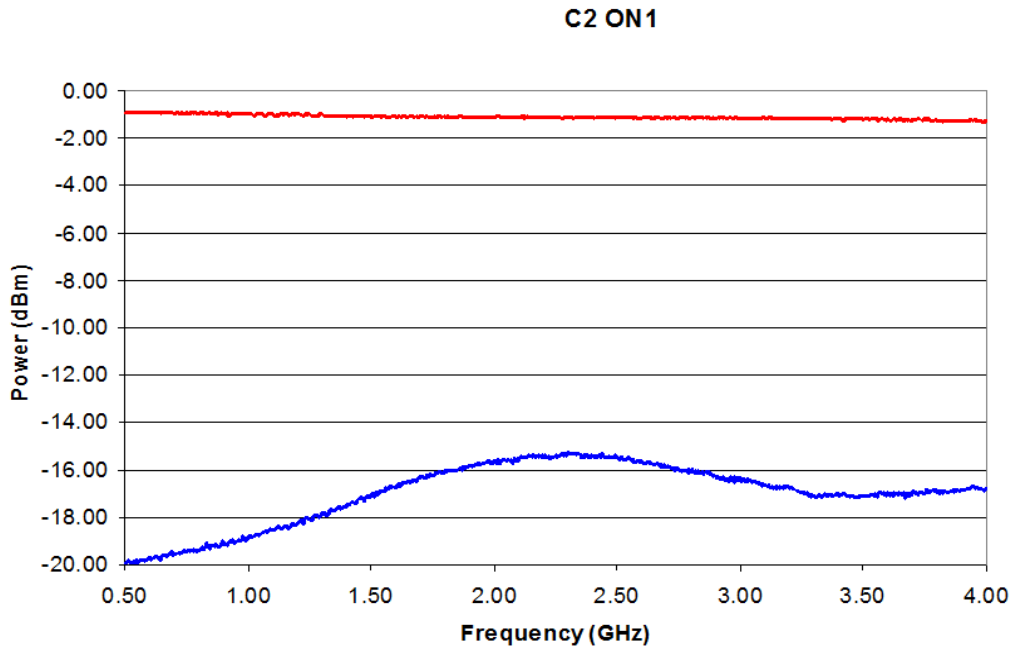

Fig. 19 Both ON state (RED) and OFF state (BLUE) are better than previous two design iterations but not as good as the tapered design iteration which will be discussed in the next section (tested at GRC)

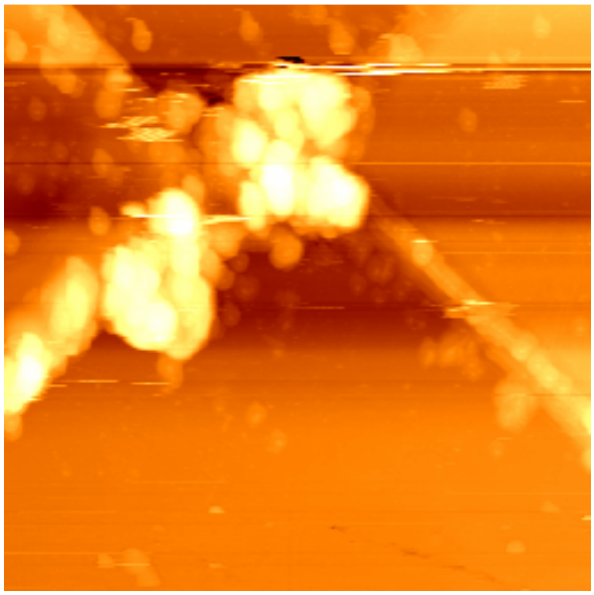

Fig. 20 Atomic Force Microscope image of silver growth in gap at a serrated edge. Note the rather large formation of silver right at the electrode tip (tested at GRC)

2.4 PMC-based microwave switch fabrication

The tapered design of a microwave series switch is based on a simple two electrode coplanar geometry comprising a bottom ground electrode, a quartz substrate, the solid electrolyte, an Au-plated inert electrode (Ni) and an Au-plated oxidizable electrode (Ag), and a passivation layer. To fabricate the test structures, a 60 nm thick Ge_3Se_7 layer was deposited by thermal evaporation (Edwards 1) onto a 500 µm thick quartz substrate with a pre-deposited Au ground plate. A 20 nm thickness Ag layer was deposited in the same equipment and was dissolved into the base glass by photodissolution at room temperature using exposure to ultraviolet light from a 405 nm broadband source with an energy density at the wafer surface of 1 J/cm2. Following photodissolution, a 50 nm thick Ni cathode was deposited by electron beam evaporation (CHA1) and an additional 50 nm thick Ag anode was added by thermal evaporation (Edwards 1) to ensure a continuous oxidizable source for electrodeposition. A simple photoresist passivation layer atop the "active" area was implemented to provide protection (Nessel et al.). Both electrodes (Ag anode, Ni cathode) are Au-plated to 2 µm thick. Note that the tapered lines in the electrode tips were not Au-plated as they were passivated by the passivation layer and therefore the thicknesses of these lines were not increased by the added Au layers. A gap of 10 µm separates the two electrodes. Within this gap, an Ag-saturated Ge_3Se_7 electrolyte represents the active area of the device. A representative circuit layout can be seen in the microphotograph of Fig. 21 and a device cross section is shown in Fig. 22 (c). A 50-transmission line tapers to a higher impedance (narrowed width) towards the

gap. This tapering effect helps to reduce capacitive coupling in the switch in the OFF state, but remains the primary source of loss in the ON state. Please refer the process flow for the fabrication of this microwave switch with the tapered design to Fig. 8 and Fig. 22. Fig. 22 supplements the extra processing steps, which are not included in Fig. 8, to complete the device.

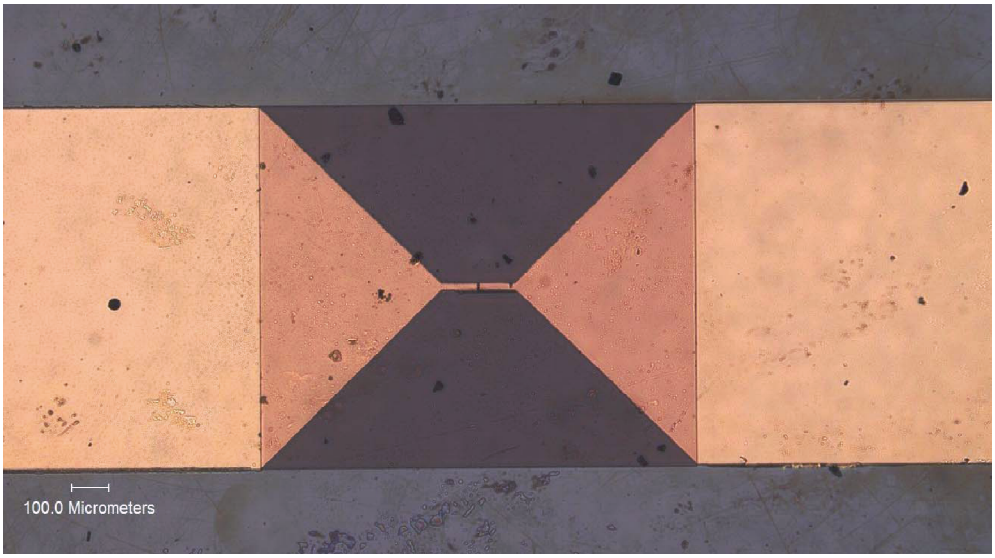

Fig. 21 Microphotograph of tapered coplanar PMC switch design (tested at GRC)

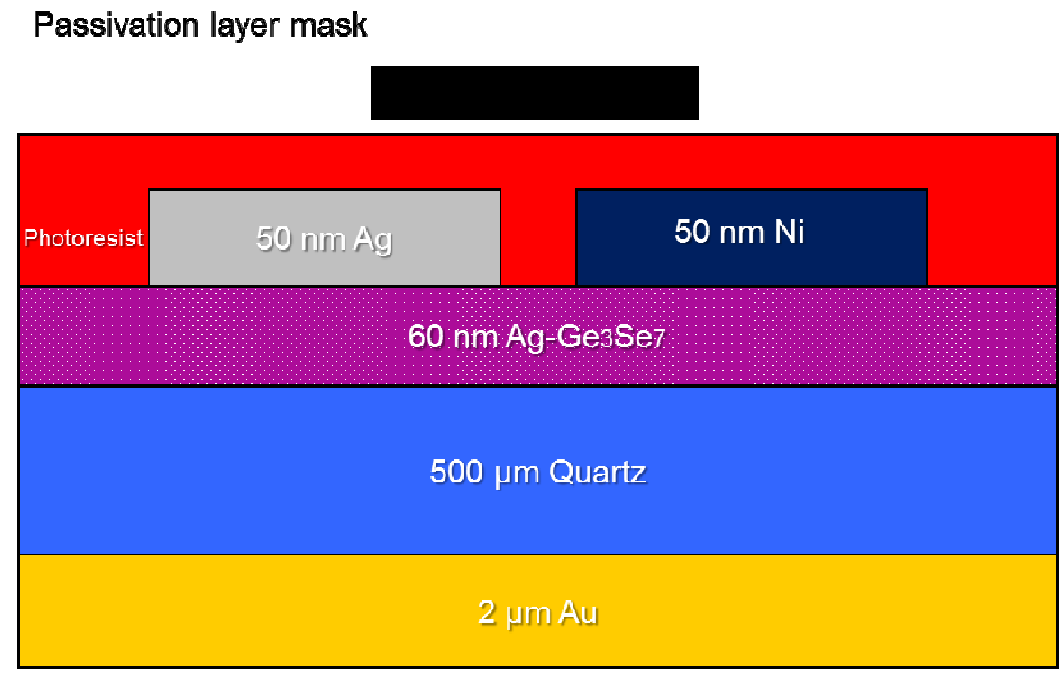

(a) AZ 4330 Photoresist spin for passivation layer lithography

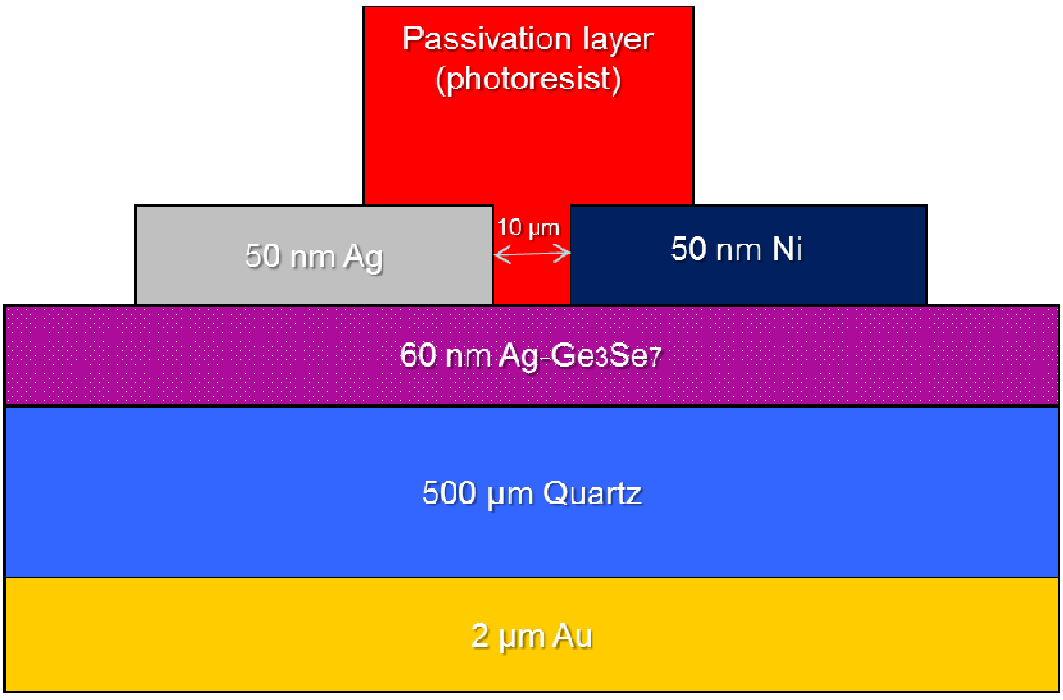

(b) Passivation layer patterning and developing

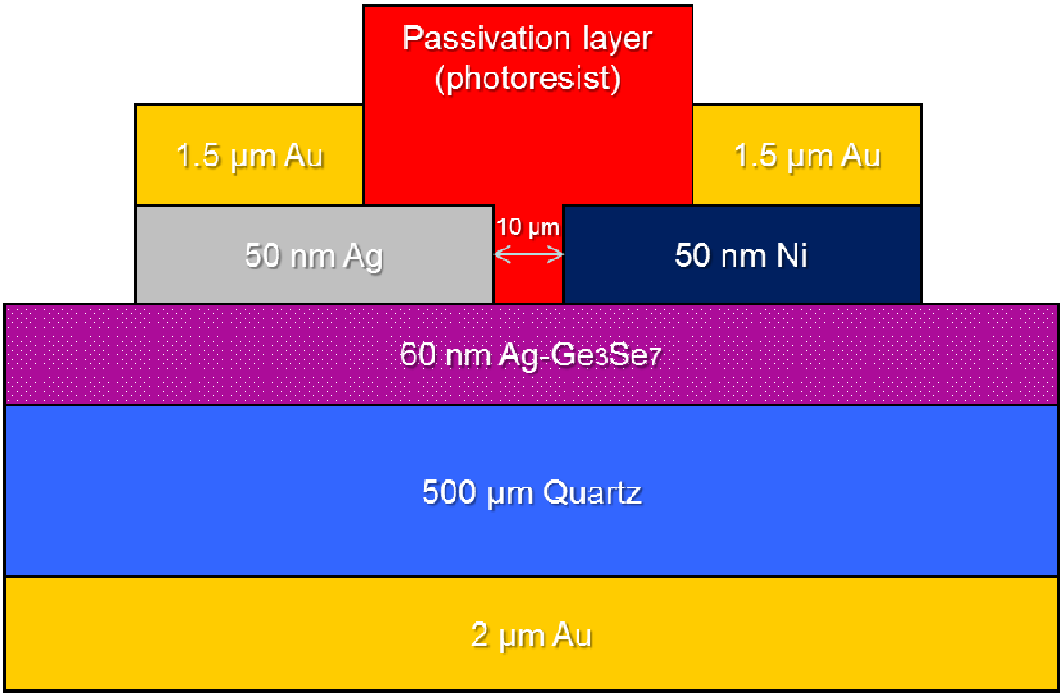

(c) Au plating for top electrodes (performed at GRC)

Fig. 22 Extra process flow for the fabrication of PMC-based microwave switches with tapered design

To operate the device, a voltage of 1V and a current limit of 10 mA were used. Increasing voltages improved growth rates, whereas lifting current limits reduced the overall resistive loss of the electrochemically grown metallic dendrites, but induced higher power requirements to operate the switch. A positive voltage relative to the Ni (inert) electrode is applied to enable silver growth and set the device to the ON state. Reversing polarity of the applied voltage erases the electrochemically grown silver and sets the device into the OFF state. Fig. 23 is a microphotograph of the conductive metallic pathways that form when the device is ON. From the inset of Fig. 23, an atomic force microscope

image shows that much of the silver growth occurs on the surface of the thin film (Nessel et al.).

2.5 Measurement and results

2.5.1 Insertion loss and isolation

To measure the microwave performance of the device, test samples were individually diced and mounted onto a brass mounting fixture (Fig. 9). The circuit was connected to an Agilent E8361A Vector Network Analyzer in order to measure ON state insertion loss and OFF state isolation. An Agilent E3646A DC Power Supply was utilized to provide the necessary voltage/current to change the state of the device (nominally 1V/10mA (ON) and -1V/10mA (OFF)). A plot of these results is shown in Fig. 24 for a typical nanoionic switch. From the plot, it is observed that an ON state insertion loss of ~0.5 dB is achievable, with an OFF state isolation of better than 35 dB over the DC to 6 GHz band. The series gap capacitance, C_{gap}, that is the coupling between the electrodes including the substrate effect and also the dominant component in the OFF state capacitance can be estimated by (Ishii)

$$C_{gap} = 0.5[C_0(\varepsilon_{eff}) - 0.5C_e(\varepsilon_{eff})]$$

$$C_0(\varepsilon_{eff}) = 9.6(\varepsilon_{eff}/9.6)^{0.8}(g/w)^{m0}\exp(K_0)w \quad (pF)$$

$$C_e(\varepsilon_{eff}) = 9.6(\varepsilon_{eff}/9.6)^{0.9}(g/w)^{me}\exp(K_e)w \quad (pF)$$

$$m0 = w/h[0.627\cdot\ln(w/h) - 0.3853]$$

$$K_0 = 4.26 - 0.631\cdot\ln(w/h)$$

$$me = 0.8675$$

$$K_e = 2.043(w/h)^{0.12}$$

where the width of these electrodes w = 20 μm, the thickness h = 500 μm, the gap between two electrodes g = 5 μm and the effective relative permittivity of the substrate ε_{eff} = 3.9. The estimated $C_{gap} \approx 3\times10^{-14}$ F by substituting all the numbers into the equations. The OFF state capacitance can be calculated from the isolation measurement results shown in Fig. 10. The isolation is expressed by

$$Iso = 10\log_{10}\left[1 + \frac{1}{\left(4\pi f c_{off} z_0\right)^2}\right]$$

where f is the frequency, C_{off} is the OFF state capacitance and Z_0 is the characteristic impedance and typically 50 Ω. Using the isolation measurement results (40 dB) in Fig. 10 at 1 GHz, C_{off} is estimated about 2×10^{-14} F. This value calculated from the measurement results is very close to the estimated C_{gap} and agrees very well with the prediction made in section 2.4.2 which stated that the OFF state capacitance can be lowered by reducing the widths of the electrodes. In this design the 20 μm tapered transmission line was 50 times smaller than the reference design which has 1 mm wide electrodes.

These measured results are comparable to MEMS and solid state-based RF switch performance in the same frequency range. At frequencies much greater than this, the series switch design tends to perform poorly, maintaining good insertion loss characteristics, but reducing isolation (due to capacitive edge coupling at the gap). Further, repeatability of this performance over several cycles also requires improvement (Nessel et al.).

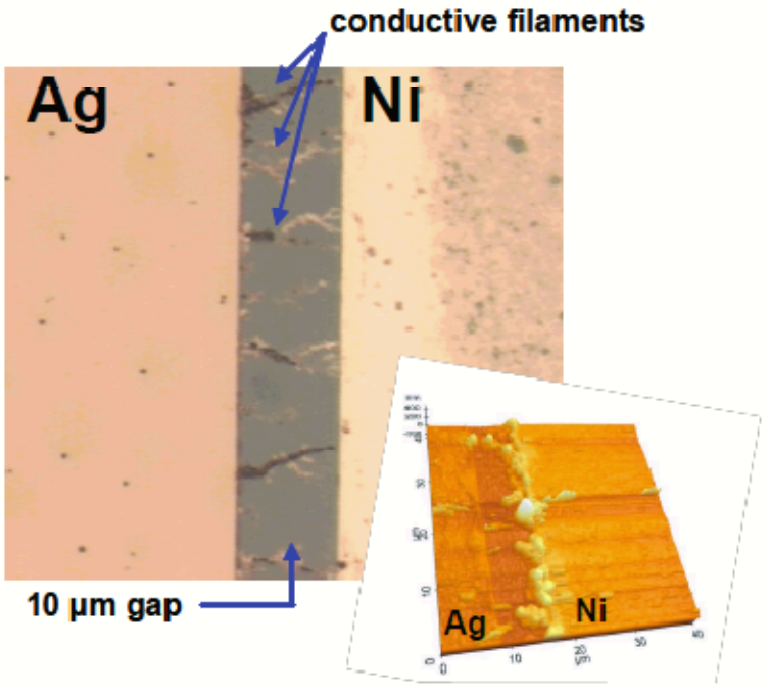

Fig. 23 Microphotograph (larger image in figure) and associated Atomic Force Microscope (AFM) image (smaller inset on right) of PMC-based switch in the ON state (tested at GRC)

2.5.2 Linearity and power handling

Power measurements were performed using an Anritsu ML2437A power meter and Anritsu MG3691B signal generator. A switch was mounted on the same brass mounting fixture while various frequencies (500 MHz – 4 GHz) of varying power were fed into a switch. Attenuation pads at the input and output to the switch were used to reduce signal reflection within the system. Frequency and power range limits were determined by the dynamic range of the signal generator and available components. From Fig. 25, devices, typically demonstrated linearity over the range of measured power from -20 dBm to +20 dBm, were observed, with device breakdown typically occurring at ~400- 500 mW. Further, no change

is evident in the power transfer curve at different frequencies of operation, demonstrating the device's wide bandwidth operation potential (Nessel et al.).

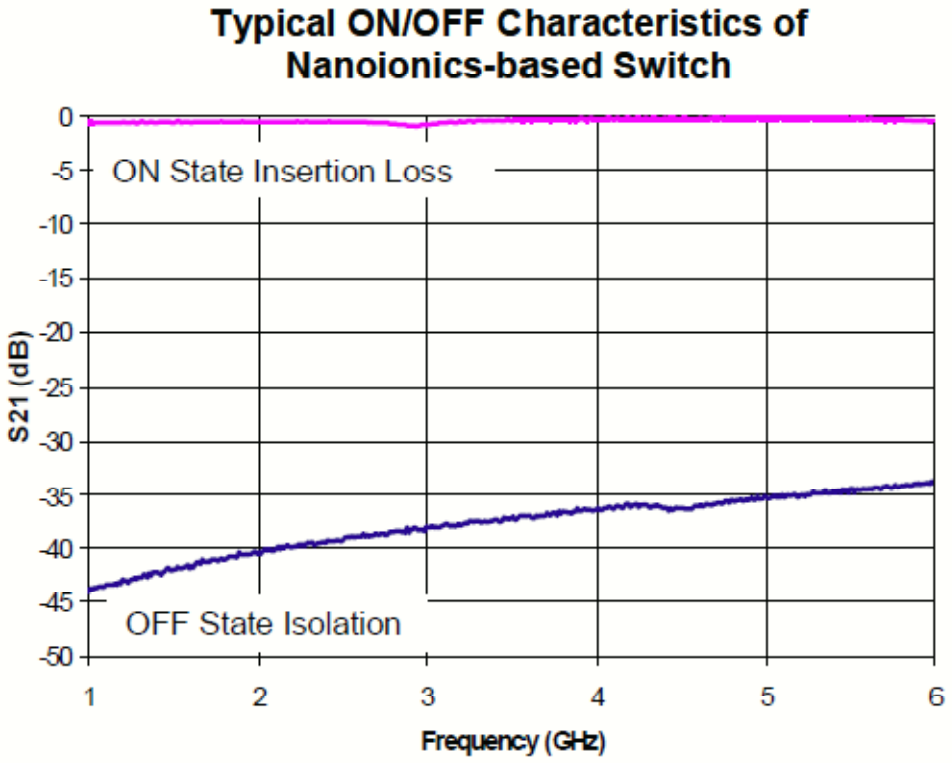

Fig. 24 The insertion loss (S21) of the switch in the ON state is better than -0.5 dB over the 1 to 6 GHz range (commercial ISM Band), while the isolation in the OFF state is better than -35 dB (Nessel et al.).

2.5.3 Speed

The travelling distance of the electrodeposit regulates the speed of operation of the nanoionic switch. The wider the gap between electrodes is, the longer the response time of the switch is. Though the switching speed was not directly measured, results inferred from (Michael N. Kozicki et al.) indicate that the electrodeposition rate of silver within a chalcogenide glass can reach at a

velocity of approximately 1 nm/ns. Therefore, for a 10 μm gap, a switching speed of around 10 μs is expected. Apparently the smaller the gap size is, the faster the switch operation is, but other considerations such as OFF state isolation limit the optimization of speed, at least for a coplanar-type structure (Nessel et al.).

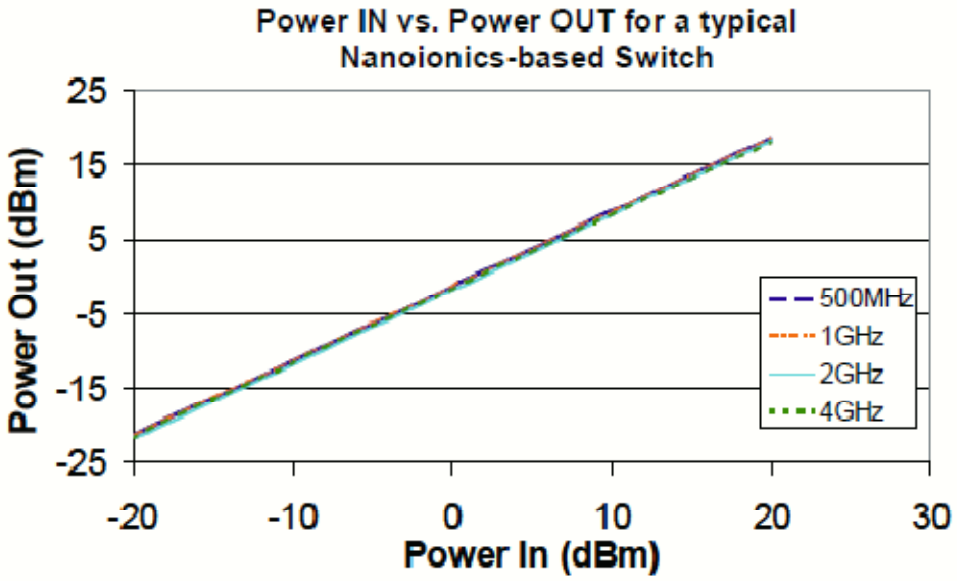

Fig. 25 Power transfer curve of a typical PMC-based switch over its operating range for frequencies between 500 MHz and 4 GHz (Nessel et al.).

3. PMC-BASED DENDRITIC ELECTRODE

3.1 Introduction

The photovoltaic industry has been booming for almost a decade in request of new clean and sustainable energy alternatives in place of fossil fuels, and the majority of new manufacturing capacity is based on traditional screen-printed solar cell technology which takes well over 50% share of international markets. In spite of the maturity of this technology, the cell design still suffers from a number of performance limitations that reduce the cell efficiencies. One of them is front screen-printed contacts (Mai et al.).

Using screen printed contacts is a performance/cost trade-off, pointed out by Green and his colleagues from the University of New South Wales (UNSW) (Miles, Hynes and Forbes). Major factors that contribute to the performance/cost trade-off include high shading losses, high resistivity of the screen printed silver grids compared to pure silver (3× as high), high contact resistance between the grid and silicon and poor aspect ratio (Miles, Hynes and Forbes). All these factors combine to reduce device efficiencies to approximately 14% (Miles, Hynes and Forbes).

The top contact electrode is often formed as a series of wide bus bars with somewhat narrower branches extending between them. The dimensions of these electrodes (e.g., their line widths and the spaces between them) are generally large due to manufacturing cost limitations. The relatively large space between electrodes can create a high series resistance between the current generating sites and the top electrode, leading to inefficient energy collection from the areas of the

current generating structure that are farthest from the electrodes. Packing the electrode structures more tightly is not a suitable solution, as a greater amount of electrode material will shield the current generating material from solar radiation, thereby rendering it useless for energy generation. Accordingly, using conventional techniques solar cell designers have to sacrifice efficient current collection in order to avoid blocking too much of the absorber layer from light, leading to an inefficient use of the current collecting material, and therefore to lower energy generated per unit area.

A PMC-based dendritic metal electrode was developed to be potentially integrated with solar cell devices. A metallic dendritic network can be grown in a solid electrolyte to harvest current, or grown on either insulator like SiO_2 or semiconductor like Si using water-mediated method without involving any solid electrolyte.

These dendritic structures can make possible optimizing the top contact electrode with minimized resistance and shading loss if they provide sufficient lateral conductivity without sacrificing a big deal of light transmission. The real estate taken by the conventional screen-printed top metallization could be significantly cut down and the shading loss could be greatly minimized as a result.

In this chapter, a review of the solar cell technologies is presented first, followed by the introduction and discussion of the dendritic electrode technology.

3.2 Solar cell technology overview

The photovoltaic effect was first discovered in 1839 by French physicist A. E. Becquerel. In1883, Charles Fritts built the first solar cell by coating a thin layer

of gold onto the semiconductor selenium to create the junctions but the device at that time was only around 1% efficient. It was not until 1954 that the first practical solar cell device was built when Bell Laboratories by accident discovered that silicon doped with certain impurities could be light-sensitive (Wikipedia "Solar Cell from Wikipedia, the Free Encyclopedia").

Extensive research has been done on exploiting photovoltaic effect for energy conversion and a handful of materials and processes can potentially realize it, but in reality nearly all photovoltaic energy conversion employs the form of p-n junction in connection with semiconductor materials (Bowden).

Fig. 26 shows how a solar cell directly converts sunlight into electricity. Incident sunlight with energy greater than that of the band gap that hits on the solar cell can generate electron-hole pairs (Bowden). The electrons and the holes are separated by the existing electric field inside a p-n junction. The connected emitter and base of the solar cell are utilized to collect the electrons and the holes and allow the light-generated carriers to flow through the external circuit to generate current (Bowden). However, these electrons and holes will exist, on average, for a length of time equal to the minority carrier lifetime before they recombine (Bowden). This recombination will kill then the light-generated electron-hole pair and no current can be produced (Bowden).

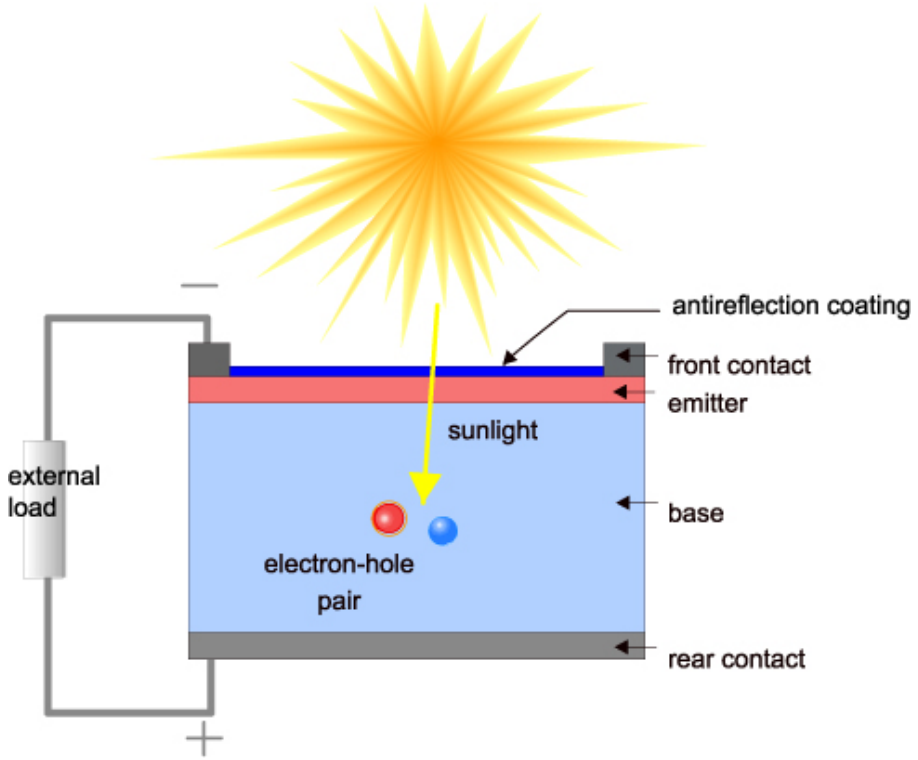

Fig. 26 Cross section of a solar cell (Bowden).

3.2.1 Equivalent circuit of a solar cell

An ideal solar cell may be modeled by a current source in parallel with a diode; in real life an ideal solar cell does not exist and thus a shunt resistance and a series resistance component may be added to the model. The resulting equivalent circuit of a solar cell is shown in Fig. 27 (Wikipedia "Solar Cell from Wikipedia, the Free Encyclopedia").

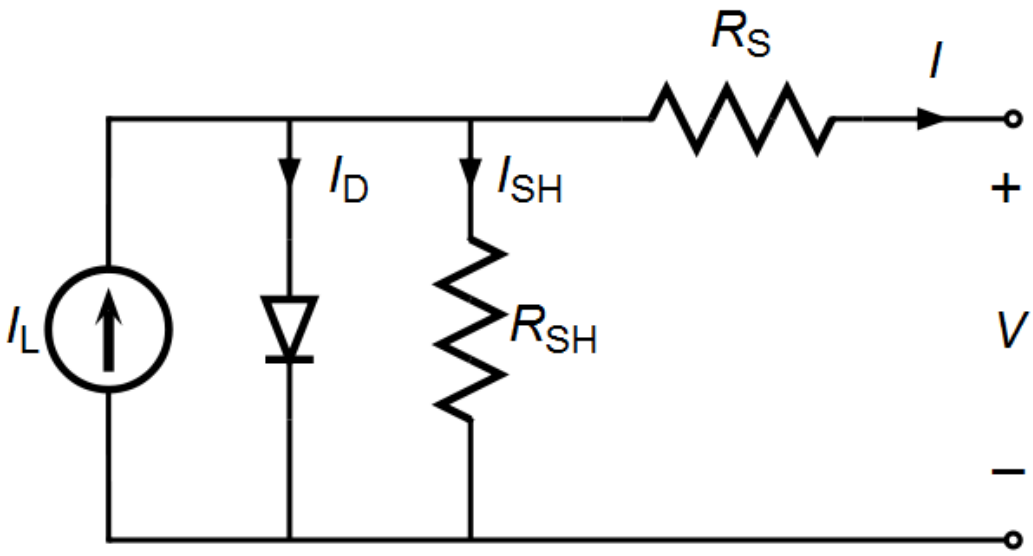

Fig. 27 equivalent circuit of a solar cell (Wikipedia "Solar Cell from Wikipedia, the Free Encyclopedia"),

3.2.2 Characteristic equation

From the equivalent circuit it is obvious that the current produced by the solar cell can be expressed by (Wikipedia "Solar Cell from Wikipedia, the Free Encyclopedia")

$$I = I_L - I_D - I_{SH}$$

where

I = output current (A)

I_L = photogenerated current (A)

I_D = diode current (A)

I_{SH} = shunt current (A)

The current through these elements is governed by the voltage across them (Wikipedia "Solar Cell from Wikipedia, the Free Encyclopedia"):

$$V_j = V + IR_S$$

where

V_j = voltage across both diode and resistor RSH (V)

V = voltage across the output terminals (V)

I = output current (A)

R_S = series resistance (Ω)

By the Shockley diode equation, the current diverted through the diode is (Wikipedia "Solar Cell from Wikipedia, the Free Encyclopedia"):

$$I_D = I_0 \left\{ \exp \left[\frac{qV_j}{nkT} \right] - 1 \right\}$$

where

I_0 = reverse saturation current (A)

n = diode ideality factor (1 for an ideal diode)

q = elementary charge

k = Boltzmann's constant

T = absolute temperature

At 25°C, kT/q≈0.0259 volts.

By Ohm's law, the current diverted through the shunt resistor is(Wikipedia "Solar Cell from Wikipedia, the Free Encyclopedia"):

$$I_{SH} = \frac{V_j}{R_{SH}}$$

where

R_{SH} = shunt resistance (Ω)

Substituting these into the first equation gives the characteristic equation of a solar cell, which relates solar cell parameters to the output current and voltage (Wikipedia "Solar Cell from Wikipedia, the Free Encyclopedia"):

$$I = I_L - I_0 \left\{ \exp\left[\frac{q(V + IR_S)}{nkT} \right] - 1 \right\} - \frac{V + IR_S}{R_{SH}}$$

3.2.3 Open-circuit voltage and short-circuit current

At open circuit condition, I = 0 and the voltage across the output terminals is defined as the open-circuit voltage. Assuming the shunt resistance is high enough to ignore the final term of the characteristic equation, the open-circuit voltage V_{OC} is (Wikipedia "Solar Cell from Wikipedia, the Free Encyclopedia"):

$$V_{OC} \approx \frac{kT}{q} \ln\left(\frac{I_L}{I_0} + 1 \right)$$

Similarly, at short circuit condition, V = 0 and the current I through the terminals is defined as the short-circuit current. It can be shown that for a high-quality solar cell (low R_S and I_0, and high R_{SH}) the short-circuit current I_{SC} is (Wikipedia "Solar Cell from Wikipedia, the Free Encyclopedia"):

$$I_{SC} \approx I_L$$

3.2.4 Series resistance

Series resistance in a solar cell is composed of three major parts: the resistance of emitter and base of the solar cell, the contact resistance between the metal contact and the silicon and the resistance of the top and rear metal contacts. Series resistance has no effect on open-circuit voltage since the total current through the series resistance is zero (Bowden). However, near the open-circuit

voltage, the series resistance has strong effect on the IV curve and large R_S will also significantly reduce I_{SC} (Bowden). The behavior of the solar cell is similar to that of a resistor in these regimes due to the dominance of series resistance (Bowden). These effects are shown for crystalline silicon solar cells in the I-V curves displayed in the Fig. 28.

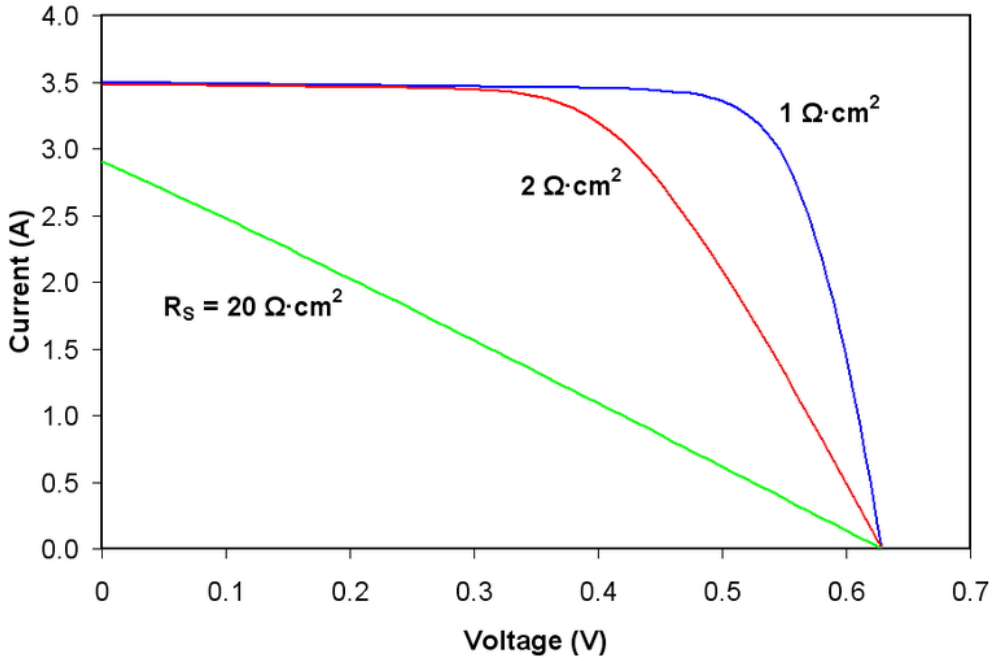

Fig. 28 Effect of series resistance on the current-voltage characteristics of a solar cell (Wikipedia "Solar Cell from Wikipedia, the Free Encyclopedia").

3.2.5 Shunt resistance

The presence of a shunt resistance, R_{SH}, mainly due to manufacturing defects, can induce significant power losses by providing an alternate current path for the light-generated current (Bowden). The effect of a shunt resistance is manifested at low light levels as the amount of current generated by light is small

(Bowden). These effects are shown for crystalline silicon solar cells in the I-V curves displayed in the Fig. 29.

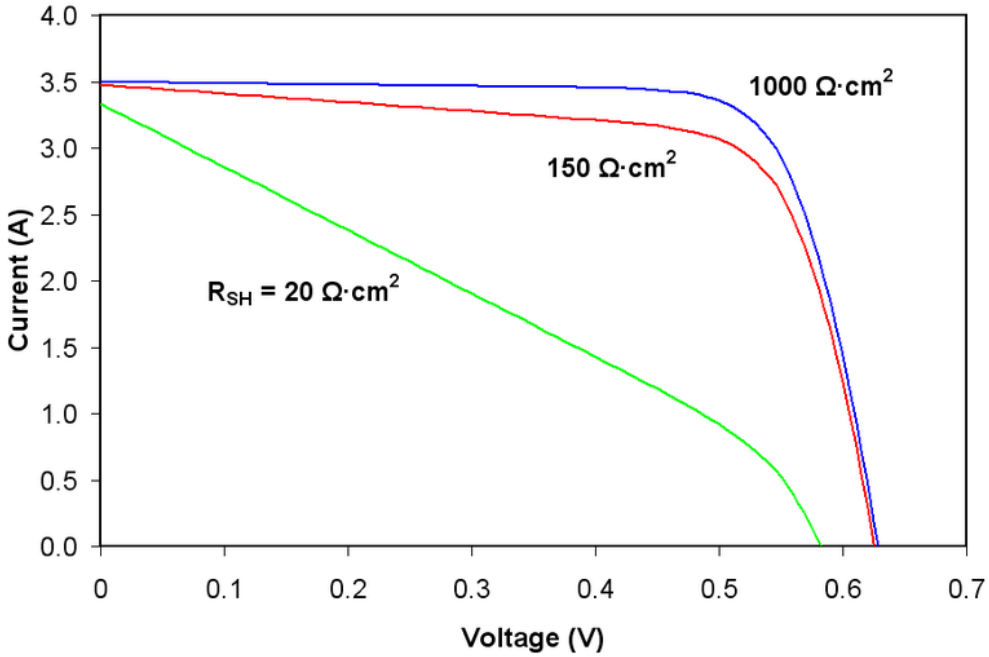

Fig. 29 Effect of shunt resistance on the current–voltage characteristics of a solar cell (Wikipedia "Solar Cell from Wikipedia, the Free Encyclopedia").

3.3 Dendritic electrode on Ge_3Se_7

3.3.1 Material characterization

The first step of this research project was to characterize the base material's optical properties through visual observation and transmission measurement to find out how well different thicknesses of solid electrolyte, with and without surface dendrites, would transmit light over a spectrum ranging from the near-ultraviolet to the near-infrared.

Ag-doped germanium selenide electrolyte was selected for initial study due to its high ion mobility and room temperature processing capability, which

results in rapid dendrite growth, excellent flexibility (which has obvious benefits in flexible device applications), and allows a larger range of substrates to be employed, including plastics. Specifically, Ge_3Se_7 was chosen as the base glass owing to its particular composition that has the largest optical gap of the germanium selenide system at approximately 2.1 eV (Popescu), though this will decline to less than 2 eV with the addition of Ag and even less with increasing Ag concentration (Orava).

Ag dendrite morphology was also studied in combination with spectrometer measurements.

3.3.1.1 Ge_3Se_7 test sample fabrication

To fabricate the test samples, a variety of thicknesses of Ge_3Se_7 base glass and Ag bilayers were first evaporated onto cleaned microscope slides in Cressington 308 deposition system, and then the Ag layer was photodissolved into the base glass to form the solid electrolyte using UV (λ = 436 nm) exposure in an Oriel aligner for 1,800 seconds at 4 mW/cm^2. In order to completely dissolve the Ag in the glass, the thickness ratio of Ge_3Se_7 to Ag was maintained at 3:1 in each case during the exposure and an adequate amount of time was used to full expose the samples to prevent Ag from remaining on the surface (although this may not have been the case in the thinnest samples, as it will be discussed later). The resulting electrolyte film thicknesses were 10, 30, 60, and 100 nm. The samples then had 60 nm thick Ag anode patterns added to facilitate dendrite growth. The schematic drawing is shown in Fig. 33.

3.3.1.2 Ag dendrite growing

The Ge_3Se_7 test device was mounted on a chuck of a probe station which has micromanipulators with probes in connection with an Agilent 4155C semiconductor parameter analyzer for testing the devices and electrodepositing Ag dendrite networks. One of the tungsten probes was connected to the anode of the test device and the other one was in contact with the Ag thin film as a cathode. 2.5 V DC was applied between the cathode and anode, to grow two-dimensional dendrite fields that were visible to the naked eye (see Fig. 34 for example). One major advantage of this kind of setup is that these regions with dendrites can also be easily targeted during the optical measurements. Different dendrite patterns were created for study purpose and the discussion is followed in the next section.

3.3.1.3 Ag dendrite morphology

A few dendrite patterns were grown on test structures to demonstrate the nature of dendrite growth. Fig. 34 (a) and Fig. 34 (b) show two different examples of dendrite growth and Fig. 34 (c) is a zoom-in image of Fig. 34 (b). In both examples, a 3 V DC bias was applied for growing dendrites but the Tungsten cathode was placed in Fig. 34 (a) twice as far away from the anode as in Fig. 34 (b). The dark taper object in the Fig. 34 (a) and Fig. 34 (b) is the tungsten probe that was used as a movable cathode during the dendrite growth. The silver anode is not visible as it is out of the field of view.

The electrodeposition of metal dendrites can have a variety of morphological features depending on the growing conditions like voltage applied per unit area, solute concentration, composition of the hosting glass, the

conductivity of the substrate, etc (Balakrishnan). It can be sorted into three categories:

1. Fractal diffusion limited aggregate (DLA)

2. Dendritic

3. Densely branched morphology (DBM)

DLA-like patterns strongly resemble the results of DLA computer model simulations (Fig. 30) and are fractal while dendritic patterns (Fig. 31) are rather straight deposits with little side branching and no well-defined radius relative to the cathode. DBM patterns (Fig. 32) are characterized by straight filaments distributed in an even radial pattern around the cathode at a specific radius and they are not fractal (West).

DLA-like patterns are fractal in nature with striking properties like optimization of transporting energy and resources (Rinaldo et al.), (Boming and Baowen), (Hui-Fen, Qing-Xin and Jian-Kang), and enhancement of localized surface plasmon resonance (Hutter and Fendler). “Fractal is a mathematical description of a complex geometric pattern exhibiting self-similarity in that small details of its structure viewed at any scale repeat elements of the overall pattern (Farlex).” There are many examples of fractals in nature, like circulatory systems of plants and mammals and river basins. One of the prominent properties in these natural fractal systems is that they often transport and distribute resources with minimal resistance and optimal size. This has led to a number of applications of employing these mechanisms in design of optimized top contact metallization (Bhakta and Bandyopadhyay), (Morega and Bejan), (A.M. Morega*). However,

as is often the case, nature resolves problems in a way that surpasses those developed by man. The dendrite patterns grown in this work are mostly DLA-like and can be potentially optimized in resistance.

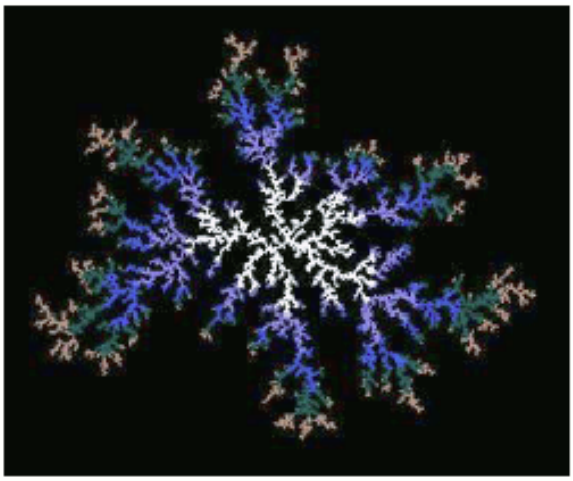

Fig. 30 Computer model of DLA growth and optical micrograph of the DLA growth patterns (Balakrishnan)

Fig. 31 Dendritic pattern (Ben-Jacob and Garik)

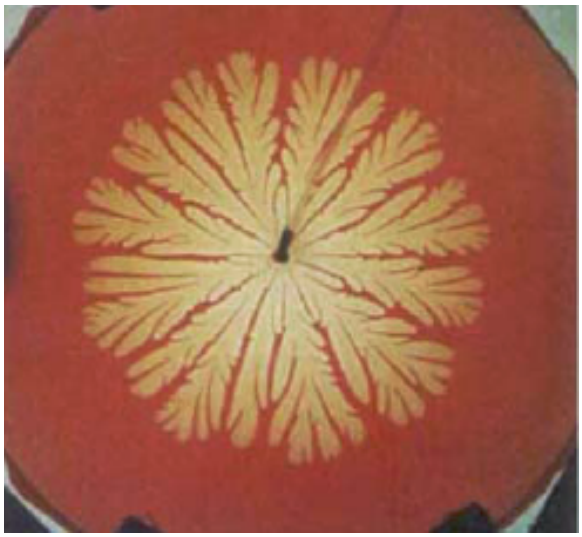

Fig. 32 DBM pattern (Ben-Jacob and Garik)

In the examples, Fig. 34 (a) illustrates a clear DLA-like dendrite growth, with narrow low-dimensional branches reaching out from the cathode tip across the surface of the electrolyte. The large gaps among the dendritic branches allow most of the light to penetrate. This dendritic network structure is fractal in nature with striking properties like optimization of transporting energy and resources (Rinaldo et al.), (Boming and Baowen), (Hui-Fen, Qing-Xin and Jian-Kang), and enhancement of localized surface plasmon resonance (Hutter and Fendler). Fractal is a mathematical description of a complex geometric pattern exhibiting self-similarity in that small details of its structure viewed at any scale repeat elements of the overall pattern (Farlex). There are many examples of fractals in nature, like circulatory systems of plants and mammals and river basins. One of the prominent properties in these natural fractal systems is that they often transport and distribute resources with minimal resistance and optimal size. This has led to a number of applications of employing these mechanisms in design of optimized

top contact metallization (Bhakta and Bandyopadhyay), (Morega and Bejan), (A.M. Morega*). However, as is often the case, nature resolves problems in a way that surpasses those developed by man.

Image Fig. 34 (b) illustrated more densely branched but less visible dendrites. Though the coverage is greater, the thinner dendrites themselves are very likely to grant the transparency. Image Fig. 34 (c) is a portion of image Fig. 34 (b) taken at higher magnification (500X) to show the dense nature of the electrodeposits. However, even at this higher magnification, the dendrites still appear to be quite transparent.

Thus, in terms of transparency of either dendrite type they both allow most of the light to penetrate and both could meet the requirements for transparent top electrode applications. In the case of dendrites in Fig. 34(a), the transparency arises because of the large gaps between the dendritic fingers whereas in dendrites Fig. 34(b), the coverage is greater but the transparency is a result of the transparency of the thin dendrites themselves. To confirm this observation, transmission measurements were performed to compare the test samples with and without dendrites in combination with material optical analysis (Ge_3Se_7) and will be introduced in the next section.

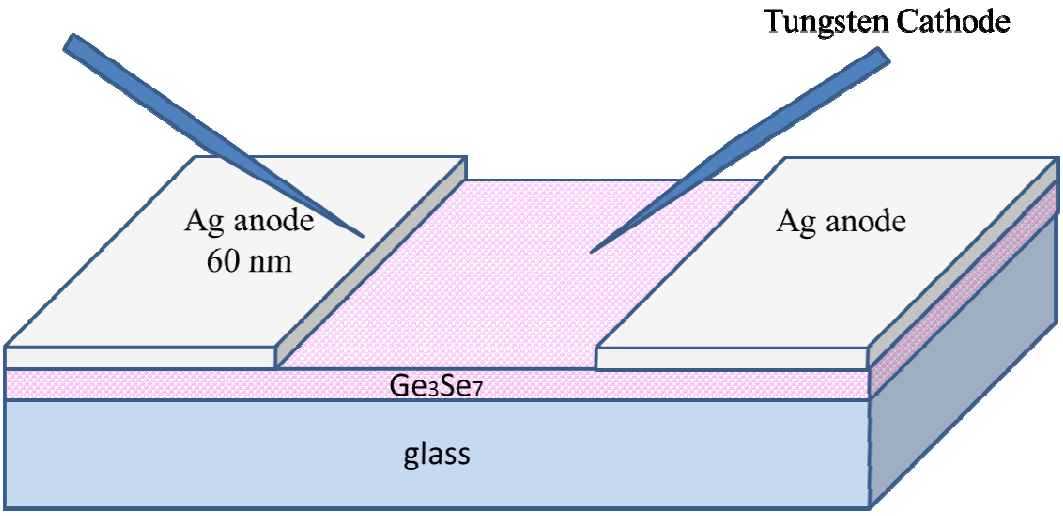

Fig. 33 Schematic drawing of Ge_3Se_7 test sample

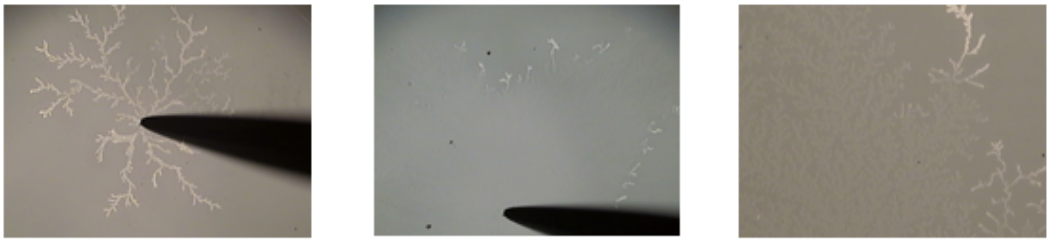

Fig. 34 Dendrite growth on a Ag-Ge-Se solid electrolyte film on an n-type layer

3.3.1.4 Optical measurements

The samples were characterized in an Ocean Optics double channel spectrometer (Model DS200) from 300 to 1100 nm to assess their transmission characteristics. A blank glass slide was analyzed first in order to subtract the contribution of the substrate from the coated sample results.

The transmission vs. wavelength plots for all samples were shown in Fig. 35 and the results summarized here. In the sub-600 nm range (corresponding to photon energy greater than 2.1 eV), transmission is relatively low and decreases with increasing film thickness. This is not surprising given that the optical gap of

the doped samples is less than 2.1 eV, resulting in a dark orange tint in the films. Above 600 nm, transmission of all samples increases with wavelength as incident photon energy drops below 2.1 eV. The spike in all the spectra around 650 nm is the equipment ranging error. The transmission spectra of the 10 nm samples show the best overall characteristics and they allow most light to penetrate for the optical range, especially above 600 nm. However, the visible spectrum typically spans from 390 nm to 750 nm and the peak intensity of sunlight is in the yellow-green (roughly 490 nm – 590 nm) region. Low transparency below 600 nm wavelength can potentially impact the performance of solar cells which are integrated with this material. Further study of electrical characterization needs to be conducted to investigate this impact in the later section.

Overall transmission characteristics in the 30, 60, and 100 nm samples with and without dendrites are very similar. If at all, the presence of dendrites seems to reduce the transmission very slightly, which is expected taking into account that dense, partially occlusive deposits were intentionally grown to aid in the characterization. This indicates that the dendritic electrode structures have little effect on transmission due to their small dimensions, which also agrees with the observation in section 3.4.1.3. However, what was not expected is the significantly higher transmission in the samples with the dendrites on the 10 nm thick films. This suggested that the samples without the dendrites were somehow less transmissive than they should be and that the dendrite growth somehow changed this situation to allow more light at all wavelengths to pass through.

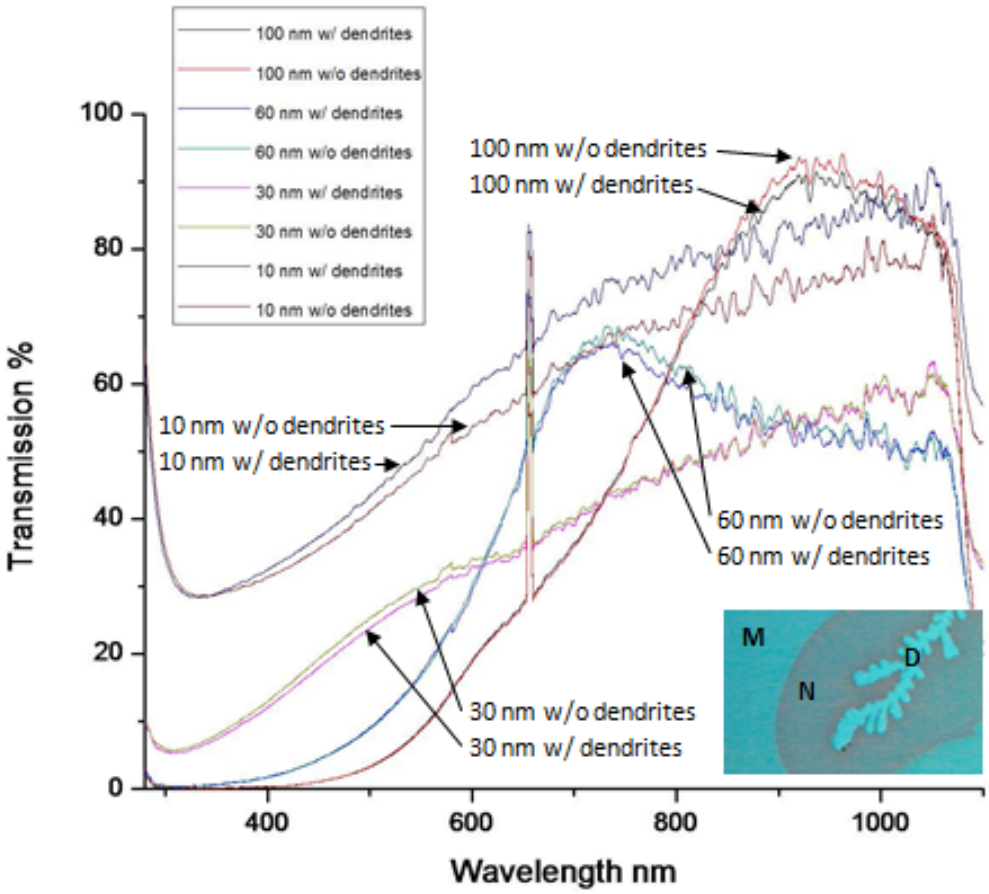

Fig. 35 Transmission vs. wavelength spectra for electrolyte samples of different thickness, with and without substantial dendrite growth. Inset: Nomarski interference contrast micrograph of a dendrite (D) grown on a 10 nm sample, showing non-metallic (N) and metallic (M) regions.

There are two possible causes for the reduction in transmission in the 10 nm samples:

1. An extremely thin (and perhaps discontinuous) layer of Ag was left on the surface following the photodissolution, leading to a higher reflectance and a lower shunt resistance even without dendrites.

2. The thinner films have a much higher Ag concentration than the thicker ones, leading to reduced transmission and a lower resistivity (note that resistivity is a strong function of Ag concentration for highly-doped films (Kawaguchi, Maruno and Elliott)).

Sheet resistance measurements were carried out to investigate this phenomenon. The results are shown in Table 1. For the thicker films, the sheet resistance typically decreased significantly following dendrite growth; for example, in the case of the 30 nm sample, it dropped from almost 10 kΩ/square to around 5 kΩ/square. To be noted, the second figure does not indicate the actual dendritic electrode resistance, as the two-dimensional electrodeposited structure was unlikely to be continuous between the randomly-positioned measurement probes. However, the lower resistance value did show that the dendrites were "shunting" the higher resistance of the film in places, leading to an overall lower sheet resistance. Considering all other factors being equal, the 10 nm films should have exhibited a sheet resistance higher than the thicker films but the results contradict the prediction. For the 10 nm films without dendrites, the sheet resistance was close to 2 kΩ/square, which, even though it was still in the range expected for highly-doped Ag-Ge-Se films (Stefan Enderling et al.), was considerably lower than the resistance of all thicker film samples. On forming the dendrites, the excess Ag from either the surface layer or from within the electrolyte itself would at least be partially consumed in the electrochemical reaction and the transmission would increase as a result, just as Fig. 35 shows. This is also supported by the film resistance measurements following dendrite

growth, which show an increased sheet resistance, in the order of 7 kΩ/square (close to the "with dendrite" values of the thicker films), suggesting that the more conducting material has indeed been consumed. Further proof of the excess Ag was obtained via optical microscopy (in conjunction with Nomarski interference contrast microscopy), which revealed that the dendrites were surrounded by regions which appeared to be less metallic than the areas away from the electrodeposits, as shown in the inset in Fig. 35.

Table 1 Sheet resistance measurements on a variety of thicknesses of Ge_3Se_7 glass slide samples with grown dendrites or without any dendrites.

Sample	Sheet Resistance (average from 5 measurements on the same sample)
10 nm Ge_3Se_7 with no dendrites	2.4 kΩ/square
10 nm Ge_3Se_7 with dendrites	7.1 kΩ/square
30 nm Ge_3Se_7 with no dendrites	9.4 kΩ/square
30 nm Ge_3Se_7 with dendrites	5.1 kΩ/square
60 nm Ge_3Se_7 with no dendrites	7.1 kΩ/square
60 nm Ge_3Se_7 with dendrites	6.0 kΩ/square

"Excess" Ag could be a result of poor deposition control for the sub-10 nm thick films. To improve the optical and electrical characteristics of the 10 nm films, dipping samples in a wet Ag etchant, like $Fe(NO)_3$ for a short period should remove any excess metallic Ag from the surface without damaging the underlying film.

3.3.2 Test solar cell with dendritic electrode on Ge_3Se_7

3.3.2.1 Test solar cell layout and fabrication

Basic solar cell test structures were fabricated by utilizing a standard solid source thermal diffusion process in the Center for Solid State Electronics Research. B-doped/p-type single crystal Si wafers (100 mm diameter, 500 µm thick, 100 orientation, 14 – 22 Ω.cm, 6.1 – 9.7 x 10^{14} cm^{-3}) were diffused with P dopant to create a 1 µm thick 10 – 14 Ω/square n-type surface layer (0.001 – 0.0014 Ω.cm, approximately 10^{20} cm^{-3}). The layer doping was somewhat higher than optimal for this substrate (cell simulation suggested that 0.9 µm thick, 0.005 Ω.cm, approximately 10^{19} cm^{-3} would have been more efficient) but absolute efficiency was not the primary concern at this stage as only the comparison of cells with and without dendrites were concerned in this experiment. The wafer backs were cleaned with HF acid, immediately followed by deposition of an Al film of 200 nm thickness to create a bottom contact to the p-type substrate. A 10 nm thick Ge_3Se_7 base glass and 3.3 nm thick Ag bilayers were deposited in the same Edwards 1 deposition system, and the Ag layer was photodissolved into the base glass to form the solid electrolyte using UV (λ = 436 nm) exposure in an Oriel aligner for 1,800 seconds at 4 mW/cm^2. At last a mylar dark field mask that was designed to form a variety of sun-side electrode layouts, shown in Fig. 36 below, was used to pattern the Ag top electrode. A 100 nm thick of Ag was deposited via thermal evaporation (Edwards 1) and thereafter a lift-off was performed to form the Ag top electrode.

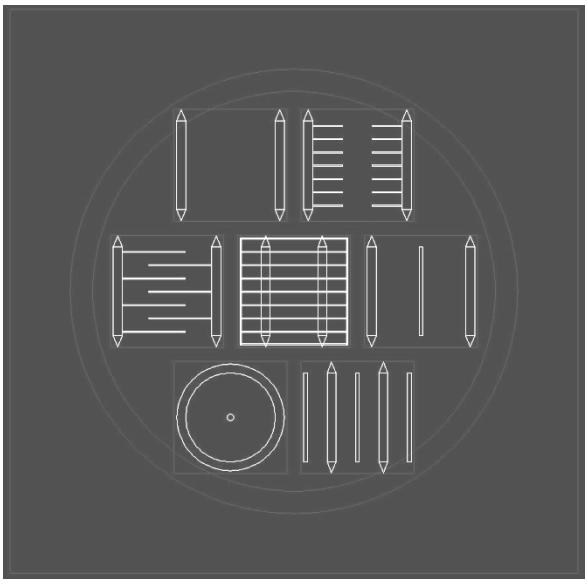

Fig. 36 Photolithographic mask used for the definition of sun-side electrode patterns. This design has seven individual electrode configurations which may be formed on a single wafer.

Seven different electrode configurations, approximately 1 inch square, was laid out and all of them could be formed on a single 100 mm wafer simultaneously to allow direct comparisons to be made. As shown in Fig. 36, the center electrode pattern was created to imitate a standard “bus bar and finger” configuration found in most solar cells. Moving clockwise from the top left, the other six configurations were as follows:

- “Open” - no electrodes between two widely-spaced bus bars.
- “Split fingers” - bus bars and fingers but with a gap in the fingers.
- “Open with sacrificial” - a sacrificial anode between two bus bars.
- “Open with multi-sacrificial” - three sacrificial anodes between and outside two bus bars.

- "Circular" – a central point electrode surrounded by a ring electrode.
- "Interdigitated fingers" - bus bars and non-bridging fingers.

3.3.2.2 Test solar cell on Ge_3Se_7 characterization

Several test cell wafers were fabricated as described above and were cut into individual 2 cm x 2 cm mini-cells with different top electrodes. Various amounts of dendrite sets were grown on these cells with different biases of 2 V to 5 V for 5 mins in an effort to bring multiple top electrodes connected. The mini-cells were illuminated with a halogen microscope lamp (21 V/150 W) which led to relatively low short circuit currents as the illuminated area was only a 5 mm diameter circle (~4×10^{-5} mm^{-2}) at most. The series resistance was determined by measuring voltages and currents at two different light intensities on the I-V curves and the formula is (Schroder):

$$r_s = |V_1-V_2|/|I_2-I_1| = \Delta V/\Delta I$$

where r_s is the series resistance, V_1, I_1, V_2, and I_2 correspond to two measurements of voltages and currents at two different light intensities. Series resistance is very important parameter and high value can seriously reduce the cell's efficiency. Turning on and off the halogen microscope lamp were used to generate two different light intensities and corresponding voltages and currents were recorded. The average open circuit voltage was 0.31 V. The results are summarized in Table 1 below. Note that the "double sets" means two separate dendrite sets grown on the sample and "triple sets" means three separate dendrite sets grown on the sample.

Short circuit current improvement ranges from around 20% to almost 200% in company with the drop of series resistances. This electrical characterization results demonstrated that the growth of dendritic structures significantly increase current collection by reducing series resistance which is an extremely important parameter in solar cells as a high series resistance will reduce the short circuit current and therefore lower the cell efficiency. However, we also noticed extensive dendrite growth can also result in decreasing short circuit current often after growing three or more sets of dendrites. Series resistance in a solar cell has three major components: first, the resistance caused by the movement of current through the emitter and base of the solar cell (so-called lateral sheet resistance); second, the contact resistance between the metal contact and the silicon; and third the resistance of the top and rear metal electrodes (Bowden). Obviously, the resistance of the rear metal electrodes is out of picture as it is not affected by the surface dendrite growth. Thus, what is concerned is how the lateral sheet resistance, contact resistance and top electrode resistance were altered during dendrite growth. Initially, only a small amount of dendrites were grown and these dendrites actually came from one of the top electrodes which was used as an anode to supply ions. The dendrites reached out to the regions where originally the resistances were high and thus reduced the lateral sheet resistance by providing more routes for current to flow, but the contact resistance between the metal contact and the silicon was not altered significantly due to the small contact area of the dendrites and so was the resistance of the top electrode as only a little amount of Ag was consumed from it. However, as they

continued to grow, they started to erode the thin narrow fingers, eventually leaving them “porous” looking (shown in Fig. 37). This erosion caused the increase of the resistances of the fingers as well as the contact resistance between the metal contact and the silicon and ultimately offset the reduction of the lateral sheet resistance. Therefore sufficient metal must be present in the electrodes in either form of sacrificial electrodes or thick top contact electrodes to supply the dendrite growth and avoid the damage to the electrodes which would cause an increase in series resistance.

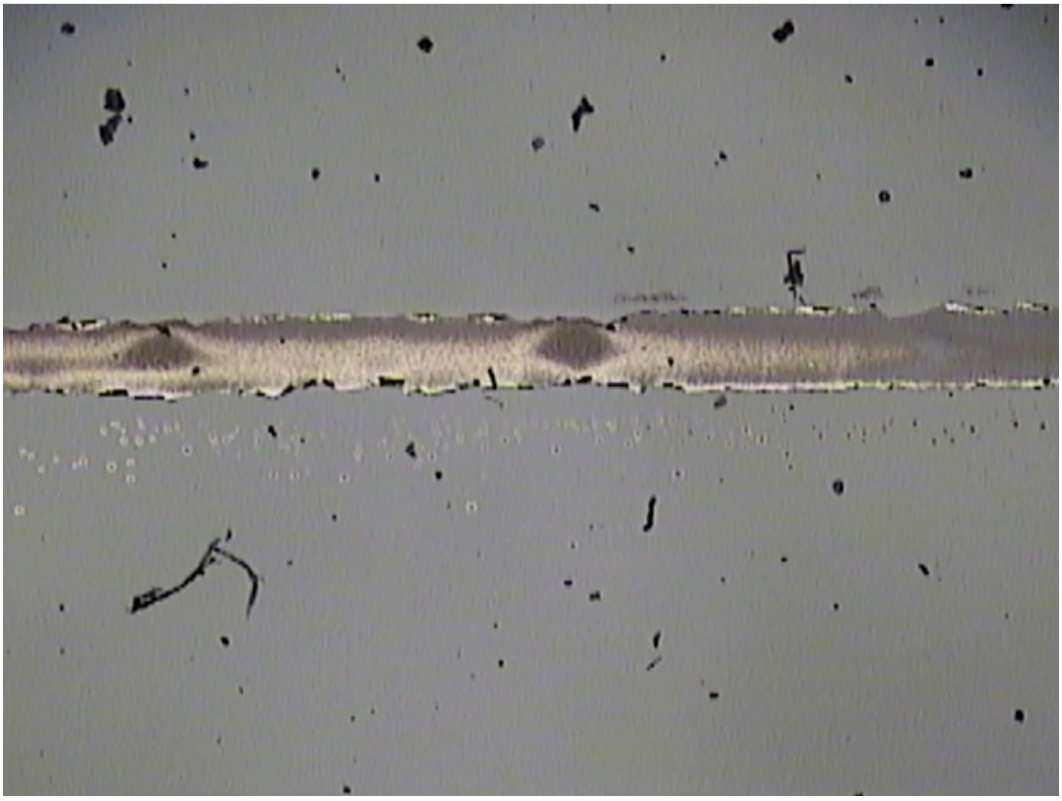

Fig. 37 An eroded finger on a solar cell sample

Table 2 Characterization data from various mini-cells illuminated with a halogen microscope lamp (see Fig. 38 for illustration of the mentioned devices) .

Configuration	V_{oc}(V)	I_{sc}(A)	ΔI_{sc}(%)	R_s(Ω)	ΔR_s(%)	Comments
OPEN w/o dendrites	0.32	0.13		1350		
OPEN w/ dendrites	0.33	0.16	+23	1110	-18	Single set
SPLIT FINGERS w/o dendrites	0.28	0.06		3450		
SPLIT FINGERS w/ dendrites	0.28	0.17	+183	633	-82	Single set
INTERDIGITATED w/o dendrites	0.31	0.18		589		
INTERDIGITATED w/ dendrites	0.31	0.22	+22	495	-16	Double sets
OPEN/SACRIFICIAL w/o dendrites	0.27	0.12		1130		
OPEN/SACRIFICIAL w/ dendrites	0.28	0.17	+42	806	-29	Triple sets
CIRCULAR w/o dendrites	0.32	0.18		707		
CIRCULAR w/ dendrites	0.33	0.24	+33	576	-19	Double sets

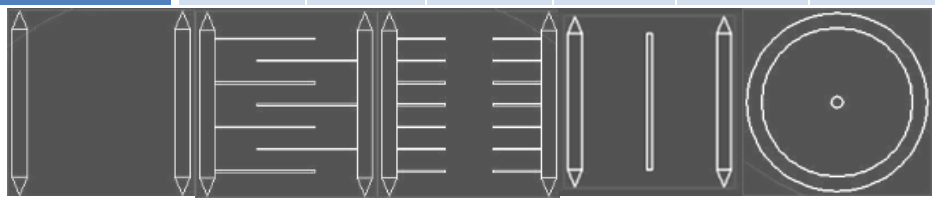

Fig. 38 (a) “Open” - no electrodes between two widely-spaced bus bars, (b) “Split fingers” - bus bars and fingers but with a gap in the fingers, (c) “Interdigitated fingers” - bus bars and non-bridging fingers.

3.3.3 Unpassivated commercial solar cell characterization

In order to evaluate the effect of the solid electrolyte films on commercial solar cells, a few 4 inch poly-crystalline silicon cells were acquired form Dr. Stuart Bowden of ASU. These cells were unpassivated, i.e., they lacked a protective layer of silicon nitride, resulting in direct access of the silicon surface, and had a screen-printed and fired Ag bus bar/finger electrode arrangement. One of them was sliced into a number of small coupons approximately 30 mm x 30 mm and one of these was completely covered by 10 nm of Ag-doped Ge_3Se_7. A two-dimensional dendrite sheet was grown between two of the fingers using a tungsten probe for the cathode and the Ag fingers for the anode, as shown in Fig. 39. The regions with and without dendrites were then illuminated with a microscope light through an objective to limit the exposed area to a few mm^2. Surprisingly, the highest short circuit currents were produced in the regions without the dendrite growth, over 10% more current than the regions with the dendrites (the difference was even larger for areas with more dendrite growth), which is opposite to the previous self-made test cell results. A possible cause is the position of the top contacts. In these commercial solar cells, the top contacts are in direct contact with Si while in the self-made test cells the top contacts are separated by a layer of Ag-doped Ge-Se from Si.

In order to have a better understanding and produce a more comprehensive comparison, three test regions were created between three sets of finger electrodes on another solar cell coupon – no coating (bare silicon), a 10 nm undoped Ge_3Se_7 coating, and a 10 nm Ag-doped Ge_3Se_7 coating, shown in Fig. 40. Dendritic

patterns were grown on the Ag-Ge-Se region and the short circuit current measured before and after growth using microscope light illumination. Similarly, the short circuit current dropped by about 10% after the dendrites had been formed on the Ag-Ge-Se region. The uncoated samples produced a slightly higher current (around 1.5% more) than the Ag-Ge-Se regions without dendrites but the most interesting result was that the regions coated with undoped Ge-Se produced a short circuit current about 1.5% higher than the uncoated regions. The experiment was repeated a couple of times to verify this effect and additional samples with two different thicknesses (30 nm and 100nm) of the undoped and Ag-doped Ge-Se, as well as uncoated regions, were also fabricated. In the 30 nm film case, the undoped film produced a 4.5% higher short circuit current, and the current in the case of the doped film, which has a lower transmission than the thinner film, was around 18% lower. In the 100 nm film case the undoped Ge_3Se_7 coated samples exhibited a 15% decrease in short circuit current compared with the uncoated cells (with little change in the open circuit voltage). See Table 3 for all the results.

From the results, it is very evident that the Ag-doped films lowered the short circuit currents compared to the uncoated cells and the cells coated with the undoped films. As it was mentioned before, with introducing the high concentration of Ag the optical band gap of the Ag-doped films will drop resulting in much less light to be transmitted through the film and the reduction in the short circuit currents. By growing Ag dendrites, even more Ag was introduced and the attenuation of light transmission becomes more dominant and therefore

offset the gain from the resistance reduction of dendrites as Si is in direct contact with top electrodes. However, in the self-made test cells, the resistance between top contacts and Si is much greater as the resistivity of Ag-doped Ge-Se is high (> 10^2 cm.Ω). The grown Ag dendrites largely reduce the resistance between top contacts and Si and overcome the attenuation of light transmission.

In the Ag-doped films, a clear trend was also observed that the short circuit currents decreased significantly with the increasing thicknesses. This can be explained by Lambert-Beer-Bouguer law, which the intensity of the transmitted light, I, is expressed by (Naser M. Ahmed*):

$$I = I_0 \exp(-\alpha d)$$

where I_0 is the intensity of the incident light, α is the absorption coefficient of the substance and d is the distance the light travels through the material. The intensity of the transmitted light is exponentially reduced while traveling through the film.

In the undoped films, the short circuit currents increased for 10 nm and 30 nm films but decreased for 100 nm film in comparison with the uncoated cells. This cannot be explained just from the optical band gap because even though they have the higher optical band gaps than the Ag-doped films the undoped films are still quite absorbing below 600 nm wavelength, which normal Si solar cells absorb very well, and supposedly reduce the short circuit currents. To understand this, it should be noted that the solar cell samples used for testing were lack of the passivation layer and anti-reflection layer that are both common for normal solar cells in use to enhance the efficiency. This suggests that the undoped Ge_3Se_7 films

act as passivation coatings and transmissive antireflective coatings. Ge_3Se_7 as a dielectric material can help passivate the surface and reduce surface defects, contributing to short circuit current increase, but more importantly it can also be used as antireflection coating. The optimal thickness for an antireflective layer is $\lambda opt/4n$, where λopt is the optimal wavelength and n the refractive index of the coating. For solar cell applications, the optimum wavelength range is 580–600 nm. Since the refractive index of the undoped Ge_3Se_7 films is around 3.0, the optimal thickness as an antireflective coating would be 50 nm, which could explain why the short circuit currents increased for 10 nm and 30 nm films but decreased for 100 nm film. The refractive index of the doped material is much higher (possibly in excess of 7.0) and even though this would lead to an ideal thickness in the order of 20 nm, the very low transmission of the doped films in the optimum wavelength range makes them unsuitable as antireflection coatings.

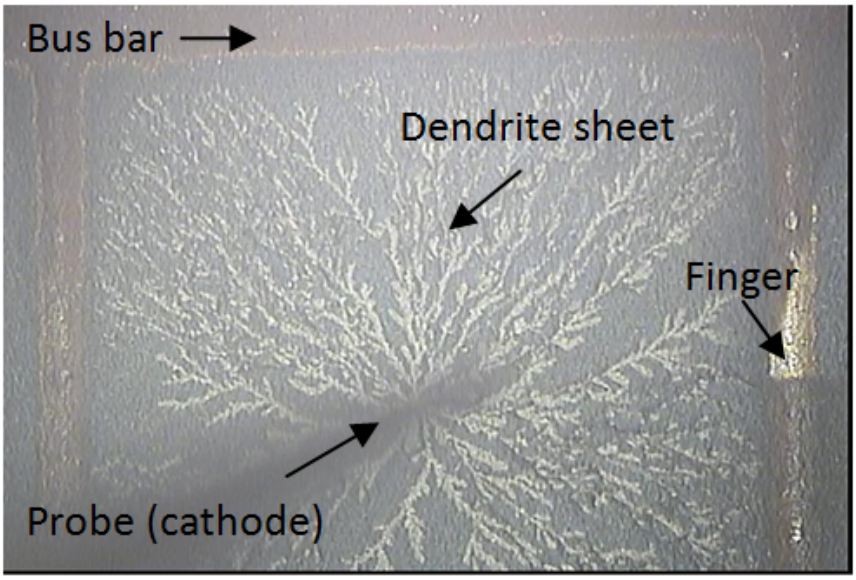

Fig. 39 Optical micrograph of dendrites grown between finger electrodes on a 10 nm thick Ag-Ge-Se film on a poly-crystalline silicon solar cell.

3.3.4 Conclusion

The undoped Ge_3Se_7 film can act as passivation coating and antireflective coating but its low ion mobility make impossible growing a great amount of dendrites. While the Ag-doped Ge_3Se_7 film can be used to grow dendritic structures which do reduce series resistance, the poor transmission and tinting associated with this material make it unsuitable. Hence, the oxide-based electrolytes, particularly Ag-doped SiO2 which is relatively transparent over the entire optical wavelength range, should be investigated.

On the other hand, Ge_3Se_7-based dendritic electrode may not be ideal for solar cell application but it can be very useful for applications which do not require high light transparency, like repairing interconnects. There is another ongoing research project, “self-healing interconnects for flexible electronics applications” (Baliga, Ren and Kozicki), which I was involved in and also utilizes Ge_3Se_7-based dendritic electrode. These interconnects show great potential in flexible electronics because they can be re-grown and continue to conduct with merely applying small voltages to heal after mechanical failure.

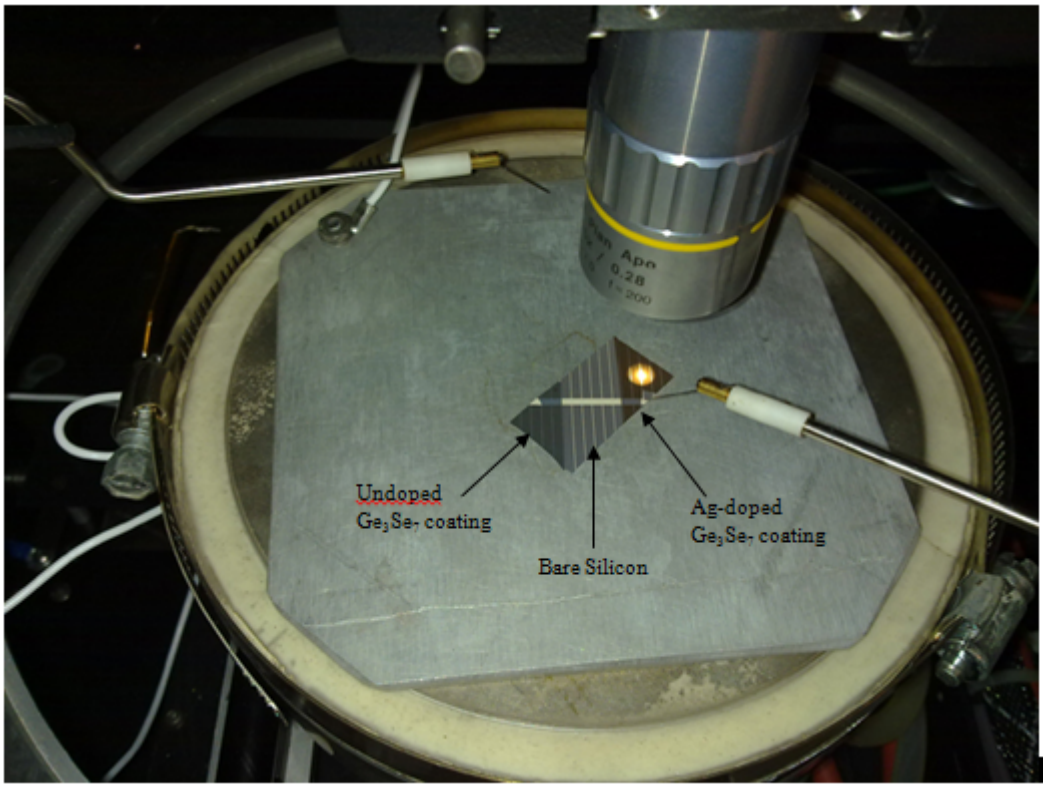

Fig. 40 Cell with 3 regions from left to right: Undoped Ge_3Se_7 coating, Bare Silicon and Ag-doped Ge_3Se_7 coating.

Table 3 Short circuit current comparison for unpassivated solar cells with 3 test regions.

Solar Cell Sample Configuration	Isc(mA)	ΔIsc(%)
w/ 10 nm Ge_3Se_7	~0.7	~1.5% higher
uncovered	~0.685	
w/ Ag doped 10 nm Ge_3Se_7	~0.675	~1.5% lower
w/ 30 nm Ge_3Se_7	~0.71	~4.5% higher
uncovered	~0.68	
w/ Ag doped 30 nm Ge_3Se_7	~0.55	~18% lower
w/ 100 nm Ge_3Se_7	~0.58	~11% lower
uncovered	~0.65	
w/ Ag doped 100 nm Ge_3Se_7	~0.26	~60% lower

3.4 Dendritic electrode on SiO_2

There are a couple of obvious advantages of using SiO_2 in place of Ge_3Se_7:

1. SiO_2 has higher light transmission over a broad range than Ge_3Se_7 (see Fig. 41).

2. SiO_2 has been widely used in solar cell devices as passivation layer, which makes no difficulty in integrating such a material.

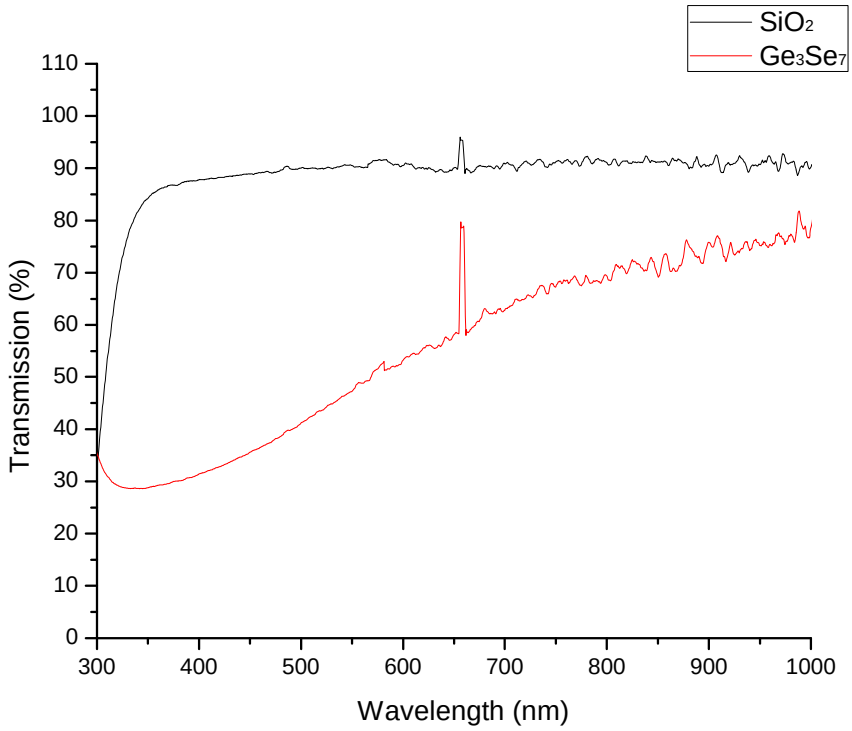

Fig. 41 Transmission of SiO_2 vs Ge_3Se_7

3.4.1 Doping SiO_2 with Ag

A piece of glass slide was first degreased using acetone, ethanol and methanol as a pre-fabrication clean step and rinsed with deionized water and blown dry in compressed nitrogen. A 15 nm thick SiO_2 film was thermally evaporated onto it, followed by depositing a 2 nm Ag thin layer. Then 60 nm thick Ag anode patterns were added via thermal evaporation to facilitate dendrite

growth. The Ag layer was exposed to UV (λ = 436 nm) source for photodissolution in an Oriel aligner for 30 mins at 4 mW/cm^2. However, no Ag diffusion was observed. No dendrite growth can be achieved even at elevated temperatures (up to 150ºC). This confirmed that photodissolution does not work for dissolving Ag in SiO_2.

In the next experiment thermal annealing was performed to dissolve Ag in SiO_2. A sample with a 15 nm thick SiO_2 film and a 2 nm Ag thin layer was annealed at 250ºC for 50 mins but again very little Ag diffused into the glass. Visible localized Ag dendrites only formed on the surface at high voltage (40 V) and 100 mA compliance. Higher annealing temperature and higher Ag density were tried in the next sample. This time a sample with a 15 nm thick SiO_2 film but a 4.5 nm Ag film, which is more than double thick than the previous sample, was prepared. It underwent the thermal annealing at 500^{0}C in N_2 for 40 minutes (note that significantly higher temperatures led to severe damage like oxidation to the Ag film). Little Ag penetration was realized due to the relatively low diffusivity of Ag in SiO_2 even at this temperature. At elevated growth temperature (up to 150^{0}C), even minimal dendrite formation required voltages in the order of 10x higher than those used in the Ag-Ge-Se system due to the low Ag concentration and poor ion mobility in the oxide. However, it was noticed that much of the Ag remained on the surface as dispersed nanoscale particles due to surface-tension-induced agglomeration in the Ag film.

To determine the effects of a denser layer of nano-particles formed by surface-tension-induced agglomeration, 16 nm thick Ag films were deposited on

15nm SiO_2 layers and annealed at 200^0C for 50 minutes. This sample was used to compare to the previous sample with a 15 nm thick SiO_2 film and a 4.5 nm Ag film annealed at 500^0C in N_2 for 40 minutes. The visible "haze" on the surface of the samples, shown in Fig. 42, confirmed that the Ag particles were larger and denser than those created from the thinner film, shown in Fig. 43.

Thermally doped oxide, although substantially more transparent than Ag-Ge-Se, is impractical for dendrite growth due to low ion concentration/mobility which leads to limited dendrite growth even at high voltages.

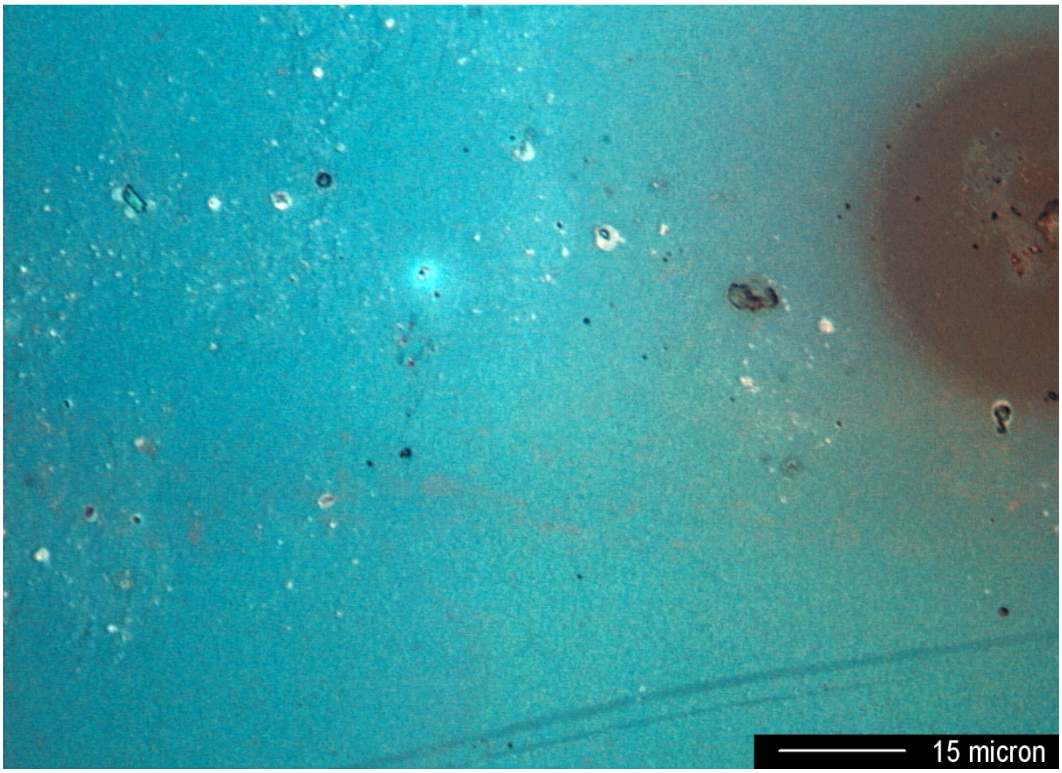

Fig. 42 4.5 nm Ag annealed on SiO_2

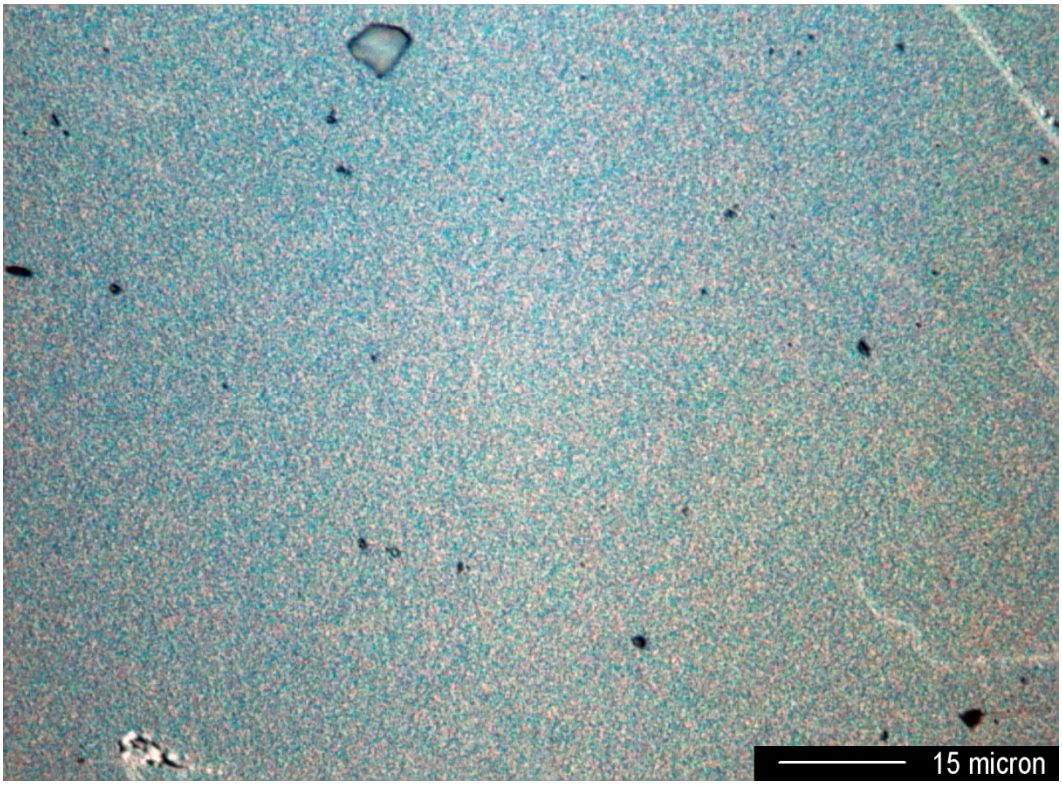

Fig. 43 16 nm Ag annealed on SiO_2

3.4.2 Water-mediated dendritic growth on SiO_2

It has been long known that silver migration can cause electrical failure in electronics resulting in insulation resistance degradation or short circuit (Yang, Wu and Christou). The Ag ions migrate from anode to cathode through the water layer on an insulating surface under the influence of a DC bias. The Ag ions are reduced at the cathode and form silver bridges between the cathode and anode electrodes. This electrochemical process is called electrochemical migration (ECM).

By introducing water or other liquid electrolyte onto SiO_2 or even Si, growing Ag metallic dendrites with low DC bias becomes possible. A glass slide sample with a 16 nm Ag film which was annealed at 200^0C for 50 minutes and

100 nm thick Ag anode patterns were deposited thermally to facilitate dendrite growth. Then the sample was mounted on the high-temp probe station and a thin surface layer of dionized (DI) water was introduced into the reaction environment. Substantial two-dimensional dendrite growth was achieved at low voltage (around 5 V).

The closer packing of the Ag particles allowed substantial two-dimensional dendrite growth on the oxide surface with or without the presence of a purified water overlayer. The growth without the water overlayer required 30 V and was fast and dense, producing high levels of coverage within 10 minutes (see Fig. 44), but the growth with the overlayer required less than 5 V to produce a similar effect (see Fig. 45). The water-mediated growth also produced dendritic clusters, in which local regions of nano-particles become connected by the dendrites.

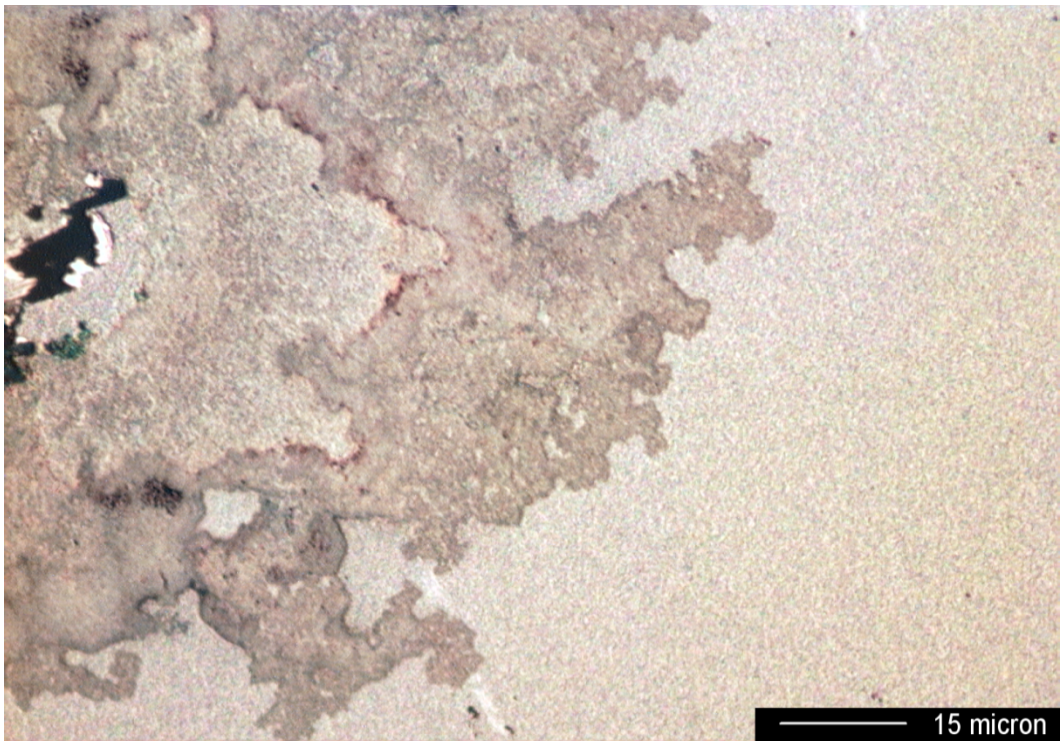

Fig. 44 Dendrite growth with assistance of Ag nanoparticles with no water present

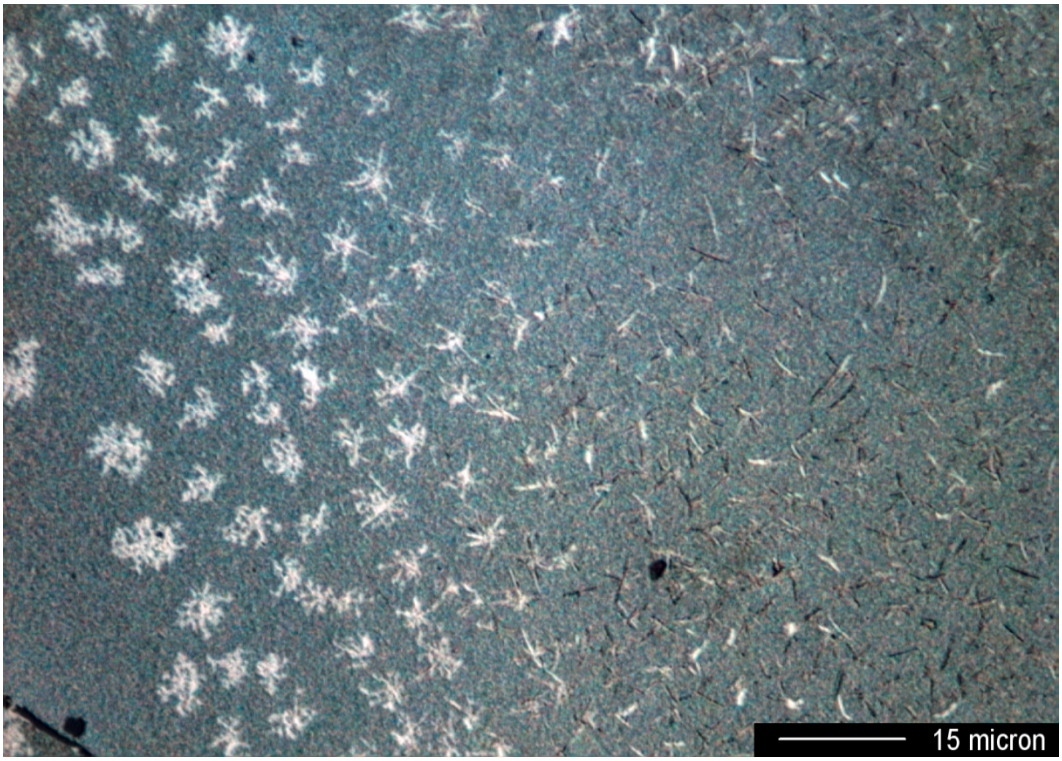

Fig. 45 Dendrite growth with assistance of Ag nanoparticles with water present

It was established that water-mediated growth could also be performed directly on SiO_2 layers without a thin layer of Ag deposited, using the electrodes as the source of Ag. In this case, substantial dendrite growth was observed for a low voltage stimulus (5 V for 10 minutes), shown in Fig. 46.

3.5 Dendritic electrode on Si solar cell

3.5.1 Water-mediated dendritic growth on Si

The water-mediated growth process was attempted on unpassivated solar cells that had screen printed Ag electrodes as the source of Ag. Substantial dendrite growth was observed with the bias up to 20 V, shown in Fig. 47. Some of the growth occurred normal to the surface into the water layer, forming 3D growth, indicating that the water is indeed the source of ions. Note that the presence of the dendrites had little impact on both open-circuit voltage and short-circuit current.

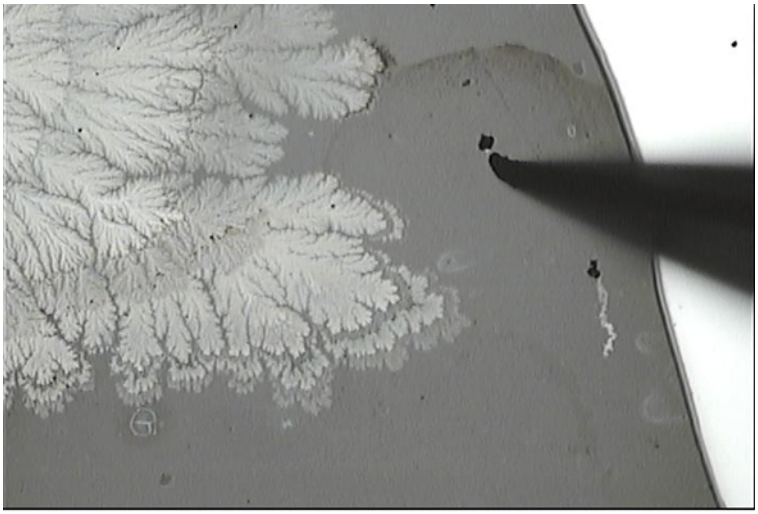

Fig. 46 Dendrite growth directly on SiO_2 without Ag nanoparticles present

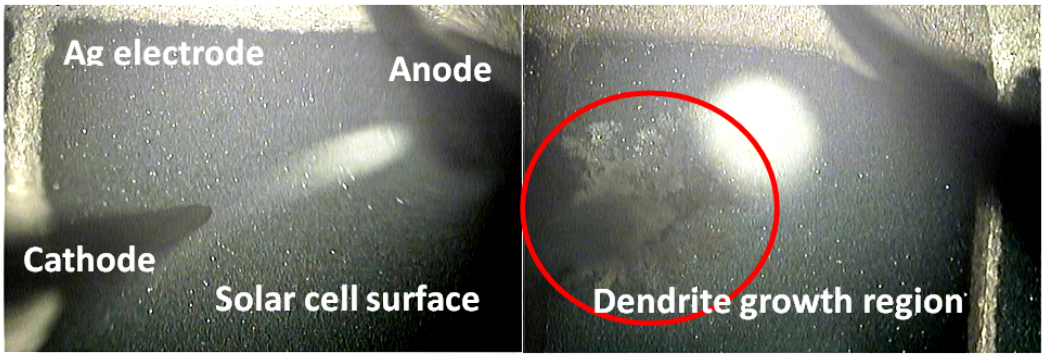

Fig. 47 Optical micrographs (before and after growth viewed through the water layer) of water-mediated dendrite growth on a solar cell. Growth was via a 20 V stimulus for 10 minutes.

3.5.2 Water-mediated growth on Si after $Fe(NO_3)_3$ etching

Ag etchant (1M $Fe(NO_3)_3$) was employed to partially remove existing printed Ag fingers on solar cells while leaving most of the busbars intact. This process reduced the short circuit current by an average of approximately 6%. Ag dendrites were then grown using the water-mediated process and a 2 V stimulus for 10 minutes and the short circuit current generally increased by an average of slightly over 3%, demonstrating that dendrites deposited via a water-mediated process, if optimized, could possibly be used to substitute for standard electrode fingers.

Water-mediated growth solves the problem of dendrite formation on oxides by supplying an alternative high mobility ion pathway. It is particularly successful on silicon substrates, including unpassivated solar cells. This may be due to the substrate acting as a distributed supplier of electrons. The previous work with semiconducting substrates showed that two-dimensional growth was

more likely to occur on such resistive materials. It is possible to replace (or repair) fine electrode features on solar cells using the water-mediated growth process, although considerable optimization is necessary. One thing that especially needs to be paid attention to is that thicker Ag films can be used to create high density nano-particle coatings following annealing at relatively low temperature and these coatings can help to promote dendrite growth with or without a water overlayer. The dendritic structures created by water-mediated growth (see Fig. 45) are extremely interesting in a scientific sense, as they suggest local connectivity with extended order that could lead to unique optical properties. In the next chapter, an investigation into this effect is presented.

4. PMC-BASED DENDRITIC PLASMONIC STRUCTURES

4.1 Introduction

In conventional bulk Si solar cells, wafer costs account for over 50% of the total PV module cost (Green). Thin film solar cell technologies offer the potential solution to considerably cut the consumption of silicon and thus lower the cost of PV. But as the absorber layers get thinner, the absorbance of near-bandgap (600-1,100 nm) light is poor so is cell performance. Surface texturing has been successfully employed in bulk Si solar cells to enhance light absorption but cannot be applied to thin film cells as simply the large texturing features, up to 10 µm in size, exceed the thin film thickness (1-2 µm) and increase minority carrier recombination in the surface and junction regions as well (Beck, Polman and Catchpole). A novel approach to achieve light trapping in thin film solar cells has emerged in utilizing the excitation of localized surface plasmons from metallic nanoparticles to enhance the thin film solar cell performance at long wavelengths.

It is believed that, by utilizing plasmonic techniques, thin film solar cells are capable of maintaining the efficiency of the thicker semiconductor while the photovoltaic layer may be thinned by as much as 100x while (Atwater and Polman).

The original idea of dendritic electrode project was to create highly transparent low resistance electrodes using the dendritic growth technique. However, something interesting was discovered during the experiments that the material system which was used for SiO_2 dendritic electrode possessed some

previously unanticipated attributes. In the previous work with oxide films, particularly, Ag nanoparticles was surprisingly created by surface-tension-induced agglomeration during annealing of thin (10 – 20 nm) layers of Ag on SiO_2. Such metallic nanoparticles can support surface plasmons - excitations of the conduction electrons at the interface between a metal and a dielectric - and it is possible to use this effect to concentrate incident light into a semiconductor below the dielectric, thereby increasing the absorption (Maier and Atwater).

Theoretical studies has suggested closely packed metal aggregates of spheres or fractal metal structures can support the existence of electromagnetic resonances over a very broad spectral range, in contrast to the (typically) narrow range associated with colloidal metallic nanoparticles (Murray and Barnes). Fractal structures have been used in applications like surface-enhanced Raman scattering enhancement (Song et al.) and fluorescence enhancement (Geddes et al.) (Drozdowicz-Tomsia, Fang and Goldys) in the past. There has been little experimental work reported to date using fractal structures for photovoltaics.

PMC technology is used to develop dendritic plasmonic structures to not only enhance but also tune the surface plasmon resonance. In this chapter, a review of plasmonics technology is presented first, followed by Ag nanoparticles characterization. Optical characterization, fabrication and results are given in the order of section 2, 3 and 4.

4.2 Review of plasmonics

People have been fascinated by the optical properties of metal particles since the time of Faraday. In the past few decades, especially after the discovery

of that Raman scattering can be enhanced by orders of magnitude through the use of metal nanostructures (Catchpole and Polman). Subsequently, lots of efforts were put into the research of fundamental properties and the development of applications of plasmonic resonances, especially in optics (Barnes, Dereux and Ebbesen) and biosensing (Anker et al.).

In 2006, Derkacs et al. reported an 8 % overall increase in conversion efficiency in thin film amorphous silicon solar cells with Au nanoparticles (Derkacs et al.). Since then, interest in using plasmonics for such thin film solar cells has intensified.

Conventionally, Si photovoltaic absorber must be 200–300 μ m thick to fully absorb the incident sunlight because Si is a relatively weak absorber. Fig. 48 shows the standard AM1.5 solar spectrum together with a graph that illustrates what fraction of the solar spectrum is absorbed on a single pass through a 2-μm-thick crystalline Si film (Atwater and Polman). Apparently, the 2-um-thick Si thin film is not thick enough and poorly absorbs the light in the 600–1,100 nm spectral range of the solar spectrum.

Plasmonic structures can enhance the absorption in thin film solar cells and make it optically thick without increasing the actual physical thickness of the photovoltaic absorber layers. Plasmons are resonant modes that the free conduction electrons in the metal collectively oscillate with interactions of light (Murray and Barnes). The oscillating electric field of the light exerts a force on the free conduction electrons in the metal (Murray and Barnes). As a result, a dipole moment is induced in the particle and leads to the redistribution of charge

which results in a restoring force on the displaced electrons associated with a resonant frequency (Murray and Barnes).

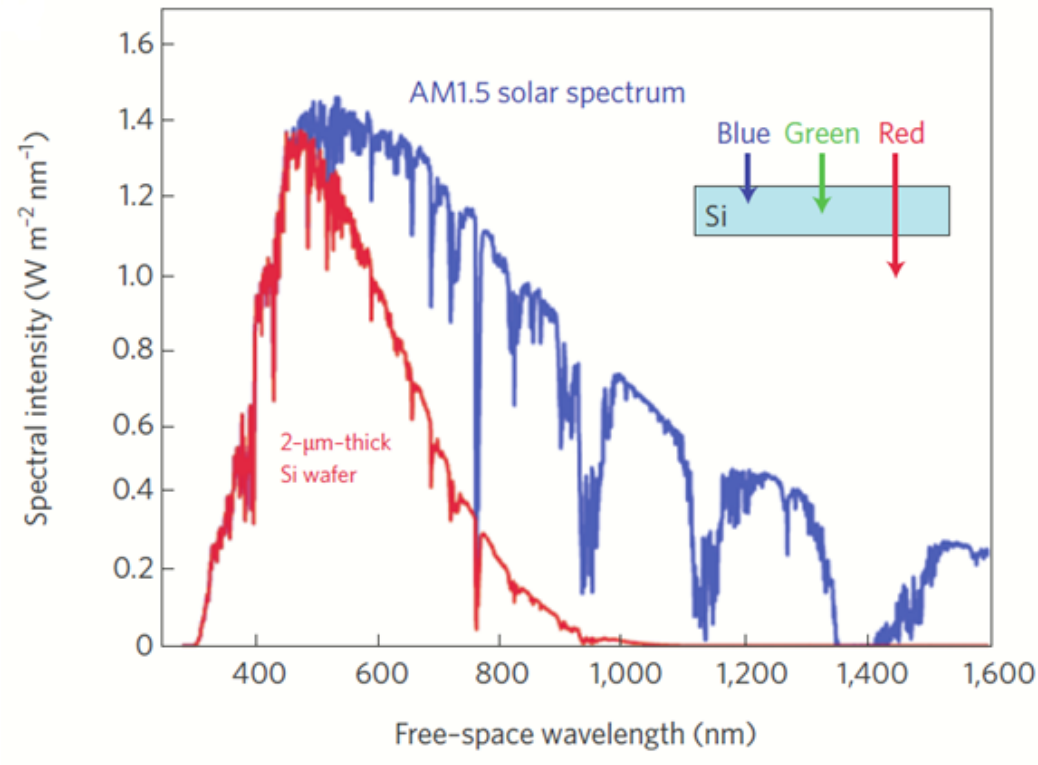

Fig. 48 AM1.5 solar spectrum, together with a graph that indicates the solar energy absorbed in a 2- μ m-thick crystalline Si film (assuming single-pass absorption and no reflection). Clearly, a large fraction of the incident light in the spectral range 600–1,100 nm is not absorbed in a thin crystalline Si solar cell (Atwater and Polman).

For particles with diameters less than the incident wavelength, a point dipole model is used to describe the absorption and scattering of light (Catchpole and Polman). The scattering and absorption cross-sections are given by (Catchpole and Polman):

$$C_{scat} = \frac{1}{6\pi}(\frac{2\pi}{\lambda})^4|\alpha|^2, C_{abs} = \frac{2\pi}{\lambda}Im[\alpha]$$

Where

$$\alpha = 3V\left[\frac{\frac{\epsilon_p}{\epsilon_m} - 1}{\frac{\epsilon_p}{\epsilon_m} + 2}\right]$$

is the polarizability of the particle. Here V is the particle volume, ε_p is the dielectric function of the particle and ε_m is the dielectric function of the embedding medium. The scattering efficiency Qsca is given by Qscat =Cscat / (Cscat+Cabs) (Catchpole and Polman). When $\varepsilon_p = -2\,\varepsilon_m$ the particle polarizability will become very large to induce the surface plasmon resonance (Catchpole and Polman). At the surface plasmon resonance the scattering or absorption cross-section can be many times the geometrical cross section of the particles (Catchpole and Polman).

There are three light trapping techniques of using plasmonic structures for thin film solar cells for allowing considerable reduction (possibly 10- to 100-fold) of the photovoltaic layer thickness without sacrificing the optical absorption and thus efficiency (Atwater and Polman). First, using metallic nanoparticles as plasmonic structures can serve as subwavelength scattering elements to excite particle plasmons to couple and trap the light into a thin absorber layer, typically an semiconductor (Fig. 49 a) (Atwater and Polman). Second, using metallic nanoparticles as plasmonic structures can be also employed as subwavelength antennas to enlarge its effective absorption cross-section by coupling the plasmonic near-field to the semiconductor (Fig. 49 b) (Atwater and Polman). Third, using a grooved metallic film as plasmonic structures on the back surface of a thin film solar cell can excite SPP (surface plasmon polaritons) modes to

boost sunlight conversion efficiency (Fig. 49 c) (Atwater and Polman). In this research work, we focused on light scattering using plasmonic metallic nanostructures and thus only the first light trapping technique mentioned above will be briefly reviewed next.

Light trapping using metallic nanoparticles can couple and trap the light into a thin absorber layer, typically an semiconductor, by scattering (Fig. 49 a) (Atwater and Polman). The light normally is scattered almost equally in both the forward and reverse directions for a small metal nanoparticle that is embedded in a homogeneous medium (Atwater and Polman). However, for a particle that is positioned close to the interface between two dielectrics, light will prefer to scatter into the dielectric with the larger permittivity (Atwater and Polman). As a result, the scattered light will experience a larger optical path length owing to the angular spread (see Fig. 49 (a)) (Atwater and Polman). For light scattered beyond the critical angle for reflection (16° for the Si/air interface), they will still be trapped in the cell (Atwater and Polman). For a cell with a reflecting metal back contact, some light reflected towards the surface will be scattered back again by the same scattering mechanism, resulting in an increase of the effective path length (Atwater and Polman).

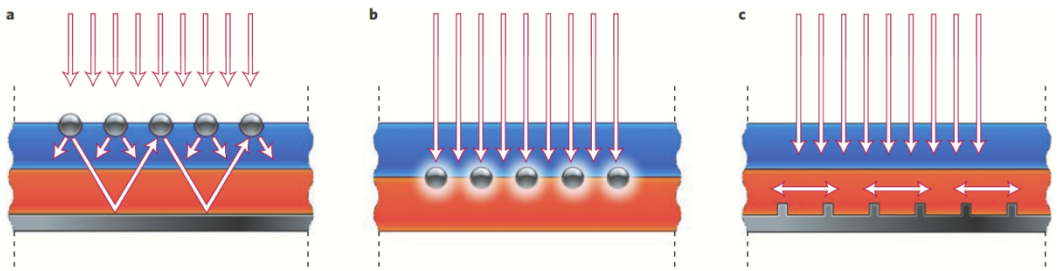

Fig. 49 Plasmonic light-trapping geometries for thin-film solar cells. a, Light trapping by scattering from metal nanoparticles at the surface of the solar cell. Light is preferentially scattered and trapped into the semiconductor thin film by multiple and high-angle scattering, causing an increase in the effective optical path length in the cell. b, Light trapping by the excitation of localized surface plasmons in metal nanoparticles embedded in the semiconductor. The excited particles' near-field causes the creation of electron–hole pairs in the semiconductor. c, Light trapping by the excitation of surface plasmon polaritons at the metal/semiconductor interface. A corrugated metal back surface couples light to surface plasmon polariton or photonic modes that propagate in the plane of the semiconductor layer (Atwater and Polman).

Light scattering not only depends on materials and their surrounding dielectric environment but also their size and their shape. For metallic particles with sizes smaller than the wavelength of light, absorption that dissipates heat dominates extinction (Pillai et al.), which can be employed in applications like solar glazing, nanoscale lithography, and therapeutic applications but not common for thin film solar cells (Pillai et al.). As the size of the particles increases, scattering exceeds absorption, which is in favor of light trapping. However, when the particle size increase over certain limits, other effects kick in like retardation

effects (the distance between the charges at opposite interfaces of the particle increases with its size, thus leading to a smaller restoring force and therefore a lowering of the resonance frequency (Maier, MyiLibrary and SpringerLink))and radiation damping (a direct radiative decay route of the coherent electron oscillation into photons (Maier, MyiLibrary and SpringerLink)), resulting in reducing the efficiency of the scattering process (Pillai et al.).

Fig. 50 shows that the enhanced near-field coupling in smaller particles, which their effective dipole moment is located closer to the semiconductor layer, can couple a greater portion of the incident light into the underlying semiconductor (Atwater and Polman).

4.3 Ring anode dendritic structure

The ring anode device structure was adopted in place of the normal coplanar device structures which were used in previous two research projects. This ring structure offers more uniform dendrite coverage than the coplanar structure as the dendrite growth is greatly influenced by electrical field and the electrical field in the coplanar structure often leads to growing more dendrites on one side over the other. Uniform dendrite coverage is particularly important for optical measurements because the spectrometer only measures an area of a few mm^2. To measure samples with non-uniform dendrite growth, interested areas must be found to obtain a more accurate result while these interested areas could well spread over the whole samples randomly and not readily visible.

In this section, Ag nanoparticles are optically characterized first, followed by fabrication of ring anode devices. Then the method of growing dendrites is presented. Results are discussed at the end of the section.

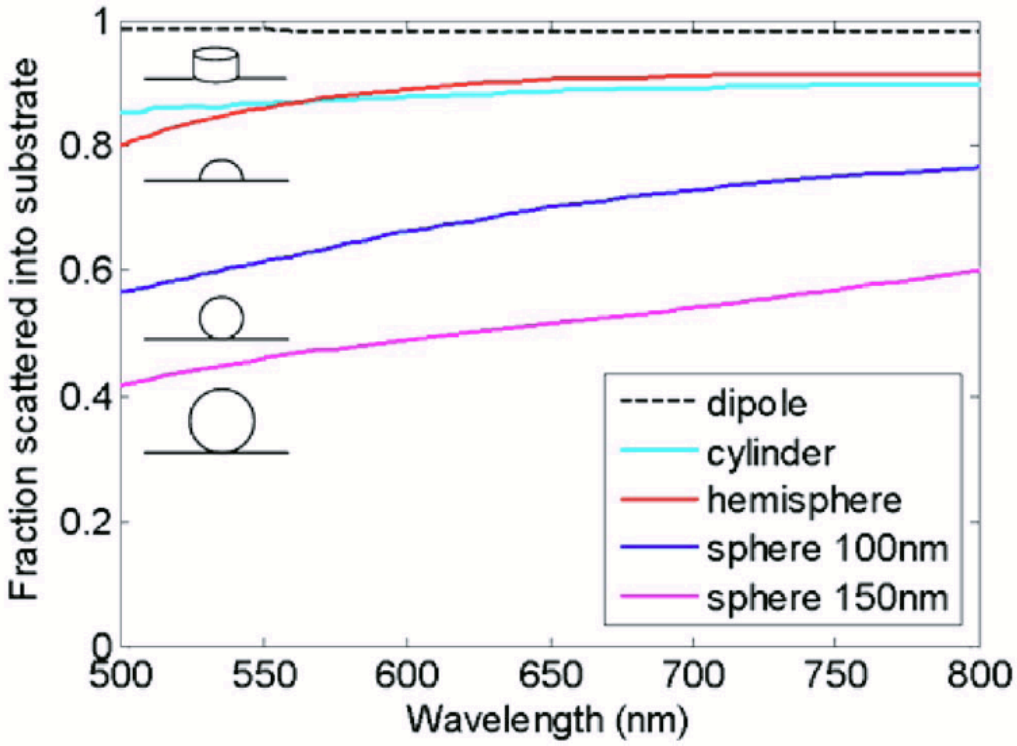

Fig. 50 (Color online) Fraction of light scattered into the substrate, f_{subs}, for Ag particles on a 10 nm thick SiO_2 underlayer on Si: a cylinder with diameter d=100 nm and height h=50 nm; a 100 nm diameter hemisphere; a 100 nm diameter sphere; and a 150 nm diameter sphere. Also plotted is f_{subs} for a parallel electric dipole that is 10 nm from a Si substrate (Atwater and Polman).

4.3.1 Ag nanoparticles characterization

Transmission measurements were used to characterize Ag nanoparticles and compare the optical changes before and after annealing. Ag was chosen due to its high scattering efficiency among metals (Stuart and Hall) and the glass

substrate was employed to simulate the dielectric environment to the nanostructures on silicon because normal silicon-based solar cell devices have an about 30 nm SiO_2 layer which is analogous to glass slides and also the underlying silicon has very limited effect on the surface plasmon resonance (Pillai et al.). To fabricate the test structure, a piece of glass slide used as substrate was first degreased using acetone, ethanol and methanol as a pre-fabrication clean step and rinsed with deionized water and blown dry in compressed nitrogen. A 16 nm thin layer of Ag film was thermally evaporated onto the glass substrate at the rate of approximately1 Å/s under high vacuum (<3*10-6 Torr). In the last process, 100 nm thick Ag anode patterns were deposited to facilitate dendrite growth. The test sample (Fig. 51) was taken to a spectrometer, Ocean Optics double channel spectrometer (Model DS200), to measure its transmission curve. Then the test sample (Fig. 52) was annealed for 50 mins at 200 °C in nitrogen and its transmission characterization was measured again. Next, large Ag dendritic patterns were grown on this sample with aqueous electrolyte and put it under spectrometer again to measure its transmission spectrum.

The measured transmission spectra were displayed in Fig. 53 and the micrographs of the samples were shown in Fig. 54. The transmission results also give the extinction (1-transmission) of the measured samples. In Fig. 53, the spectrum of the continuous thin (16 nm) Ag film on SiO2 shows no localized surface plasmon resonances but the similar transmission characteristics of bulk Ag, which is highly reflective in the visible and infrared spectrum due to bulk plasma screening. Bulk plasmas are the collective longitudinal oscillation of the

free electron gas versus the fixed ion cores (Maier, MyiLibrary and SpringerLink). The plasma frequency (bulk plasmon frequency) can be recognized as the natural oscillation frequency of the free electron gas (Maier, MyiLibrary and SpringerLink). For an incident electromagnetic waves (light) with a frequency higher than the plasma frequency, the charges are unable to respond quickly enough to screen out the incident field and the wave is transmitted; For that with a lower frequency is instead reflected (Murray and Barnes). The bulk plasmon frequency of Ag is about 3.78 eV (Pinchuk, Von Plessen and Kreibig), corresponding to a wavelength of 328 nm. In Fig. 53, the main transmission peaks around 330 nm in three different Ag spectra show the bulk plasmon position which does not obviously shift as it is the natural plasma frequency of Ag. The sharp drop in the transmission spectra of all three Ag samples at the wavelength below 320 nm is caused by the interband absorption which is around 4 eV for Ag, corresponding to a wavelength of 310 nm (Fox), and results in high absorption in the UV spectrum where low reflectivity is though expected for photo energies above 3.78 eV (Ag bulk plasmon frequency).

After annealing, the continuous thin (16 nm) Ag film on SiO_2 was converted to nanoparticles as a result of surface-tension-induced agglomeration (Atwater and Polman). A major dip in the 16 nm annealed Ag transmission plot around $\lambda = 450$ nm indicates that there exists a strong bare-island (island-on-glass) resonance, similar to that observed by other researchers under comparable conditions (see Fig. 55). The bare island resonance of the nanoparticles is the dipole localized surface plasmon resonance of the nanoparticles on a low

refractive index medium (Pillai et al.). Light incident on the particles induces movement of the conduction electrons, leading to a buildup of polarization charges on the particle surface, and results in dipole oscillations (Pillai et al.). For Ag nanoparticles with diameters great than 80 nm, a quadrupole resonance that has a different electron oscillation pattern than the primary dipole resonance occurs at a shorter wavelength than the primary transmission dip (Steven J. Oldenburg). The Ag nanoparticles' sizes used in this research are greater 100 nm (Pillai et al.) and account for the second weak dip (quadrupole resonance) at 360 nm which was also observed in other people's work (Evanoff and Chumanov) (Kim et al.) (Evanoff and Chumanov). It is known that the resonant frequency of a metal nanoparticle depends on its size, shape, material properties, and surrounding medium. Annealing metal films can alter the size and shape of metal nanoparticles. For thin films, the formed nanoparticles are well separated and close to spherical shape (Zhang) (Pillai et al.). The interparticle coupling between dispersed nanoparticles is weak and the resonant behavior resembles the single particle localized plasmon resonance in which the strong dipole resonance mode is dominant (Zhang) (Stuart and Hall). With increasing film thicknesses, the nanoparticle sizes get bigger and the spacing between nanoparticles is reduced. As a result, the interaction between nanoparticles becomes stronger and allows a coupling of resonance modes to redshift the resonance (Ghosh and Pal). Also increasing film thicknesses can cause the size and shape distributions of nanoparticles more irregular, thus resulting in broadening of localized surface plasmon resonance (Wang et al.). As the film thickness increases, the

nanoparticles tend to lose their spherical shape after annealing and look more like hemisphere, showing in Fig. 50, due to reducing coalescing forces, which is among the most efficient shapes for light trapping (Pillai et al.) (Atwater and Polman).

After annealing, an electrolytic growth over half hour at 5 V was carried out on the sample to electrodeposit a thick layer of Ag dendrites. The transmission spectrum shows a very large change of localized plasmon resonances and the resistance of the dendritic electrode formed from the nanoparticle layer in this case was measured at 25 ohm, which indicates a large amount of Ag electrodeposits. The dipole resonance peak position was difficult to determine as the resonance became so broad. The dendrites can be regarded as many closely packed Ag nanoparticles aggregates which have strong interparticle coupling and a very wide range of size and shape distributions of nanoparticles. This experiment demonstrated that the dendritic structure can be used to alter the surface optical properties of Ag nanoparticles. Tuning the surface optical properties by controlling growth of dendrites will be presented in the following sections. Fig. 54 shows a couple of examples of dispersed nanoparticles on SiO_2 layer (left optical micrograph) and the same layer following dendritic growth at 1.4 V for several minutes under ultrapure water.

It was noticed that the thicknesses of the deposited films even for the same batch of samples varied a lot as a result of poor deposition control due to the bad rotation in the deposition system and the variation could be as much as a few nm considering only sub-20nm films were deposited. Fig. 56 shows samples with 16

nm thick Ag which all was deposited at the same time in the same Edwards 1 deposition system. In the following experiments, initial transmission characteristic for each individual sample is always recorded individually, which is used for transmission comparison, as one cannot assume that films are uniformly deposited and have identical optical characteristics.

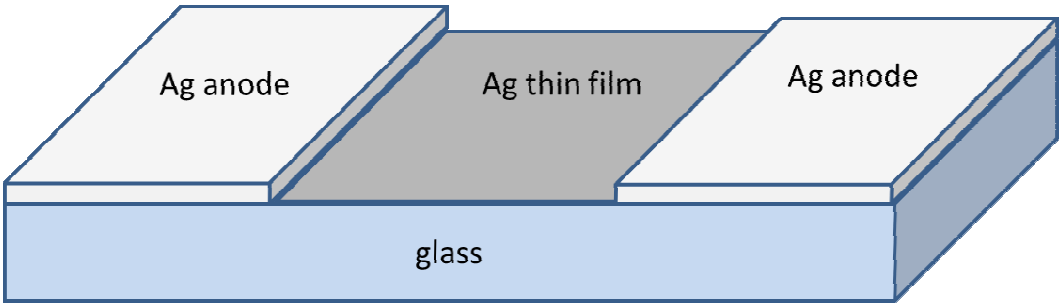

Fig. 51 Schematic drawing Coplanar Testing Device Before Annealing

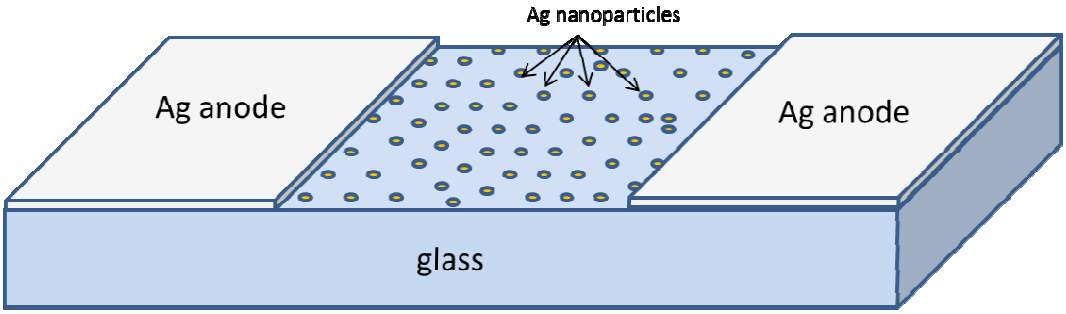

Fig. 52 Schematic drawing Coplanar Testing Device After Annealing

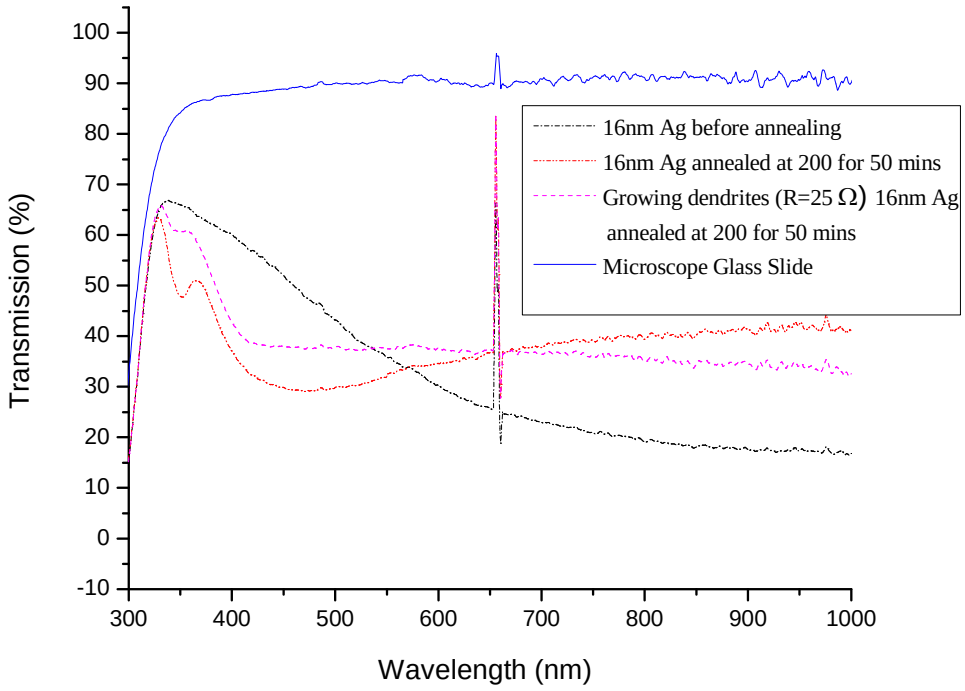

Fig. 53 Comparison of transmission characteristics of continuous 16 nm thick Ag film, annealed film/nanoparticle layer, and annealed film following dendrite growth. The resonance (dip in transmission) around 450 nm is clearly visible in the annealed film but seems to red-shift slightly following electrolytic growth. The resistance of the dendritic electrode formed from the nanoparticle layer in this case was 25 ohm. A SiO_2 transmission characteristics is also included.

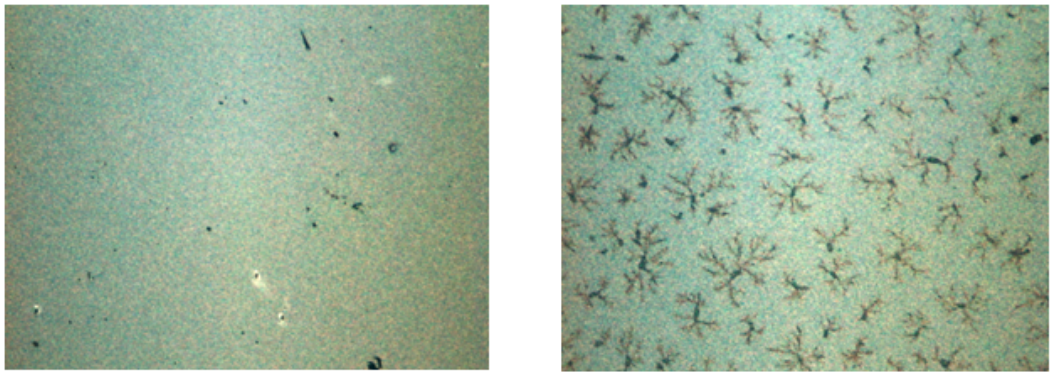

Fig. 54 Example of dispersed nanoparticles on SiO_2 layer (left optical micrograph) and the same layer following dendritic growth at 1.4 V for several minutes under ultrapure water.

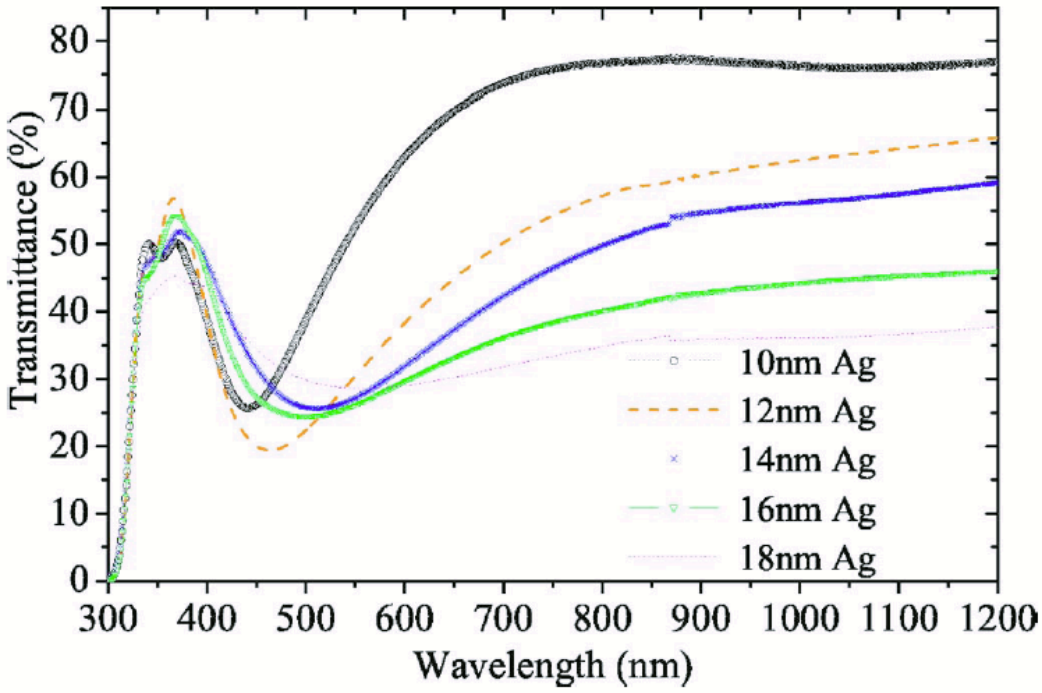

Fig. 55 Transmittance measurements showing redshifting of the bare island resonance of particles corresponding to increasing mass thickness of silver, which implies larger particle sizes (Pillai et al.).

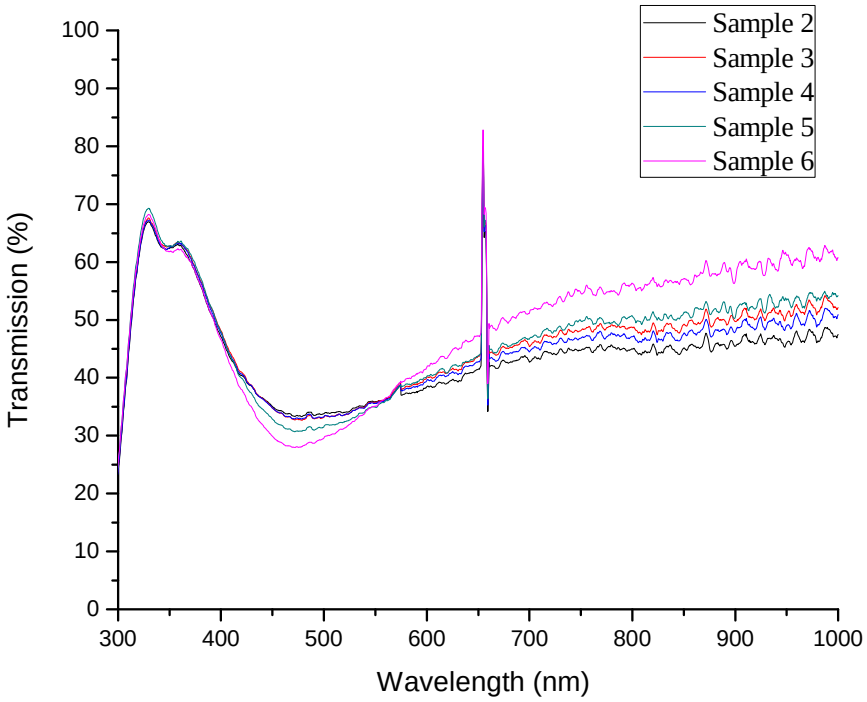

Fig. 56 Transmission characteristics of 5 samples deposited at the same time

4.3.2 Fabrication

To fabricate the test structure, a piece of glass slide used as substrate was first degreased using acetone, ethanol and methanol as a pre-fabrication clean step and rinsed with deionized water and blown dry in compressed nitrogen. A circular mask tape of 5-6 mm diameter was used to mask the substrate for the Ag ring anode of 100 nm thickness, deposited via thermal evaporation at the rate of approximately2 Å/s under high vacuum (<3*10-6 Torr). Ring shape anode is designed to provide more uniform electrical field to facilitate uniform dendritic growth than coplanar anode design. After the deposition, the mask tape was removed and the sample was treated with the same clean procedure as pre-fabrication and blown dry in nitrogen. To form the seeding layer, a 16 nm thin

layer of Ag film was thermally evaporated onto the glass substrate at the rate of approximately1 Å/s under high vacuum (<3*10-6 Torr), followed by annealing for 50 min at 200 °C in nitrogen. Due to surface-tension-induced agglomeration, Ag nanoparticles tends to grow together to form larger islands after annealing, providing nucleation sites to assist future Ag dendrite growth. The schematic drawing for the final ring anode device structure is shown in Fig. 57. After completion of test samples, initial transmission characteristics were immediately recorded for each individual sample in a spectrometer, Ocean Optics double channel spectrometer (Model DS200).

4.3.3 Dendrite growth

To form dendritic structures, the test device was mounted on a chuck of a probe station which has micromanipulators with probes in connection with an Agilent 4155C semiconductor parameter analyzer. One of the tungsten probes was connected to the anode of the test device and the other one was in contact with the Ag thin film as a cathode. A thin layer of water was disposed on the slide, directly in contact with both the anode and the cathode, and thereafter a 3 V DC bias was applied across the cathode and the anode to grow the Ag dendrite networks extending from the nanoparticles. There are two functions for these Ag nanoparticles: first, they can excite surface plasmon resonance; second, they provide nucleation sites to facilitate Ag dendrite grow (Devers et al.). Once the desired electrodeposition was completed, the test device was rinsed with DI water, blown dry. Three representative micrographs of showing tree-like dendrites and fractal aggregates from the tested samples are shown in Fig. 63, Fig. 64 and Fig.

65. Fig. 63 was taken by high-resolution microscope and Fig. 64 and Fig. 65 were taken by FESEM. Then transmission was measured to compare with the initial transmission characteristics.

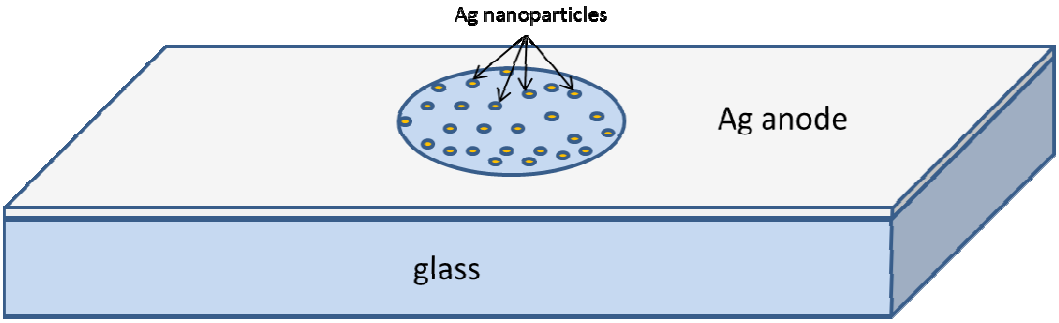

Fig. 57 Schematic drawing of ring anode test device

4.3.4 Results and discussion

Transmission results from three samples were shown below (Fig. 60, Fig. 61 and Fig. 62). During dendrite growth, all were biased with 3 V and 100 mA compliance but for different lengths of time (5 s, 20 s and 50 s). The current compliance was set high but typical growth currents were around μAs as water is a relatively weak electrolyte. Tuning the growing condition to have the desired dendritic structures is a balancing act in which several parameters must be taken into account. Different voltages were tried from 1 V to 20 V. Applied voltages that are too high lead to the 3-dimensional dendritic growth, which dendrites grow away from the surface and will not contribute to surface plasmon resonance, and hydrogen bubbles forming. Applied voltages that are too low result in slow growth as well as dense dendritic branches which reflect a great amount of incident lightg. 3 V is optimal voltage and ideal for creating fractal structures that enhance the surface plasmon resonance. Time also plays an important role for

dendritic growth. Growing for too long, dendrites will cover too much area and dendritic growth becomes electroplating, which loses the functionality and subtlety of fractal structures. Growing for too short, obviously, dendrites will have little impact on surface plasmon resonance. In Fig. 53, a spectrum of a very dense Ag dendritic network grown on top of Ag nanoparticles for a long period was presented and shows that a large amount of Ag dendrites can make the localized surface plasmon resonance very broad but the redshift can't be observed as the broadening effect almost completely buried the resonance peak location. In the results shown here, by controlling growth time and optimizing growth voltage, it is demonstrated that the localized surface plasmon resonance can be fine-tuned to enhance light scattering. In Fig. 60, the dendrites were grown for 5 s with 3 V and the main dip in the transmission plot was only redshifted very little for about 10 nm and the resonance broadening was very minimum and almost undetectable. In Fig. 61, the dendrites were grown for 20 s with 3 V and the main dip in the transmission plot was redshifted for almost 50 nm but the resonance broadening was still very small. In Fig. 62, the dendrites were grown for 50 s with 3 V and the main dip in the transmission plot was redshifted for about 60 nm. The resonance was significantly broadened compared to 5s and 20 s growths. To better understand these results, we must first understand how dendrite networks alter the localized surface plasmons which are generated by nanoparticles.

These Ag dendrite networks are natural large fractal aggregates. The fractal dimension is calculated for a typical grown fractal dendritic structure using the box counting technique to confirm the fractal nature of these dendritic

structures. An example of the dendrite growth used for box-counting is shown in Fig. 58 and the counting result is given in Fig. 59. The fractal dimension is Df = 1.8746 +/- 0.17051, which is in line with the fractal dimension 1.7 of typical DLA-like structures (West). Fractal structures do not possess translational invariance, and ordinary running waves cannot be transmitted (Shalaev et al.). Localized surface plasmon resonances associated with different features of fractal structures strongly couple with each other via dipolar or, more commonly, multipolar forces and leads to a redistribution of the plasmon amplitude from a large number of particles into much larger amplitude on a few localized particles (Shalaev et al.) (Qiu et al.). Therefore, plasmon resonances on fractal structures are not independent localized surface plasmons and they should be treated as collective eigenmodes which are formed by the interaction between different features of fractal structures (Shalaev et al.). Our results shown in Fig. 60, Fig. 61 and Fig. 62 demonstrated that the coupled plasmon resonances of Ag fractal dendrite networks grown on top of Ag nanoparticles with controlled dendrite growing parameters can be redshifted and extended to long wavelengths, and cover a broad spectral range with strong amplitude in comparison to the particle plasmon resonance (Qiu et al.).

The most prominent effects, which can enhance localized surface plasmon resonances and benefit thin film solar cells, observed on the bare island resonance due to the growth of dendritic structures in Fig. 62 can be summarized as 1. resonance redshift, 2. resonance broadening and 3. large amplitude of resonance.

1. The bare island resonance peak red-shifted to longer wavelengths. The electrodeposition of dendritic Ag structures (see Fig. 64 and Fig. 65) lead to a broader distribution of particle sizes than annealed nanoparticles and result in many originally separated particles making contact with each other. In dispersed nanoparticles, redshift occurs because the distance between the charges at opposite interfaces of the particle increases with its size and conduction electrons across the particle no longer move in phase. This leads to a reduction in the depolarization field (which is generated by the surrounding polarized matter) at the center of the particle (Catchpole and Polman) As a result, the restoring force becomes smaller and therefore the resonance frequency lowers (Maier, MyiLibrary and SpringerLink) and shifts to longer wavelengths. After the electrodeposition of dendritic Ag structures, not only the sizes of originally separated particles increased but also the interactions between particles increased as there always exists a strong coupling of a particle with neighboring particles in fractals (Shalaev). The positive metal cations in the neighboring particles exert additional coulombic attractions and weaken the restoring force of the electron oscillation (Zhu et al.). As a result, the plasmon energy is reduced and consequently the plasmon wavelength is redshifted to longer wavelengths. This is particularly important for thin film solar cells as they absorb weakly in visible and longer wavelengths and the redshifted resonance can enhance the absorption in that spectral range.

2. The bare island resonance broadens, which allows light trapping occur over a broad range of wavelengths. In dispersed nanoparticles, this resonance

broadening effect mainly results from the weakening of the strength of the dipole plasmon resonance (Maier, MyiLibrary and SpringerLink). As the particle volume increases, radiation damping also increases. In radiation damping, vibrating energy of moving charges, such as electrons, is converted to electromagnetic energy and is dissipated in the form of radio waves or infrared or visible light (Encyclopædia Britannica. Encyclopædia Britannica Online. Encyclopædia Britannica). After the electrodeposition of dendritic Ag structures, many annealed nanoparticles experienced size increase as well as large size variation, which caused the resonance broadening, but more importantly the interactions of the coupled adjacent nanoparticles with large size variation created a variety of resonant modes over a wide spectral range (Shalaev et al.) (Murray and Barnes). In fractal structures, the resonance frequency of the localized surface plasmon mode is dependent on the local configuration of particles at the mode location (Podolskiy and Shalaev). A random fractal comprises a large number of local geometries due to the presence of the inhomogeneous distribution of particle sizes and spacings and thus the interactions in a particle with neighboring nanoparticles are also inhomogeneous over the particle volume (Podolskiy and Shalaev) (Murray and Barnes). As a result, higher order resonant modes, other than the dipole mode, can be excited. Different fractal structures possess different plasmon resonance frequencies and consequently a collection of these resonance frequencies spans over a broad spectral range covering the visible and infrared (Podolskiy and Shalaev) (Qiu et al.). Broadening the resonance at longer

wavelengths is considered to be an advantage for solar cell applications as the enhancement over visible and longer wavelengths are desired.

3. The bare island resonance amplitude increased, which indicates the excitation of a strong resonance due to the fractal dendrite structures. This effect was predicted in (Shalaev), the enhancement at longer wavelength due to aggregation of initially isolated particles into fractal structures is proportional to $(R/r)^{3(2-Df)}$ (enhancement factor in 2 dimensions), where R is the radius of a large fractal cluster, r is the radius of small metal particles and Df is the fractal dimension. The fractal dimension calculated for a typical fractal dendritic structure in section 4.3.4 is Df = 1.8746 +/- 0.17051, which is in line with the fractal dimension 1.7 of typical DLA-like structures (West). Clearly, there is always an enhancement as the enhancement factor is always bigger than 1 for Df<2 and R is always larger than r for a large fractal structure.

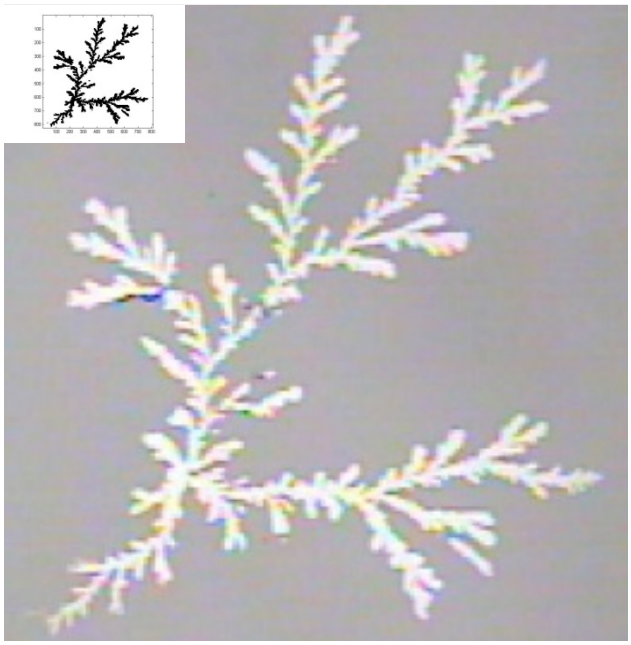

Fig. 58 An example of the dendrite growth used for box-counting

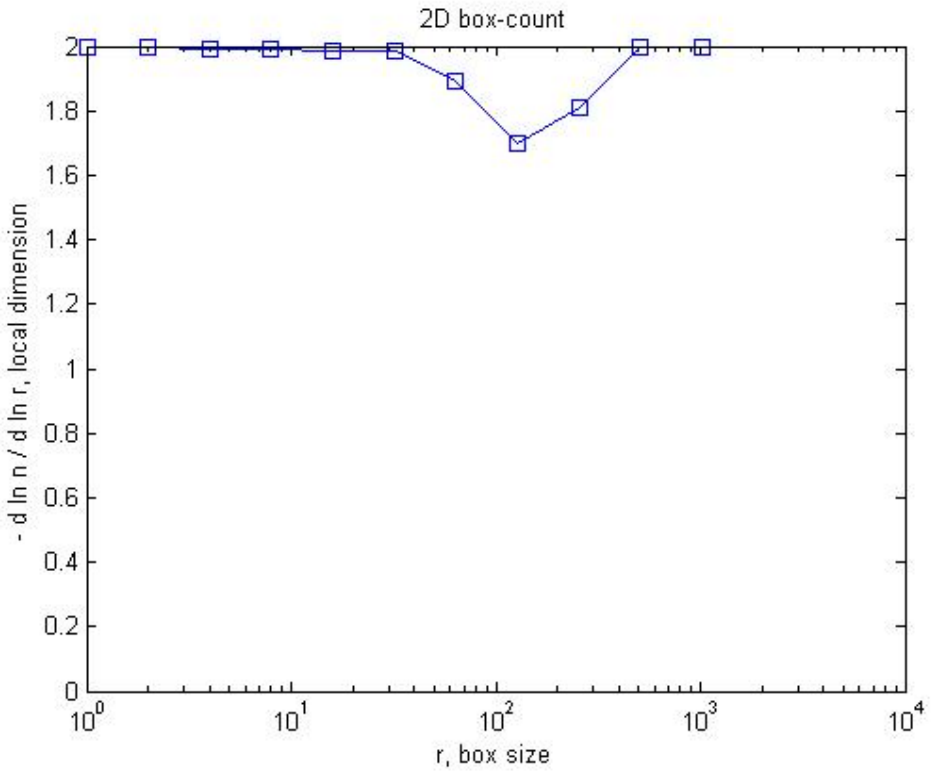

Fig. 59 Box-counting result of the example shown in Fig. 58

4.3.5 Conclusion

In this research project, metallic dendritic plasmonic structures is demonstrated and it can potentially be utilized to excite strong surface plasmon resonance and enhance thin film solar cells performance at longer wavelengths by electrochemically growing fractal structures with assistance of surface metal nanoparticles.

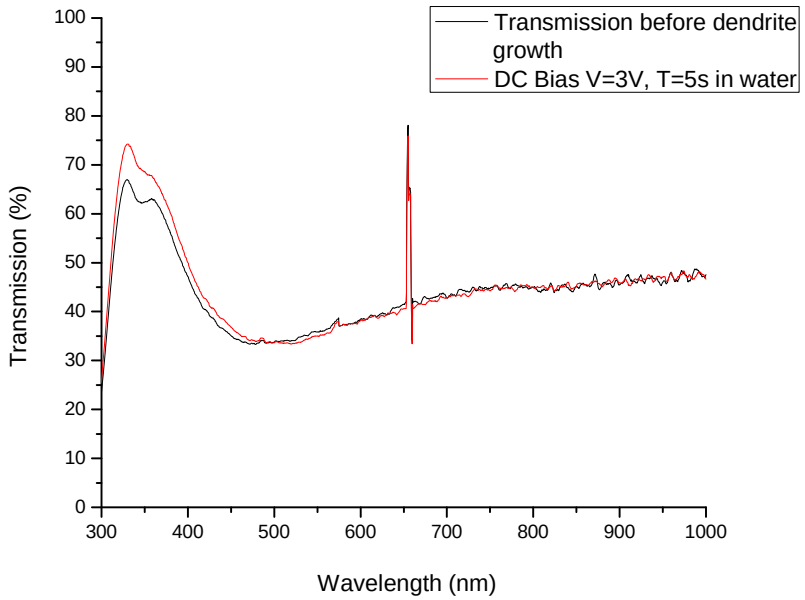

Fig. 60 Transmission characterisitcs of a sample with dendrite growth at 3 V for 5 s

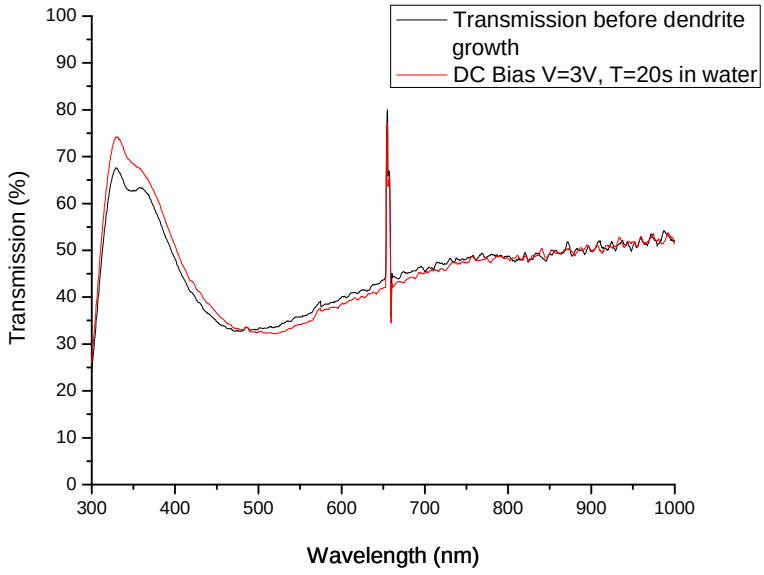

Fig. 61 Transmission characterisitcs of a sample with dendrite growth at 3 V for 20 s

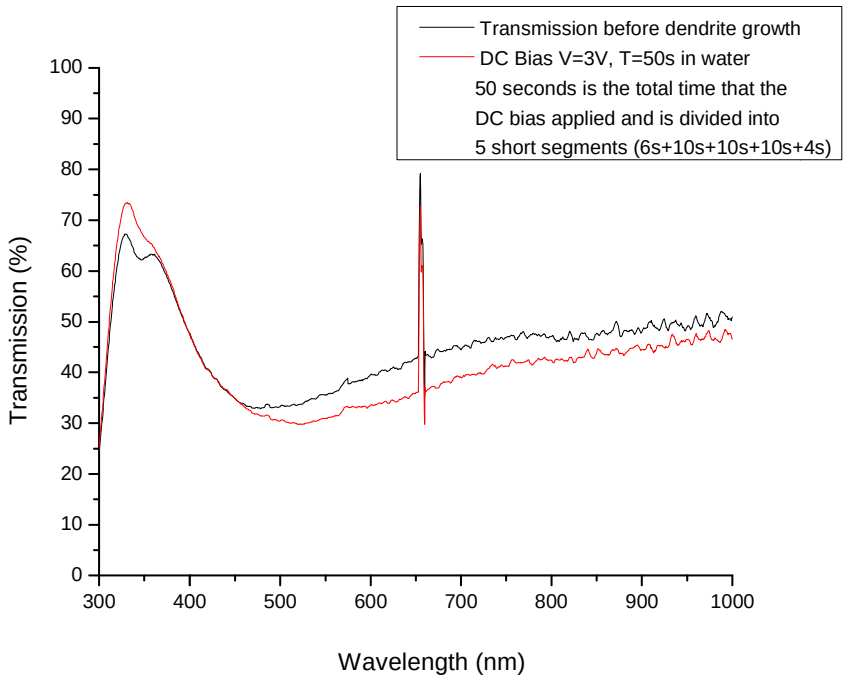

Fig. 62 Transmission characterisitcs of a sample with dendrite growth at 3 V for 50 s including 5 continuous short segments of growth

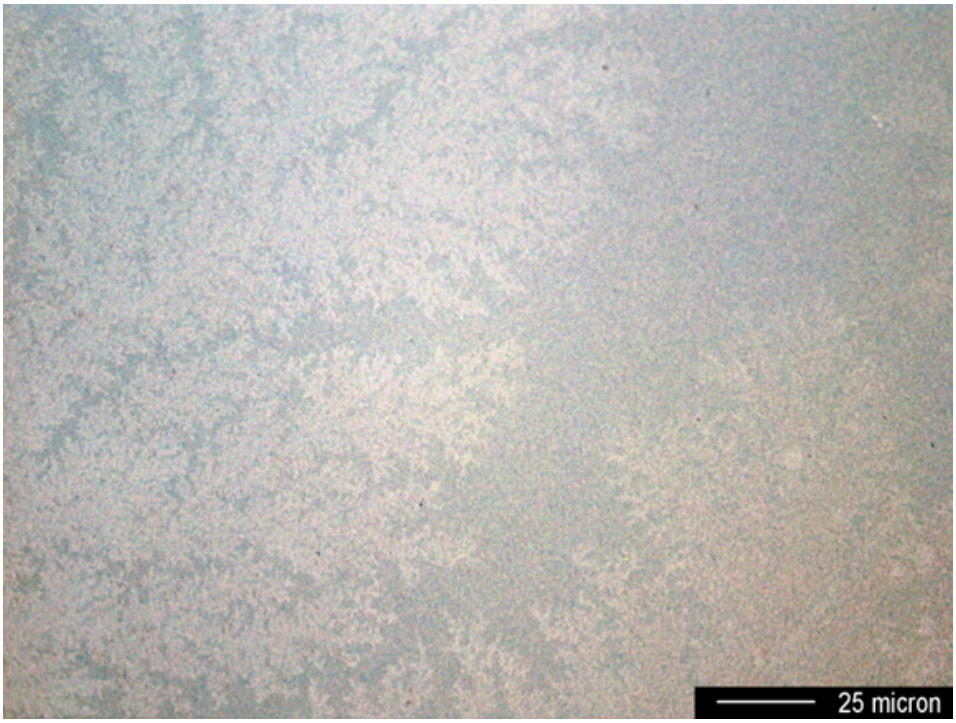

Fig. 63 Dendrite growth micrograph from high-resolution microscope

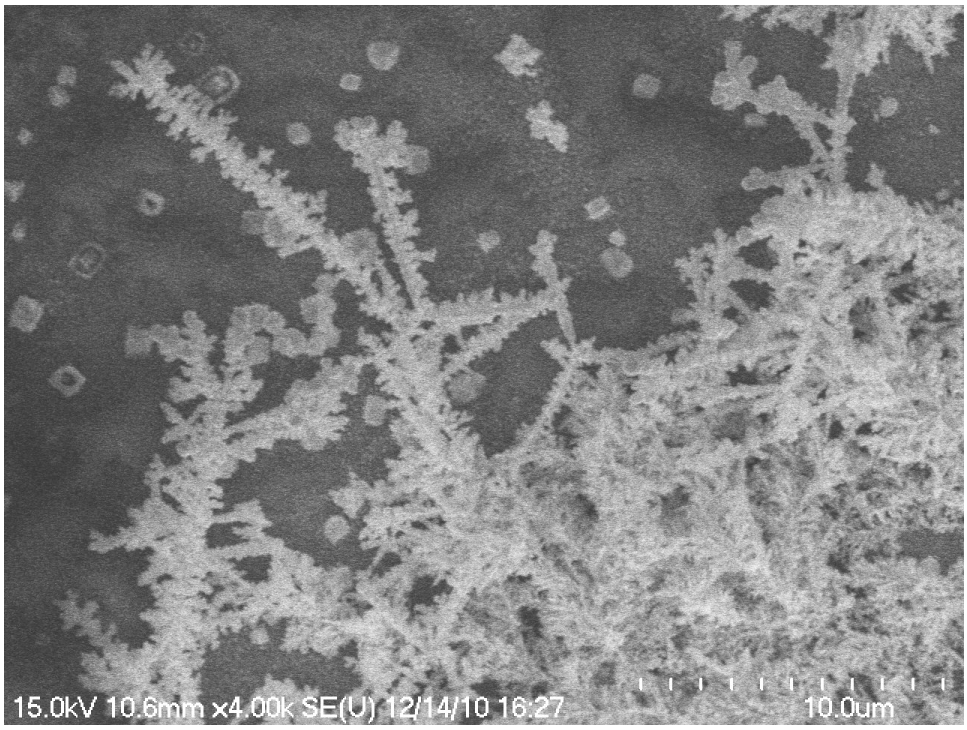

Fig. 64 Tree-like dendrite growth micrograph from FESEM

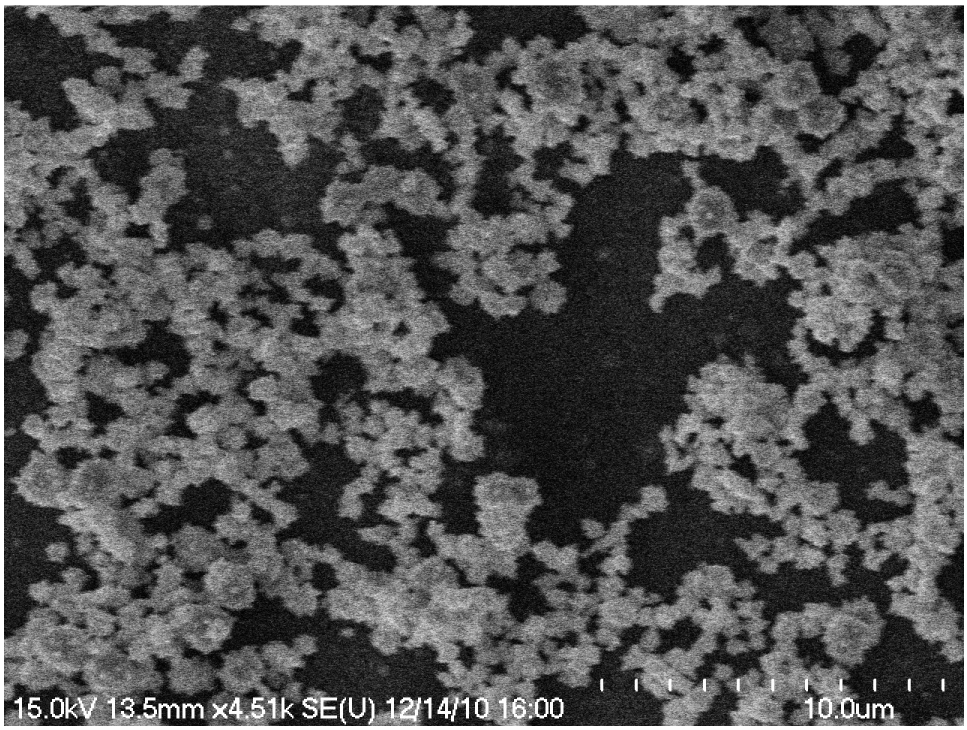

Fig. 65 Fractal Ag particles aggregates micrograph from FESEM

5. CONCLUSION

In this dissertation, three PMC-based lateral devices are presented.

A novel PMC-based lateral microwave switch was developed and characterized for use in microwave systems. The device utilizes a switching mechanism based on PMC technology, in which mobile ions within a solid electrolyte undergo an electrochemical process to form and remove a conductive metallic "bridge" to define the change of state. The PMC-based switch has demonstrated an insertion loss of ~0.5dB, isolation of >30dB, low voltage operation (1V), low power (~ μ W) and low energy (~μJ) consumption, and excellent linearity up to 6 GHz. The switch requires fewer bias operations (due to non-volatile nature) and has a simple planar geometry allowing for novel device structures and easy integration into microwave power distribution circuits.

PMC technology is used to develop lateral dendritic metal electrodes. Originally GeSe was choose due to its high ion mobility and room temperature processing capability, excellent flexibility, and allows a larger range of substrates to be employed, including plastics. Although dendritic metal electrodes grown in GeSe prove to reduce series resistance, the relatively poor transmission and tinting associated with the Ag-Ge-Se electrolytes may not be ideal for solar cell applications. However, there are plenty other applications which do not require high light transparency but need resistance reduction, for example, self-healing interconnects in which dendritic metal electrodes were grown in Ag-Ge-Se electrolytes for repairing broken interconnects. SiO_2 as another solid electrolyte, which is highly transparent in visible light spectrum and compatible with

photovoltaic industries as it has been used as surface passivation layer for long time, was also investigated. But due to its low ion mobility material growing dendrites within it proves to be very difficult. A simple water-mediated dendrite growth method was therefore developed to overcome solid electrolyte material issues and turns out to be very successful. Note, other liquid electrolytes can also be used. Metallic dendritic electrodes hence can be grown on either insulators like SiO_2 or semiconductors like Si. These dendritic electrodes have attributes like low resistances and relatively high light transmission and can be potentially used for solar cell applications, like replacing conventional Ag screen-printed top electrodes. This research effort also laid a solid foundation for developing dendritic plasmonic structures.

In recent years, plasmonics for photovoltaics has taken off as it plays an important role in enhancing the light trapping properties of thin-film solar cells for boosting efficiency and reducing costs. The metallic dendritic plasmonic structures were developed by growing metallic dendritic networks electrochemically on SiO_2 with a thin layer of surface metal nanoparticles in water electrolyte. These structures increase the distribution of particle sizes by connecting pre-deposited Ag nanoparticles into fractal structures and result in three significant effects, resonance red-shift, resonance broadening and resonance enhancement, on surface plasmon resonance for light trapping simultaneously, which can potentially enhance thin film solar cells' performance at longer wavelengths.

REFERENCES

A.M. Morega*, J.C. Ordonez**, P.A. Negoias*, M. Morega*, and R. Hovsapian**. "Optimal Electrical Design of Spherical Photovoltaic Cells." 15 Nov., 2010 <cds.comsol.com/access/dl/papers/1668/Morega.pdf >.

Andoh, Yoshiyasu. "Market & Technology of Rf Modules: Focusing on Front End Modules for Cellular Terminals." *Yoshiyasu Andoh*. Ed. Print.

Anker, J. N., et al. "Biosensing with Plasmonic Nanosensors." *Nature Materials* 7.Copyright 2008, The Institution of Engineering and Technology (2008): 442-53. Print.

Atwater, Harry A., and Albert Polman. "Plasmonics for Improved Photovoltaic Devices." *Nature Materials* 9.Compendex (2010): 205-13. Print.

Balakrishnan, Muralikrishnan. "Germanium Sulfide-Based Solid Electrolytes for Non-Volatile Memory." 3241249. Arizona State University, 2006. Print.

Baliga, Sunil R., Minghan Ren, and Michael N. Kozicki. "Self-Healing Interconnects for Flexible Electronics Applications." *Thin Solid Films* 519.Compendex (2011): 2339-43. Print.

Barnes, William L., Alain Dereux, and Thomas W. Ebbesen. "Surface Plasmon Subwavelength Optics." *Nature* 424.Compendex (2003): 824-30. Print.

Beck, F. J., A. Polman, and K. R. Catchpole. "Tunable Light Trapping for Solar Cells Using Localized Surface Plasmons." *Journal of Applied Physics* 105.11 (2009). Print.

Ben-Jacob, E., and P. Garik. "The Formation of Patterns in Non-Equilibrium Growth." *Nature* 343.Copyright 1990, IEE (1990): 523-30. Print.

Bhakta, Aditya, and Santanu Bandyopadhyay. "Constructal Optimization of Top Contact Metallization of a Photovoltaic Solar Cell." *International Journal of Thermodynamics* 8.Compendex (2005): 175-81. Print.

Boming, Yu, and Li Baowen. "Fractal-Like Tree Networks Reducing the Thermal Conductivity." *Physical Review E (Statistical, Nonlinear, and Soft Matter Physics)* 73.Copyright 2007, The Institution of Engineering and Technology (2006): 66302-1. Print.

Bowden, Christiana Honsberg and Stuart. *Photovoltaics Cdrom*. 10 Nov., 2009 <http://pvcdrom.pveducation.org/>.

Catchpole, K. R., and A. Polman. "Plasmonic Solar Cells." *Optics Express* 16.Compendex (2008): 21793-800. Print.

Derkacs, D., et al. "Improved Performance of Amorphous Silicon Solar Cells Via Scattering from Surface Plasmon Polaritons in Nearby Metallic Nanoparticles." *Applied Physics Letters* 89.Copyright 2006, The Institution of Engineering and Technology (2006): 93103-1. Print.

Devers, T., et al. "Preparation of Dendritic Tin Nanoaggregates by Electrodeposition." *Journal of Non-Crystalline Solids* 321.Copyright 2003, IEE (2003): 73-80. Print.

Drozdowicz-Tomsia, K., Xie Fang, and E. M. Goldys. "Deposition of Silver Dentritic Nanostructures on Silicon for Enhanced Fluorescence." *Journal of Physical Chemistry C* 114.Copyright 2011, The Institution of Engineering and Technology (2010): 1562-9. Print.

Encyclopædia Britannica. Encyclopædia Britannica Online. Encyclopædia Britannica, 2011. ""Radiation Damping."". Jan 04 2011. <http://www.britannica.com/EBchecked/topic/488591/radiation-damping>.

Integration of a Novel Electrochemical Tuning Scheme with Mems Surface Micromachined Resonators. 2005. Institute of Electrical and Electronics Engineers Inc. Print.

Enderling, Stefan, et al. "Sheet Resistance Measurement of Non-Standard Cleanroom Materials Using Suspended Greek Cross Test Structures." *IEEE Transactions on Semiconductor Manufacturing* 19.1 (2006): 2-9. Print.

Evanoff, D. D., and G. Chumanov. "Synthesis and Optical Properties of Silver Nanoparticles and Arrays." *ChemPhysChem* 6.7 (2005): 1221-31. Print.

Farlex. "Fractal Definition". 23 Dec 2010. <http://www.thefreedictionary.com/fractal>.

Fox, Mark. "Optical Properties of Solids." *American journal of physics* 70.12 (2002): 1269. Print.

Geddes, C. D., et al. "Silver Fractal-Like Structures for Metal-Enhanced Fluorescence: Enhanced Fluorescence Intensities and Increased Probe Photostabilities." *Journal of Fluorescence* 13.Copyright 2004, IEE (2003): 267-76. Print.

Ghosh, Sujit Kumar, and Tarasankar Pal. "Interparticle Coupling Effect on the Surface Plasmon Resonance of Gold Nanoparticles: From Theory to Applications." *Chemical Reviews* 107.Compendex (2007): 4797-862. Print.

A Comparison between Rf Mems Switches and Semiconductor Switches. 2004. IEEE Computer Society. Print.

Green, M. A. "Thin-Film Solar Cells: Review of Materials, Technologies and Commercial Status." *Journal of Materials Science: Materials in Electronics*.Copyright 2008, The Institution of Engineering and Technology (2007): 15-19. Print.

Hui-Fen, Huang, Chu Qing-Xin, and Xiao Jian-Kang. "Fractal Power Network Based on Plant Vein for Power Integrity." *IEEE Transactions on Electromagnetic Compatibility* 52.Copyright 2010, The Institution of Engineering and Technology (2010): 759-62. Print.

Hutter, Eliza, and Janos H. Fendler. "Exploitation of Localized Surface Plasmon Resonance." *Advanced Materials* 16.Compendex (2004): 1685-706. Print.

Ishii, T. Koryu. *Handbook of Microwave Technology*. San Diego: Academic Press, 1995. Print.

Jhangiani, Jaideep. "Understanding Key Rf Switch Specifications." 10 Nov. 2009 <http://www.tmworld.com/file/4517-Understanding_RF_Switch_Specifications.pdf>.

Kawaguchi, Takeshi, Shigeo Maruno, and Stephen R. Elliott. "Optical, Electrical, and Structural Properties of Amorphous Ag-Ge-S and Ag-Ge-Se Films and Comparison of Photoinduced and Thermally Induced Phenomena of Both Systems." *Journal of Applied Physics* 79.12 (1996): 9096-96. Print.

Kim, Seok-Soon, et al. "Plasmon Enhanced Performance of Organic Solar Cells Using Electrodeposited Ag Nanoparticles." *Applied Physics Letters* 93.Compendex (2008). Print.

Kozicki, M. N., P. Maroufkhani, and M. Mitkova. "Flow Regulation in Microchannels Via Electrical Alteration of Surface Properties." *Superlattices and Microstructures* 34.3-6 (2003): 467-73. Print.

Kozicki, M. N., et al. "Information Storage Using Nanoscale Electrodeposition of Metal in Solid Electrolytes." *Superlattices and Microstructures* 34.3-6 (2003): 459-65. Print.

Non-Volatile Memory Based on Solid Electrolytes. 2004. Institute of Electrical and Electronics Engineers Inc. Print.

Kozicki, Michael N., Mira Park, and Maria Mitkova. "Nanoscale Memory Elements Based on Solid-State Electrolytes." *IEEE Transactions on Nanotechnology* 4.3 (2005): 331-38. Print.

New Emitter Design and Metal Contact for Screen-Printed Solar Cell Front Surfaces. 2007. Inst. of Elec. and Elec. Eng. Computer Society. Print.

Maier, S. A., and H. A. Atwater. "Plasmonics: Localization and Guiding of Electromagnetic Energy in Metal/Dielectric Structures." *Journal of Applied Physics* 98.Copyright 2005, IEE (2005): 11101-1. Print.

Maier, Stefan A., MyiLibrary, and SpringerLink. *Plasmonics*. Vol. 1. New York, NY: Springer, 2007. Print.

Miles, R. W., K. M. Hynes, and I. Forbes. "Photovoltaic Solar Cells: An Overview of State-of-the-Art Cell Development and Environmental Issues." *Progress in Crystal Growth and Characterization of Materials* 51.Copyright 2006, IEE (2005): 1-42. Print.

Mitkova, M., and M. N. Kozicki. "Mass Transport in Chalcogenide Electrolyte Films - Materials and Applications." *Journal of Non-Crystalline Solids* 352.Copyright 2006, The Institution of Engineering and Technology (2006): 567-77. Print.

Morphology of Electrochemically Grown Silver Deposits on Silver-Saturated Ge-Se Thin Films. 2003. Elsevier. Print.

Morega, A. M., and A. Bejan. "A Constructal Approach to the Optimal Design of Photovoltaic Cells." *International Journal of Green Energy* 2.Copyright 2006, The Institution of Engineering and Technology (2005): 233-42. Print.

Murray, W. Andrew, and William L. Barnes. "Plasmonic Materials." *Advanced Materials* 19.Compendex (2007): 3771-82. Print.

Naser M. Ahmed*, Zaliman Sauli, Uda Hashim, Yarub Al-Douri. "Investigation of the Absorption Coefficient, Refractive Index, Energy
Band Gap, and Film Thickness for Al0.11ga0.89n, Al0.03ga0.97n, and
Gan by Optical Transmission Method." *International Journal of Nanoelectronics and Materials* 2 (2009): 189-95. Print.

A Novel Nanoionics-Based Switch for Microwave Applications. 2008. Institute of Electrical and Electronics Engineers Inc. Print.

Orava, J. "Optical and Structural Properties of Ge-Se Bulk Glasses and Ag-Ge-Se Thin Films." *Journal of Non-Crystalline Solids* 355.37-42 (2009): 1951-54. Print.

Paunovic, Milan. *Fundamentals of Electrochemical Deposition / Milan Paunovic, Mordechay Schlesinger*. New York :: Wiley, 1998. Print.

Surface Plasmon Enhanced Silicon Solar Cells. 2007. American Institute of Physics. Print.

Pinchuk, Anatoliy, Gero Von Plessen, and Uwe Kreibig. "Influence of Interband Electronic Transitions on the Optical Absorption in Metallic Nanoparticles." *Journal of Physics D: Applied Physics* 37.Compendex (2004): 3133-39. Print.

Podolskiy, V. A., and V. M. Shalaev. "Giant Optical Responses in Microcavity-Fractal Composites." *Laser Physics* 11.Compendex (2001): 26-30. Print.

Popescu, Mihai. *Non-Crystalline Chalcogenides / by Mihai A. Popescu*. Dordrecht ; Boston :: Kluwer Academic Publishers, 2000. Print.

Qiu, T., et al. "Silver Fractal Networks for Surface-Enhanced Raman Scattering Substrates." *Applied Surface Science* 254.Compendex (2008): 5399-402. Print.

Ratnakumar, Cynthia. "Programmable Metallization Cell Fabrication and Characterization with the Focused Ion Beam." 2006. Print.

Riess, Ilan. "Comparison between Liquid State and Solid State Electrochemistry." *ChemInform* 35.4 (2004): no-no. Print.

Rinaldo, A., et al. "Thermodynamics of Fractal Networks." *Physical Review Letters* 76.Copyright 1996, IEE (1996): 3364-7. Print.

Sang-Soo, Je, et al. "In Situ Tuning of Omnidirectional Microelectromechanical-Systems Microphones to Improve Performance Fit in Hearing Aids." *Applied Physics Letters* 93.Copyright 2008, The Institution of Engineering and Technology (2008): 123501 (3 pp.). Print.

Schindler, Christina. "Resistive Switching in Electrochemical Metallization Memory Cells." 2009. Print.

Schroder, Dieter K. *Semiconductor Material and Device Characterization*. Vol. 3. Piscataway, NJ: IEEE Press, 2006. Print.

Shalaev, V. M. "Electromagnetic Properties of Small-Particle Composites." *Physics Reports* 272.Copyright 1996, FIZ Karlsruhe (1996): 61-137. Print.

Shalaev, V. M., et al. "Optical Properties of Self-Affine Thin Films." *Physical Review B: Condensed Matter* 54.Compendex (1996): 8235-35. Print.

Siah, C.H. and Aziz , N and Samad, Z and Noordin, N. and Idris , M. N. and Miskam, M.A. "Fundamentals Studies of Electro-Silver Plating Process." *Proceedings of the 18th Symposium of Malaysian Chemical Engineers* 1 (2004): 424-29. Print.

Song, Wei, et al. "Surface Enhanced Raman Scattering Based on Silver Dendrites Substrate." *Journal of Colloid and Interface Science* 298.Compendex (2006): 765-68. Print.

Steven J. Oldenburg, Ph.D. "Silver Nanoparticles: Properties and Applications." (2010). 012011 <http://www.sigmaaldrich.com/materials-science/nanomaterials/silver-nanoparticles.html>.

Stuart, H. R., and D. G. Hall. "Island Size Effects in Nanoparticle-Enhanced Photodetectors." *Applied Physics Letters* 73.Copyright 1999, IEE (1998): 3815-17. Print.

Varadan, V. K., et al. *Rf Mems and Their Applications*. Chichester, England; Hoboken, NJ: John Wiley, 2003. Print.

Wang, J. F., et al. "Tunable Surface-Plasmon-Resonance Wavelength of Silver Island Films." *Chinese Physics B* 19.11 (2010). Print.

Waser, Rainer, ed. *Nanotechnology*. Vol. 3, 2008. Print.

West, William Clark. "Electrically Erasable Non-Volatile Memory Via Electrochemical Deposition of Multifractal Aggregates." 9825781. Arizona State University, 1998. Print.

Wikipedia. "Insertion Loss". 24 Dec. 2010. <http://en.wikipedia.org/wiki/Insertion_loss>.

Wikipedia. "Solar Cell from Wikipedia, the Free Encyclopedia". 1 Nov. 2009. <http://en.wikipedia.org/wiki/Solar_cell>.

Wikipedia. "Solar Cell from Wikipedia, the Free Encyclopedia." Print.

Yang, S., J. Wu, and A. Christou. "Initial Stage of Silver Electrochemical Migration Degradation." *Microelectronics Reliability* 46.Compendex (2006): 1915-21. Print.

Zhang, X. "Interparticle Coupling Effects on Plasmon Resonances of Nanogold Particles." *Nano letters* 3.8 (2003): 1087-90. Print.

Zhu, Jian, et al. "Multifactor-Controlled Non-Monotonic Plasmon Shift of Ordered Gold Nanodisk Arrays: Shape-Dependent Interparticle Coupling." *Plasmonics* (2011): 1-7. Print.